A Study of Non-Fluid Damped Skin Friction Measurements for Transonic Flight Applications

Alexander Remington

Masters's Thesis Submitted to the Faculty of the
Virginia Polytechnic Institute and State University
in partial fulfillment of the requirements for the degree of

Master of Science
in
Aerospace Engineering

Dr. J.A. Schetz, Chairman
Dr. R. Simpson
Dr. J.R. Long

July 23, 1999
Blacksburg, VA

Keywords: Skin Friction, Aerodynamics, Eddy Current Damper

A Study of Non-Fluid Damped Skin Friction Measurements for Transonic Flight Applications

Alexander Remington

(ABSTRACT)

A device was developed to directly measure skin friction on an external test plate in transonic flight conditions. The tests would take place on the FTF-II flight test plate mounted underneath a NASA F-15 aircraft flying at altitudes ranging from 15,000 to 45,000 ft. at Mach numbers ranging from 0.70 to 0.99. These conditions lead to predicted shear levels ranging from 0.3 to 1.5 psf. The gage consisted of a floating element cantilevered beam configuration that was mounted into the surface of the test plate in a manner non-intrusive to the flow it was measuring. Strain gages mounted at the base of the beam measured the small strains that were generated from the shear forces of the flow. A non-nulling configuration was designed such that the deflection of the floating head due to the shear force from the flow was negligible. Due to the large vibration levels of up to 8 g_{rms} that the gage would experience during transonic flight, a vibration damping mechanism needed to be implemented. Viscous damping had been used in previous attempts to passively dampen the vibrations of skin friction gages in other applications, yet viscous damping proved to be an undesirable solution due to its leakage problems and maintenance issues.

Three methods of damping the gage without a fluid filled damper were tested. Each gage was built of aluminum in order to maintain constant material properties with the test plate. The first prototype used a small internal gap and damping properties of air to reduce the vibration levels. This damping method proved to be too weak. The second prototype utilized eddy current damping from permanent magnets to dampen the motion of the gage. This mechanism provided better damping then the first prototype, yet greater damping was desired. The third method utilized eddy current damping from an electromagnet to dampen the motion of the gage. The eddy current damper achieved a much larger reduction in the

vibration characteristics of the gage than the previous designs. In addition, the gage was capable of operating at various levels of damping. A maximum peak amplitude reduction of 33 % was calculated, which was less than theoretical predictions.

The damping results from the electromagnetic gage provided an adequate level of damping for wind tunnel tests, yet increased levels of damping need to be pursued to improve the skin friction measurement capabilities of these gages in environments with extremely high levels of vibration. The damping provided by the electromagnet decreased the deflections of the head during 8 g_{rms} and 2 g_{rms} random noise vibrations bench tests. This allowed for a greater survivability of the gage. In addition, the reduction of the peak amplitude provided output with vibration induced noise levels ranging from 24 % to 5.9 % of the desired output of the gage.

The gage was tested in a supersonic wind tunnel at shear levels of τ_w=3.9 to 5.3 psf. The shear levels encountered during wind tunnel verification tests were slightly larger than the shear levels encountered on the F-15 flight test plate during the flight tests, but the wind tunnel shear levels were considered adequate for verification purposes. The experimentally determined shear level results compared well with theoretical calculations.

Acknowledgments

I would like to thank my Advisor, Dr. Joseph Schetz, for providing me with the opportunity to work on this project. I would also like to thank Prof. M. Kasarda and Prof. A. L. Wicks from the Mechanical Engineering Department, and Prof. Long from the Physics department for the guidance and insightful ideas which they gave me throughout this project. I would particularly like to thank Prof. Kasarda for the invaluable knowledge about magnetism that she provided me. Also, Prof. Wicks provided his knowledge and experience of vibration theory and experimental methods which proved to be extremely helpful. I would like to thank Prof. Long for his help with my electromagnet concept and design. I would also like to thank Prof. Simpson for his assistance with this undertaking. All of these professors were very generous with their time.

Next, I would like to thank the students on the skin friction gage research team, Jurie Bereznehoit, Randy Hutcheson, Samantha Magill, Alex Sang, and Ted Smith. Everyone mentioned provided this research project with creative ideas as well as a creating an enjoyable environment to work in.

I would especially like to thank all the people at the NASA Dryden Research Facility for the funding which they provided for this project. Without their support, this degree would not have been possible.

The expertise of those in the AOE shop brought these gages into fruition. I would like to thank Bruce Stanger for the many hours he spent machining my gages to precise specifications, and I would like to thank the AOE electrician, Garry Stafford, for his aid in my electronic endeavors. In addition, I would like to thank Josh Durham for his computer expertise which kept the AOE graduate computer lab running.

I would especially like to thank my family for their support during my graduate education. This would not have been possible without the creative insight from my father, Paul, and the unconditional support of my mother, Lynne, and brother, Chris.

Table of Contents

List of Figures

List of Tables

Nomenclature

A	Area
B	Magnetic Flux Density
$C_{\#}$	Constant
C_f	Skin Friction Coefficient
C_p	Specific Heat
D	Diameter
E	Modulus of Elasticity
f	Frequency
G	Gap Size
g	Gravitational Acceleration
G_a	PSD of NASA Curve A
G_{xx}	PSD of Input
G_{yy}	PSD of Output Response
H	Transfer Function
h	Height
i	Current
L	Length
l_g	Air Gap
M	Mach Number
mmf	Magnetomotive Force
P_o	Total Pressure
P_s	Static Pressure
q	Dynamic Pressure
R	Resistance
$\mathcal{R}$	Reluctance
Re	Reynolds Number
Re_x	Reynolds Number Based on distance, x
Re_δ	Reynolds Number Based on boundary layer thickness, δ

T_s	Static Temperature
T_o	Total Temperature
t	Time
U	Velocity
V	Voltage
x	Axial Distance
y	Normal Distance from Wall
z	Vertical Distance from Floor
u_*	Friction Velocity
δ_t	Boundary Layer Thickness
ρ	Density
ρ_e	Resistivity
ϕ	Magnetic Flux
ξ	Induced emf
τ_w	Wall Shear Stress
μ	Dynamic Viscosity
μ_o	Permeability of Air
ν	Kinematic Viscosity

Chapter 1. Introduction

1.1. Motivation

In order to understand the performance of any fluid machinery system or component, knowledge of the drag created from a fluid flowing over a solid surface is required. Any object interacting with a fluid in motion experiences a drag force that can be decomposed into pressure drag, wave drag and skin friction drag. Therefore, the measurements of these drag components are vital in the optimization of performance of modern aircraft, ships, and pipe flows, etc..

For both scientific and practical reasons, the physical phenomenon of skin friction is important. The skin friction drag component is an essential parameter that needs to be quantified because it can account for more than half the drag of a streamlined vehicle.

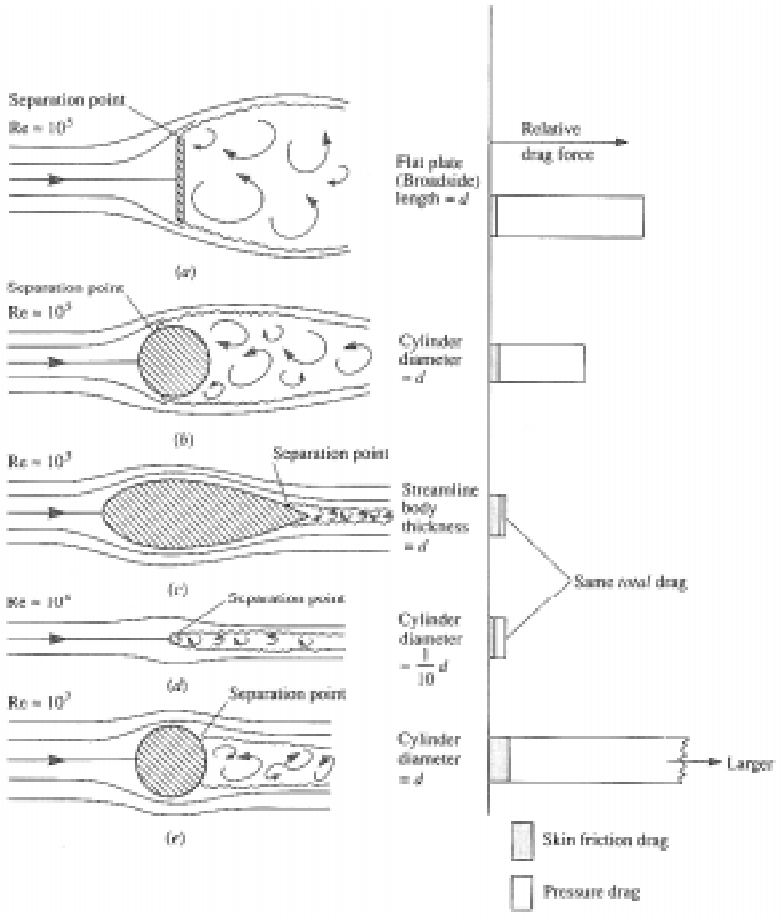

Figure 1: Relative Comparison of Skin Friction Drag on Aerodynamic Shapes [1]

From Figure 1 it is apparent that as a streamlined object similar to an aircraft travels through a fluid medium the skin friction drag dominates the drag force.

The skin friction coefficient is defined as

$$C_f = \frac{\tau_w}{\frac{1}{2}\rho U^2} \qquad [1]$$

where τ_w is the shear stress at the wall, ρ is the density of the fluid, and U is the free-stream velocity. Measuring the drag due to skin friction is a vital step that needs to be performed in virtually any system in which fluid interacts with a solid component of that system. These drag measurements are important when assessing the performance of any machinery system. For example, skin friction plays an integral role in the production of drag on the body of aircraft, consequently, these values of drag play a large role in the economics of these airplanes. The greater the thrust that an aircraft has to produce to overcome the frictional drag on a body, the greater the consumption of fuel of that aircraft. The fuel consumption of an aircraft costs a great deal of money, therefore minimizing fuel consumption is a driving force in the aerospace industry. Consequently, skin friction has large implications on the economics of virtually all machinery that interact with fluid flow. Increased knowledge about the behavior of skin friction extends beyond assessing the performance of fluid machinery and the economic ramifications therein. A greater understanding of skin friction aids in the detection of problems in intended flowfields, so that improved designs can be developed and progress in aerospace engineering can continue. The detection and location of flow separation and transition are critical aspects of fluid flow. They are critical when assessing the drag force on an object. Fluid that has transitioned to a more chaotic turbulent state generates greater drag on a body than the more ordered laminar state. The assessment of flow separation is also essential due to its disastrous effects on the performance of machines interacting with a fluid. For example, an aircraft experiences a loss in the effectiveness of its ailerons, elevators, and rudders when the flow separates in front of those control surfaces. This loss of control can lead to a potentially hazardous event. A more developed understanding of skin friction can aid in the prediction of these potentially problematic flow conditions.

Many attempts have been made to minimize this source of drag, but only a small percentage of these attempts succeed. One of the reasons for this poor success rate is that, until relatively recently, no accurate method existed to measure skin friction directly. To date, an accurate field measurement of a three dimensional skin friction distribution on a surface of aerodynamic interest has not been achieved. For this reason, accurate methods for determining the skin friction effects on a body are of great interest for physicists and engineers. Accurate methods of predicting skin friction as well as experimentally determining skin friction have eluded many researchers, but research on this important scientific property will continue until it is fully understood.

Turbulence modelers have a great need for skin friction data, particularly for off-cruise conditions where, typically, Reynolds average Navier-Stokes (RANS) predictions of drag are +/- 10% accurate at best. Skin friction is a vital component in the research of turbulence. It is involved with u_*, the friction velocity, which is a scaling velocity used in the correlation of turbulent boundary layer velocity profiles.

$$u_* = U\sqrt{\frac{C_f}{2}} \qquad [2]$$

These correlations and u_* are critical to all turbulent transport models which are used in virtually every professional CFD code. So, it is obvious that skin friction has a great impact on modern computational methods. A turbulent flow computational method is only as good as the turbulent transport model used in the program. It is this model which possesses the largest amount of uncertainty. At this point, these numerical methods do not produce accurate enough results for exclusive use in professional design. If experimental tests can provide more accurate skin friction measurements, then available computational methods and turbulence models will increase in accuracy as well, which will necessarily improve future aerospace design methods.

Over the past 40 years, advances in skin friction studies have produced a variety of direct and indirect techniques to experimentally measure skin friction. Analytical methods have been used to calculate the simple flow over a flat plate, and experimental and theoretical estimations of this flow compare well. An extensive paper by Winter [2] quotes accuracies of 1.4% to 10% for the most reliable and commonly used two-dimensional techniques. The next advancement in the experimental measurement of skin friction is the application of these

proven methods in harsher environments where analytical techniques are not reliable. The experimental measurement of skin friction in environments with extreme temperatures, “impulse tests”, high speeds, or at high vibration levels is the next logical step.

The main objective of this study is to create a method for the direct measurement of skin friction in an environment that involves a harsh level of vibration. NASA reports a high vibration level on the F-15 experimental flight test bed. Thus, a gage needs to be designed which possesses robust characteristics enabling the gage to survive in the harsh environment caused by the high level of vibration. In order to create a robust design, it is important to decrease the amplitudes of the vibrations that could cause the sensing element of the gage to violently hit the housing and potentially disassemble itself. In addition, the new design needs to be capable of producing measurements that are intelligible. For poorly damped systems, a high level of vibration causes a great deal of noise in the output data from the gage. In order to extract useful information from the output data, the noise needs to be minimized. This can be performed by a variety of techniques. At first, one expects to be able to average the data, but at extreme vibration levels near the resonance of the gage, the noise in a system may be much larger than the quantity being measured. So, a damping mechanism needs to be produced which could separate the desired output data from the noise. A variety of methods are available to provide such an effect. The seven most common methods of damping are: viscous damping, air damping utilizing small gaps, visco-elastic damping, visco-elastic isolation damping, coulomb-friction damping, damping utilizing piezoelectric materials, and eddy current damping. The potential applications of these methods are numerous because most machines experience a level of vibration during their operation. A discussion of the potential application of each of these damping mechanisms within a skin friction gage is discussed in Chapter 1.3.1. Applying a damping method that decreases the level of noise during data acquisition results in a more accurate measurement that is beneficial to every aspect of science and engineering.

1.2. Background

The science behind the concept of skin friction measurement has had a relatively short, but fascinating, history. Most likely, the first systematic investigations of skin friction were made over 100 years ago by Froude in 1872. He measured the drag of a series of planks

towed at various speeds along a tank during a time when the qualitative effects of Reynolds number on skin friction were not well understood [3]. Interest in the direct measurement of skin friction remained largely dormant until the advent of high-speed aircraft in the mid-twentieth century. The desire to continually increase the speed of aircraft revived the desire to gather precise skin friction measurements. Due to this renewed interest in skin friction, a variety of methods have been designed to measure this property. An outline of the early techniques available for the measurement of skin friction can be found in a thorough paper by Winter [2].

Current skin friction measurement techniques can be divides into two distinct categories; indirect and direct methods. Wooden and Hull [4] categorize these techniques according to the physical quantity being measured. The direct method utilizes a measurement of the wall shear force without requiring the use of any assumed laws that may require a prerequisite knowledge about the flow. This method relies on a floating element that is not intrusive into the flow. Currently, the direct method has been the preferred technique to measure skin friction, due to its smaller uncertainties, and non-intrusive nature. Indirect methods are based on the measurement of other flow quantities that are then related back to skin friction. These methods use a variety of analytical correlations to relate the measured property to a skin friction value. Indirect methods are, for example, techniques that utilize total pressure. Those techniques that measure heat transfer will be considered a subset of the indirect method because it measures a quantity other than shear force or total pressure. The Reynolds Analogy, derived by van Driest [5], is used with a heat transfer measurement to calculate a skin friction value.

1.2.1. Indirect Techniques

Figure 2 shows a variety of indirect methods discussed in another comprehensive comparison of techniques for measuring friction drag by Nitsche [6]. The ones that will be discussed are surface hot film, wall-fixed hot wire, wall fixed double wire, sublayer fence, Preston tube, and computational Preston tube. In addition, the Stanton tube, optically active liquid crystals, and the fringe imaging skin friction technique, which are not noted in Figure 2, will be considered here.

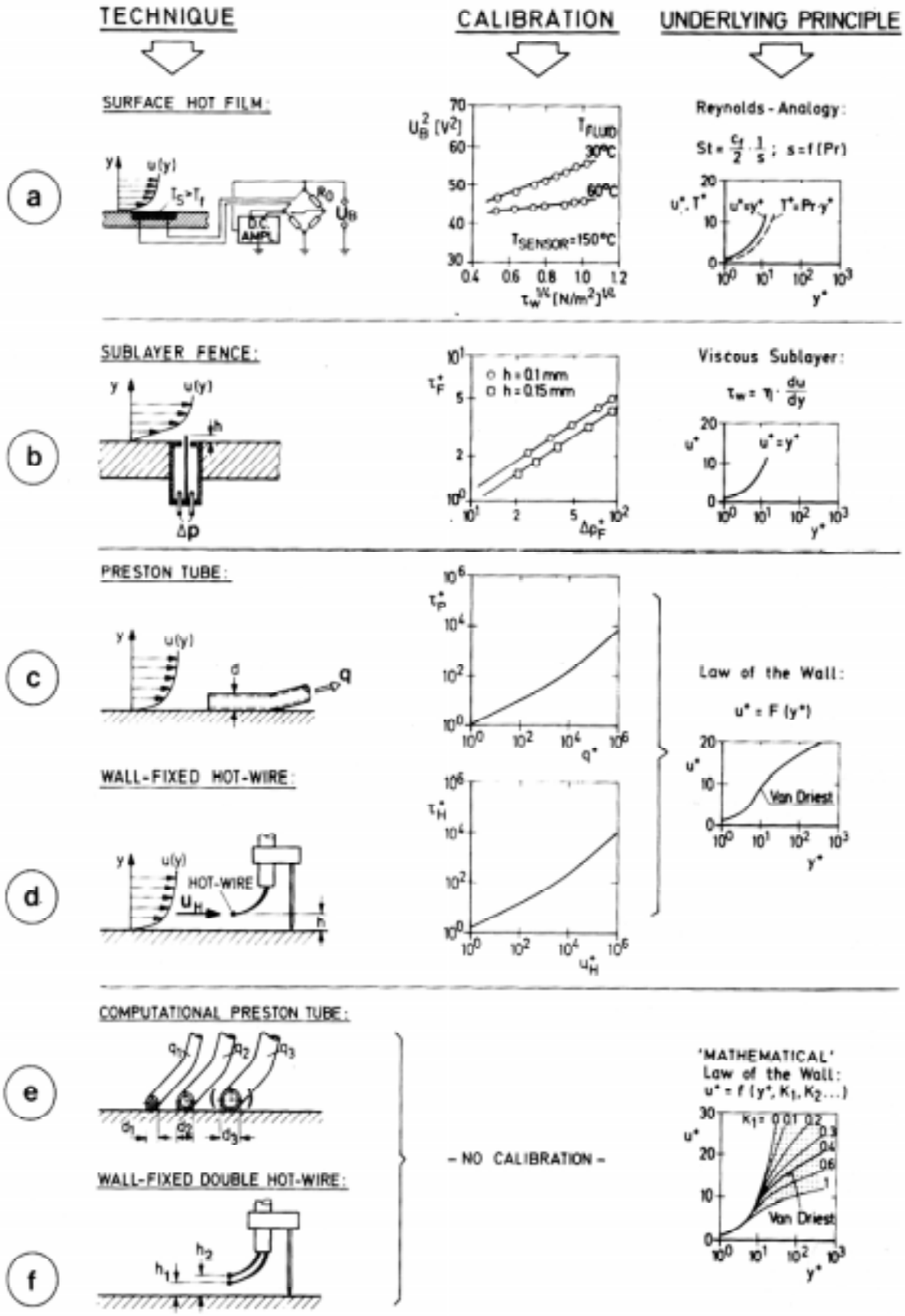

Figure 2: Indirect Methods for Measuring Skin Friction[6]

The Preston tube is one of the most popular indirect methods of skin friction measurement available to the aerodynamicist. The Preston tube operates by utilizing a small Pitot tube resting on the wall surface in order to measure the dynamic pressure of the flow. This method makes use of the similarity law of the boundary layer. The wall shear can be related to the measured dynamic pressure from the probe with an empirical calibration curve that is a fit through a logarithmic law. The reason that this method is so common stems from the size of the Preston tube. The larger sized tube allows the probe to sense not only the viscous sublayer, but the sublayer's buffer layer and the logarithmic portion of the boundary layer. This necessitates that the complete law of the wall must be used when utilizing this technique. This technique does possess some inherent errors for cases that deviate from the norm and, consequently, deviate from the law of the wall. The direct relationship between the law of the wall and the calibration curve indicates that unrestricted use of the classical calibration curve in boundary layer flows can lead to significant measuring errors in situations that cause a deviation from the law of the wall. The law of the wall tends to break down in the transition region and in areas of separating and reattaching flows, and this law can only be used in limited cases of three-dimensional flow. Several researchers have published papers using the Preston tube method [7], [8]. The computational Preston tube method was created because of the failures that the classical Preston tube method possessed in the boundary layer flows with unknown law of the wall conditions. This computer-aided method requires no calibration curve. Instead, an iterative numerical method is used which eventually converges to a velocity distribution which, consequently, will yield the corresponding wall shear stresses. This method has been outlined and documented in papers by Nitsche, Thuenker and Haberland [9],[10]. Both methods are typically used in steady, unheated flow, yet this is an intrusive method that will disturb the flow field.

Another method that utilizes pressure measurements is the sublayer fence. This technique is based on the similarity law of the viscous sublayer. In this method, the measured differential pressure on the fence is correlated to the local wall shear stress assuming a relationship between this pressure and the velocity distribution close to the wall. The correlation is generally an empirically determined calibration curve. Sublayer fences with small fence heights are relatively insensitive to additional flow parameters. From this, it can be recommended as a reference-measuring device in experimental shear stress investigations. This method is typically applied in steady, two-dimensional, unheated flow. This is also an intrusive method that will disturb the flow field.

The governing principles of the wall-fixed hot-wire method are similar to that of the Preston tube. The fundamental principle involved is the law of the wall. The measured velocity of a hot wire can be correlated more directly to the local wall friction because of a more accurate relationship between flow velocity, wall distance and shear stress. The restrictions of this technique in flows with additional parameters of influence are identical to those of the Preston tube. However, this method can be regarded to be less sensitive to variations in the law of the wall. As with the Preston tube, this method is typically used in steady, two-dimensional, unheated flow and this is an intrusive method that will disturb the flow field.

The wall fixed double hot wire method is similar to the computational Preston tube method. This method has the advantage of having two velocities above the wall measured in a direct manner instead of indirectly utilizing the dynamic pressure. The iterative computer aided evaluation procedure of the wall shear corresponds closely to that of the computational Preston tube method. This technique does require intricate preliminary tests that locate the hot wires with respect to the wall. As with the single wall-fixed hot-wire, this method is typically used in steady, two-dimensional, unheated flow, and this is an intrusive method that will disturb the flow. These devices are also fragile.

The surface hot-film technique is based on the fundamental analogy between local skin friction and heat transfer. The technique involves a small electrically heated metallic sensor embedded in a wall and maintained at constant temperature. The convective losses of the sensor are correlated to the wall shear stress by means of an individual calibration. These convective losses are generally assumed to be proportional to the electric power input to that sensor. When a constant temperature anemometer bridge circuit is used the empirical calibration formula is commonly of the form

$$V_B^{\,2} = A + B\tau_w^{\,n} \qquad [3]$$

with V_B representing the bridge voltage, the constants A and B depend on the flow, sensor temperature, properties of the wall, and/or probe support material. The factor n commonly ranges from 0.25 to 0.3. The hot film technique has been successful in cases where

Reynolds' Analogy may be applied. This is also a technique that is used in situations where the direction of the flow is not a concern. Several researchers have published papers utilizing this technique [11], [12],[13].

The Stanton tube is a method similar in principle to the Preston tube. It involves a Pitot tube with a rectangular opening which can easily be fabricated by placing a piece of a razor blade over a static pressure hole. This modified tube opening allows the Stanton tube to get readings closer to the wall surface. The fundamental basis of the Stanton tube is the same as the Preston tube. The pressure measurements in the near wall region are measured and the wall shear is calculated through the empirical relations using the law of the wall to fix a velocity profile. The Stanton tube suffers from the same complications as the Preston tube as well. When the Stanton tube encounters conditions that deviate from the law of the wall, then large errors can occur. The two techniques appear nearly identical, yet there are some important differences. The Stanton tube does not respond well to pressures resulting from the deceleration of fluid in front of the tube. Therefore, it can respond more quickly to local shear stress fluctuations. In addition, the calculation of the wall shear levels are significantly more tedious than Preston tube calculations due to the numerous physical parameters which influence the calibration of the Stanton tube (i.e. tube dimensions, tube placement). As with the Preston tube, this is an intrusive method that is typically used in steady, two-dimensional, unheated flow.

A relatively unique semi-direct technique used to measure skin friction involves the use of optically active liquid crystals. These crystals are capable of reflecting the light of a particular wavelength, which will changes in response to given physical stimuli. For skin friction applications these crystals are manufactured so that they are sensitive to shear stress. Thus, a relationship between shear stress and reflected wavelength can be generated. The crystals are capable of indicating areas where large differences in shear occur, but they are a poor indication of smaller deviations in shear. For example, the difference between 1000 Pa and 900 Pa would not be a good use of this method [14]. The optically active crystal method is more of a qualitative approach than a quantitative one. Because of this characteristic in the technique, the method is generally used in attempts to locate transition instead of quantifying actual skin friction values. This technique is generally used in unheated, steady, "field" measurements. Gaudet and Gell studied this method in 1989 [15].

The final method discussed is generally categorized as a semi-direct method. The fringe imaging skin friction technique (FISF) was inspired by the works of Tanner and Blows [16], and then further developed by Monson and Mateer [17], who eventually measured the skin friction on a two-dimensional transonic airfoil and found that their values compared reasonably well with a Navier-Stokes solution. The system was then advanced by Zilliac in 1992 [18]. The FISF technique is generally used in steady, unheated applications.

> "The essence of the technique is that a simple expression relates skin friction to the thickness variation of an oil patch experiencing shear at a point on a surface. The oil-patch thickness variation is measured using interferometry. This technique is fundamentally similar to the laser-interferometer skin friction technique [19], [20], [21], [22] except that the spatial variation of the oil-patch thickness is measured as opposed to the temporal variation. The accuracy and limitation of the two techniques are similar (+/- 5%) but, inherently, the FISF technique is simpler and much less time consuming to use. To date, the technique has been used successfully in several different two-dimensional flows to measure skin friction and also for transition detection, yet questions remain as to the effect of pressure gradients, high shear gradients, flow steadiness, and surface quality in addition to issues concerning implementation in a three-dimensional flow and determination of the fringe spacing from the interferogram images."[18]

1.2.2. Direct Techniques; Nulling and Non-Nulling

Winter [2] detailed the history of early measurement of skin friction with direct methods in a paper in 1977. All direct methods measure skin friction in the same manner. A gage is used which measures the wall shear force, without requiring the use of any assumed laws that may require a prerequisite knowledge about the flow. This method relies on a floating element that is not intrusive into the flow. Due to its small uncertainties, the direct method has been the preferred technique to measure skin friction. An extensive compilation of the history of the direct measurement of skin friction was produced by in 1999 by Magill [23]. This history of skin friction can be found in Table 1 below. It outlines all of the researchers, their area and era of research, as well as their significant breakthroughs.

Table 1: Chronological Development of Direct Skin Friction Measurement Techniques from Magill [23]

Reference	Year	Test Conditions	Nulling or Non-Nulling	Size of Floating Element (mm)	Type of Suspension/Position /Force Transducer	Gap Filler	2D/3D Flow	Remarks
Kempf	1929	Bottom of a pontoon, 77m long , $Re \leq 5 \times 10^8$	Nulling	309 x 1010	Pulleys and springs	None	2D	Measurements made in water. Schematic, Figure 2 (Winter, 1977)
Schoenherr	1932	"Catamaran Friction Planes", 0.3 to 3.0 ft/s $Re \approx 2 \times 10^6$	Nulling	914.4 x 457.2 to 1828.8 x 914.4	Weights pulled by gravity	None	2D	Towing tank in water and glycerine Schematic Figure 3 (Schoenherr, 1932)
Schultz-Grunow	1940	U=20m/s $1.6 \times 10^6 < Re_x < 16 \times 10^6$	Nulling	300 x 500*	Optical/manually-operated offset torsion bar	None	2D	Very large
Weiler & Hartwig	1952	Supersonic wind tunnel	Nulling	25 dia	Flexures LVDT**	None	2D	Schematic, Figure 3 of Winter (1977) DRL, University of Texas
Chapman, and Kester	1953	Subsonic and supersonic turbulent flow Axial flow over cylinders $4 \times 10^6 \leq Re_x \leq 32 \times 10^6$	Nulling	Cylinder, L/D=8,13, and 23	Transducer	None	2D	Ames Lab NACA (Chapman and Kester, 1953)
Coles	1953	$M = 1.97, 0.4 \times 10^6 < Re_x < 10 \times 10^6$ $M = 2.57, 0.4 \times 10^6 < Re_x < 9 \times 10^6$ $M = 3.70, 0.5 \times 10^6 < Re_x < 8 \times 10^6$ $M = 4.54, 0.4 \times 10^6 < Re_x < 8 \times 10^6$	Nulling	6.2 x 37.9	Flexure Assemble (Parallel linkage) Schaevitz variab le reluctance transformer (LVDT) Dashpot damping	oil	2D	Schematic, Figures 15-17 of Coles(1952) Jet Propulsion Laboratory
Dhawan	1953	Low speed $6 \times 10^6 < Re_x < 60 \times 10^6$ Subsonic $0.2 < M < 0.8$, $0.3 \times 10^6 < Re_x < 1.2 \times 10^6$ Supersonic $1.24 < M < 1.44$	Nulling	11.5 x 63 2 x 20	Parallel interchangeable LVDT	None	2D	GALCIT "Correlation" Tunnel Schematic, Figure 6 of Dhawan (1952)
Eimer	1953	Hypersonic, M=5.8, Laminar Flat Plate with condesation	Nulling	50.8 X 25.4	Schaevitz transformer (LVDT) Chemical Balance and Flexures	None	2D	GALCIT-Hypersonic 5X5in tunnel Schematic, Figures 17 & 18 of Eimer (1953)
Hakkinen	1953	Transonic					2D	GALCIT
Blumer, (Bradfield, & DeCoursin)	1954	$M=2.6, 1 \times 10^6 < Re_x < 8 \times 10^6$ Axially symmetric conical, turbulent boundary layer	Nulling	254 long, 15^ocone	Schaevitz transformer (LVDT)	None	2D	University of Minnesota, Rosemount Aeronautical Laboratory Schematic Figure 4 (Blumer, 1954)
Wolff	1956	Subsonic, 64 ft/s to 286 ft/s Laminar flow over various Flat Plates	Nulling	1006.475 x 749.3	Baldwin cantilever spring strain gages	None	2D	University of Minnesota Schematic Figure 2 (Wolff, 1956) Flat Plates of glass, painted glass, & aluminum (Alclad)

Reference	Year	Test Conditions	Nulling or Non-Nulling	Size of Floating Element (mm)	Type of Suspension/Position /Force Transducer	Gap Filler	2D/3D Flow	Remarks
Lyons & Fenter	1957	Supersonic Flight	Nulling	50 dia	Double parallel inter-connected linkage to eliminate sensitivity to linear and rotational accelerations	None	2D	Tested on rockets
Everett	1958	Incompressible liquid flow with variable channel height To study pressure gradient effects	Nulling	25.4 dia 25.146 dia	Beryllium-copper flexure Schaevitz transformer (LVDT)	Silicon e fluid	2D	Variable gap size and thickness Schematic, Figure 4 of Everett (1958)
Smith & Walker	1958	$0.11 < M < 0.32$ $10^6 < Re_x < 40 < 10^6$	Nulling	50 dia	Parallel linkage LVDT Kelvin current balance	None	2D	
MacArthur	1963	Shock Tunnel/Impulse Facilities	Nulling	6.4 dia	Parallel linkage Lead zirconium titanate piezoeletric ceramic beams	None	2D	Overcame difficulty in measuring small forces. It was complex with limited success, also, know as Calspan gage
Moulic	1963	M = 6 Low Density	Nulling	0.25 x 25	Side flexure pivot LVDT	None	2D	Studied strong interaction region near leading edge of flat plate
O'Donnell	1964	M=2.67, Re_θ=10070	Nulling	25 dia	Parallel Linkage	None	2D	Studied effects of misalignment of floating head
Young & Westkaemper	1965	Supersonic flow with heat transfer and surface roughness	Nulling	25 dia	Parallel linkage	None	2D	
Dershin *et al.*	1966	Supersonic flow with mass transfer	Nulling	"Pointed ellipse"	Parallel linkage LVDT	None	2D	
Moore & McVey	1966	High temperature hypersonic flows	Nulling	NA	Flexure pivot Pneumatic position sensor High temperature motor	None	2D	
Brown & Joubert	1969	Low-speed adverse pressure gradients	Nulling	19 dia	Parallel linkage LVDT	None	2D	Studied pressure gradient forces with in gap
Fowke	1969	Supersonic speeds	Nulling	127 dia	Flexure pivot LVDT Permanent magnet plus coil	None	2D	
Bruno, Yanta & Risher	1969	Supersonic speeds including flows with heat transfer	Nulling	20.3 dia	Flexure pivot LVDT Motor-driven spring	None	2D	Force variable by changing loading spring Naval Ordinance Lab
Winter & Gaudet	1970	$0.2 < M < 2.8$ $16 \times 10^6 < Re_x < 200 \times 10^6$	Nulling	368 dia	Parallel linkage Resistance strain gauges	None	2D	Surface roughness tests

References	Year	Test Conditions & Location	Nulling or Non-Nulling	Size of Floating Element (mm)	Type of Suspension/Position /Force Transducer	Gap Filler	2D/3D Flow	Remarks
Hastings & Sawyer	1970	M = 4 $10 \times 10^6 < Re_x < 30 \times 10^6$	Nulling	7.9 dia	Parallel linkage LVDT	None	2D	
Paros (Kistler)	1970	Used in a wide range of conditions including flight. Cooling system available	Nulling	9 dia	Pivoted about crossed-spring flexure. Differential capacity	None	2D	Schematic, Figure 4 of Winter (1977)
Miller	1971	Low-speed flow. Favourable pressure gradient	Nulling	25 dia	Parallel linkage LVDT			Extension of Brown & Joubert in 1961 2D
Franklin	1973	Subsonic wind tunnel and water channel	Nulling	16 dia	Pivoted. Variable geometry electronic valve.	None	2D	
Morsy	1974	Low speed flow past circular cylinder	Nulling	50.1 x 3.2	Jewelled pivots. Clock springs LVDT	None	2D	
Van Kuren	1974	High-temperature hypersonic flows with heat transfer. Floating element water cooled	Nulling	12 x 12	Parallel linkage LVDT	None	2D	
Ozarapoglu & Vinh	1975	Low-speed. Adverse pressure gradients	Nulling	127 dia	Air bearings LVDT	None	2D	Studied effects of changing gap geometry. Errors in skin friction increased with gap size.
Waltrup & Schetz	1973	Complex supersonic flow with a strong adverse pressure gradient and with injection through porous and tangential slots M=2.4	Nulling	25.4 dia	LVDT	Silicone oil	2D	Supersonic Wind Tunnel
Kenworthy & Schetz	1973							
Van Overeem & Schetz	1975							
Nerney & Schetz	1977	Low speed, and turbulent flow on smooth, rough, curved, and porous surfaces with and without injection	Non-Nulling	25.4 dia	Semi-conductor Strain Gages	Silicone oil	2D	Virginia Tech Supersonic Tunnel
Kong & Schetz	1981-2							
Collier & Schetz	1984							
Deturris, Hellbaum, & Schetz	1990	Hot high-speed flow. M=3, T=1667K &	Nulling	12.7 dia	Semi-conductor Strain Gages (DSC sensor)	Silicone oil	3D	Cooling of strain gages with water Schematic, Figure 3 of Schetz (1997) Virginia Tech Supersonic Tunnel
Kelly, Simmons, & Paull	1992	Impulse tests, hypersonic flow	Non-Nulling	10 dia	Piezoelectric transducers	Thermal cover	2D	Prototype, no successful tests, yet University of Queensland, Australia Schematic, Figure 8 of Novean (March, 1996)

References	Year	Test Conditions & Location	Nulling or Non-Nulling	Size of Floating Element (mm)	Type of Suspension/Position /Force Transducer	Gap Filler	2D/3D Flow	Remarks
Chadwick , Deturris, & Schetz	1993	Very high heat flux M=10-12, T_t=4500K q=2000KW/m^2 &	Non-Nulling	6.35 dia	Crystal Strain Gages	Silicone oil	3D	Schematic, Figure 6 of DeTurris(1992) NASA Ames DCAF
Bowersox, Chadwick, Diewert, & Schetz	1995	Impulse tests M=14 & 1. NASA Ames 16 “ Shock Tunnel, t=2.0ms 2. Hypulse Facility, t=0.3ms	Non-Nulling	8.13 dia	Semi-conductor Strain Gages	Silicone oil		Low thermal conductivity plastic Schematic, Figure 8 of Schetz (1997)
Paik & Schetz	1995	Supersonic flow unheated M=2.4	Non-Nulling		Semi-conductor Strain Gages	Silicone oil		Combines skin friction and heat flux measurements Virginia Tech Supersonic Tunnel
Novean, Bowersox, & Schetz	1996	Shock Tunnel, M=12-14, τ=200-3000Pa HYPULSE, M=14HP(high pressure) , τ=800-3000Pa Supersonic Tunnel, M=2..D4	Non-Nulling	4.55, 4.6, 5.4 dia	Semi-conductor Strain Gages	Silicone oil & Rubber RTV615	2D	Good, except when shocks impinge on floating head Schematics Figures 92-96 of Novean (March, 1996) NASA Ames 16 Inch Shock Tunnel GASL, HYPULSE Facility Virginia Tech Supersonic Tunnel
Remington & Schetz	1999	esigned for Transonic, M=0.7 to 0.99, τ=0.3 to 1.45 psf Tested in Supersonic Tunnel, M=2.4	Non-Nulling	4.2, 6.35, 9.53 dia	Kistler-Morse Strain gages Eddy current damping	None	2D	Schematic in Figure 57 of Remington (1999)
Pulliam & Schetz	1999	Designed for supersonic and high temperature environments	Non-Nulling	1.6256 dia	Fiber optics	Silicone oil	2D	Under construction

*Estimated from Sketch

** Linear Variable Differential Transformer (LVDT)

The direct method is generally divided into two categories; nulling and non-nulling designs. The nulling design involves a sensing element, generally a small movable portion of the wall, which is acted upon by the shearing force, yet does not have a net deflection. The sensing element is returned to its original position by a restoring force that is equal to the shear force interacting with it. The parallel linkage mechanism required to perform this task is complex in arrangement and cumbersome in size. Because the sensing element does not move in this method, the flow will not be disturbed during the measurement period. This method was first developed in the seminal works of Dhawan [24] in 1953 for application with measurements in the low-speed range for laminar and turbulent boundary layers. The device Dhawan developed is shown in Figure 3. The flat plate used for the measurements is supported from the ceiling of the tunnel. A variety of nulling designs have been developed for the measurement of skin friction, but they all come with some drawbacks. First, the nulling design has a much slower time response. Second, due to the mechanical complexities of the parallel linkage mechanism, problems with fabrication, assembly, size, and survivability become issues. Third, the designs from Dhawan were primarily tested in the low speed regime. There have only been a few successful applications in the high-speed regime. The nulling technique is generally used in two-dimensional, unheated flows.

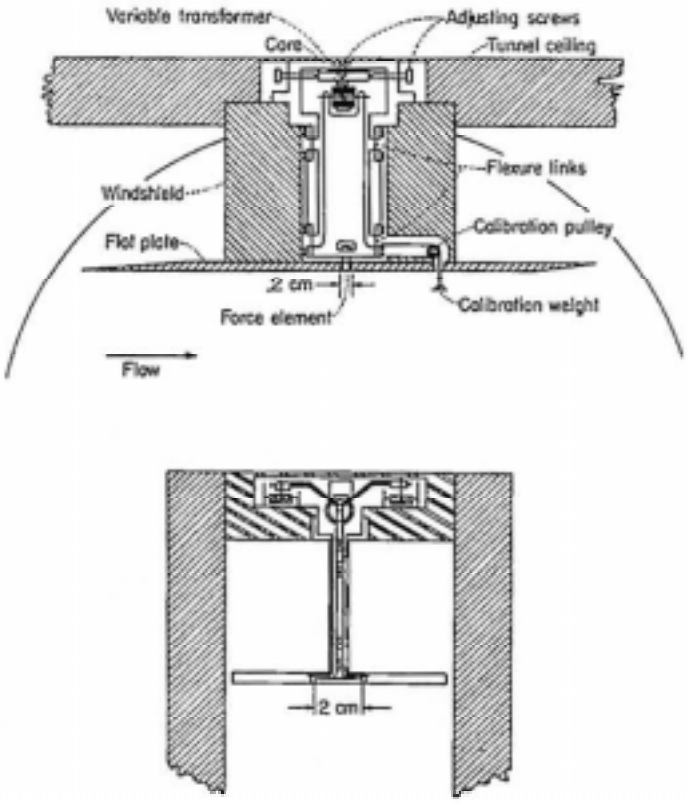

Figure 3: First Successful Gage Built by Dhawan [24]

The non-nulling design is a much simpler concept. The sensing element is allowed to deflect under the shearing load, yet the deflections are minimized to the extent that the floating element does not protrude into the flow and produce erroneous results. This leads to the important issue of misalignment, which will be discussed in Chapter 3.3, Analysis of Errors. Minimization of misalignment can be accomplished by using a stiff beam that resists large deflections. Generally, the sensing element consists of a floating head mounted on a cantilevered beam. The strain is measured at the base of the cantilevered beam, and it is related to the shear force at the sensing head. Strain gages are mounted at the base of the beam. A description of the strain gages can be found in Chapter 3.2, Strain Sensor System. This non-nulling configuration allows for an uncomplicated design for fabrication and maintenance and a more manageable size for engineering applications. The general concept for a direct method non-nulling gage can be seen in Figure 4.

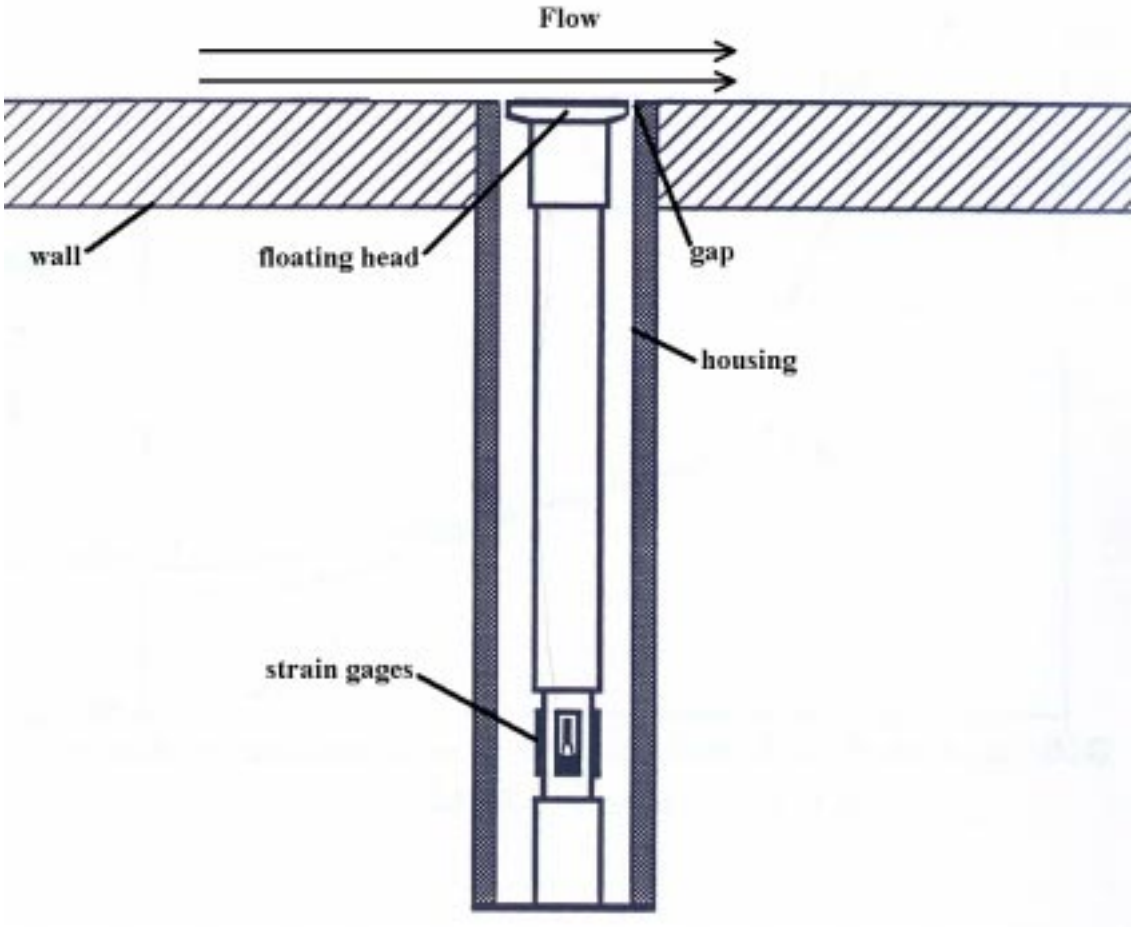

Figure 4: Simple Direct Method Non-Nulling Gage Concept [25]

The direct non-nulling method is also less susceptible to error, and has a faster time response than nulling designs. It can measure two components of the wall shear in three-dimensional flow. A variety of skin friction gages have been developed over the past decade using this non-nulling design. A review of the non-nulling techniques developed at Virginia Tech can be found in Schetz [25]. In the last decade, a great deal of effort has been placed in understanding the flow field inside propulsive systems. The environment in which an engine operates is analytically unclear and extremely hostile. Chadwick [26] and DeTurris [27] have conducted research using this non-nulling cantilevered configuration in heated supersonic applications within scramjet combustors. Beyond supersonic engine applications, considerable effort has been placed in creating a gage that can measure the skin friction within hypersonic applications. Novean [14], researchers at Calspan [28], [29], [30] and researchers at the University of Queensland in Australia [31] have developed skin friction gage designs for impulsive facilities. Currently, a great deal of research is being conducted at Virginia Polytechnic Institute and State University with skin friction gages in a variety of hostile environments.

Previous skin friction gages developed at Virginia Tech have employed oil in the internal volume for four main purposes. First, the liquid inside the gage housing provided a continuous surface to the external flow making the gage minimally intrusive. Second, the liquid fill minimized the effects of pressure gradients. Third, it helped in thermal stabilization and protection of the gage. Fourth, the liquid fill reduced the effects of facility vibrations by providing strong viscous damping. The only disadvantage to the oil fill was that it slowly leaked out over time even with the small gaps (0.004 in. nominal) around the floating head. This meant that the gage required frequent inspection and servicing. In some applications, that was a serious disadvantage. In addition, the oil leakage left a residue on the gage head that made the simple task of gage calibration difficult. Thus, there were incentives for gage designs with no fill at all.

Some work was done with a rubber fill replacing the oil, but that had some disadvantages. This concept which involved a direct non-nulling gage that utilized a rubber filled gap was successfully developed by Novean [14]. The calibration of the gage proved to be the greatest obstacle. Currently, a calibration rig is being developed which will eliminate this calibration problem. In addition, there were sensitivity issues, as well as a much larger gap required around the floating head. This gage concept had the advantage of good

vibration characteristics, as well eliminating the oil leakage problem previously discussed. It also provided a continuous surface for the external flow, as well as a robust design.

1.3. Objectives and Approach

Of increased interest are environments with extreme vibrations involved. Research in this realm of skin friction has been scarce, but many applications such as flight-testing are available for skin friction gages that can survive and operate efficiently in environments of extreme vibration.

1.3.1. Objectives

The primary objective of this skin friction gage research was to revise the current method of damping used in skin friction gages developed at Virginia Tech. There was a need to produce a gage with better vibration characteristics without sacrificing the accuracy and operation of the measurement capabilities of the gage. In addition, the gage needed to mitigate the operational problems encountered with previous oil-filled gages.

A variety of concepts were explored which could produce a large damping effect without oil fill. The available damping systems that were evaluated are as follows:

1) Viscous damping with exotic material fill
2) Air damping utilizing small gaps
3) Visco-elastic damping
4) Visco-elastic isolation damping
5) Coulomb-friction dampers
6) Damping utilizing piezoelectric materials
7) Eddy current damping

The most common method of damping available was the first method mentioned, viscous damping. With this method, a viscous fluid surrounded the vibrating object and the result was a damping force which was directly proportional to velocity. Viscous dampers

have been used on skin friction gages before, yet a variety of problems were encountered. The viscous fluid tended to leak out of the head region of the gage. This resulted in a skin friction gage design in which the viscous damping system of the gage could be degraded over the course of an experiment. Consequently, an improved damping system was desired for the skin friction gage. A variety of different exotic fluids were explored including gels, foams, commercial magnetorheological (MR) fluids [32] and electrorheological fluids. MR fluids are fluids that respond to an applied magnetic field. These fascinating materials proved to be too difficult to implement, so the concept was discarded. Foam and gel fills were explored as well, yet they performed poorly at high and low temperatures. The properties of the gels and foams would change rapidly over a temperature range. Even the viscous nature of many gels would change drastically for small temperature changes. Thus, the gel and foam fill concepts were discarded.

The next damping system utilized small air gaps around the vibrating system. Gaps on the order of 0.002 in. between the beam and housing provided a means of damping the gage. This system harnessed the viscous forces in these minute gaps to create a damping mechanism on the vibrating system. This damping mechanism eliminated the oil fill leakage concerns, yet its ability to reduce significant vibration effects was suspect. These small gaps would make it more difficult for air to flow around the internal volume of the gage and out through the gap between the floating head and the outer housing. The greatest advantage of this method is its simplistic nature.

Wrapping an elastic material around a vibrating beam can produce visco-elastic damping or hysteresis damping. Virtually all materials exhibit some level of damping when strained repeatedly. Visco-elastic materials such as silicon rubbers and gels provide a significant amount of damping. Rubbers are known to be temperature sensitive. So, visco-elastic damping at frigid temperatures can result in a poor damping due to brittle nature of the substance at low temperatures. Rubber filled gages have been designed in the past at Virginia Tech, yet the concept produced some calibration issues that are currently being researched. The Kistler-Morse DSC strain gage units used in these skin friction gages are manufactured with a small ring of silicone rubber around the base to protect the strain gages. Thus, there is some inherent damping provided by the strain gage units, but the amount of silicone rubber is inadequate for that purpose, and greater damping is required for these applications.

The most effective way to reduce unwanted vibration would be to stop or modify the source of the vibration. If this could be done, than it would be possible to design a vibration isolation system to isolate the device from the source of the system. This damping system could be produced by using a highly damped material such as a rubber to change the stiffness and damping between the source of vibration and the device that needs to be protected from the vibrations [33]. A visco-elastic isolation system would be similar to the visco-elastic damping mechanism mentioned previously. The difference would be that the entire gage housing would be surrounded with a rubber material in an attempt to isolate the gage from the intense random vibrations induced by the flight characteristics of the F-15. Again, the brittle nature of rubbers at low temperatures would result in poor damping characteristics.

The fifth type of damping considered was a coulomb-friction damper. These are often used in machinery isolators. In this method, small metal bearings would fill the inside of the gage shaft. The frictional forces of the bearings sliding against one another during the movement of the beam cause the vibration of the shaft to dampen. In a friction damper, the force is directly proportional to the coefficient of friction for the contacting surfaces, the area, and the pressure applied to bring the plates into contact. Generally, the predicted amount of damping available for a given situation would be unreliable due to the inaccurate friction coefficient estimates. In addition, this method was considered an unreasonable damping solution, because a coulomb-friction damping system would not be able to be implemented into a skin friction gage with such small dimensions.

Piezoelectric damping systems are most often used in actively controlled damping systems. Piezo ceramic patches connected to electronic shunt circuits have formed successful vibration reduction devices. A drawback of existing electronic shunt circuits is the large inductance required when suppressing low frequency vibrations [34]. New shunt designs can significantly reduce the structural vibration response with half of the inductance previously required, yet these damping systems are often expensive, complicated, and require another power source. Like Coulomb damping, piezoelectric damping would be difficult to implement due to the small dimensions of the skin friction gage head. An additional issue stems from the location of the strain gages. This is the location of attachment for most piezo-electric vibration control devices. Also, this technique is extremely sensitive to temperature.

The use of an eddy current damper as a damping device has been used in a variety of applications where other methods have proved to be inadequate [35]. It was found to be very successful in the magnetic bearing industry and also in applications where a tunable and active vibration damping system was desired [36]. Eddy current dampers have been created using electromagnets and permanent magnets. There are several advantages of using permanent magnets in a passive damping system. A permanent magnet eddy current system is an inherently passive damping system. Thus, no additional power sources are needed which simplifies the system. The damping force is velocity/frequency dependent, but more importantly, the damping coefficient varies inversely with the resistivity of a conductor moving in the magnetic field. The electromagnet eddy current damper system possesses a variety of characteristics that are attractive to skin friction designs. The electromagnet is capable of producing a larger magnetic flux density and, consequently, a larger damping ratio. It tends to be a more complicated system that requires power sources and larger spaces, yet it has the ability of being controllable.

1.3.2. NASA Flight Test Vibration Requirements

The anticipated vibration environment for the design of this skin friction gage is quite violent. Thus, all instrumentation that is to be mounted on the flight test bed requires a verification of its operability within that environment. The vibration analysis of the skin friction gage involves the simulation of a Random Vibration Test Curve provided by NASA in their vibration specification manual [37]. All devices that are mounted within the FTF-II plate need to pass test specifications for use during flight experiments. The skin friction gage will be subject to Category II test requirements (turbojet powered aircraft tests). For acceptance on to the FTF-II , the skin friction gage must be tested under representative FTF-II conditions. Vibration tests on all hardware would be performed using a random vibration test curve equivalent to 8.0 g_{rms} at a frequency range from 15 to a maximum of 2000 Hz. NASA specifies these conditions for operation in the flight test fixture with Curve A shown in Figure 5. The approximate flight conditions for the F-15 are listed below in Table 2.

Table 2: F-15 Flight Test Conditions

Mach	0.7-0.99
Altitude	45,000 ft
Temperature at 45,000 ft	-70 F
Wall Temperature Range	0-120 F
C_f	~0.002
Re_{flight}	~5 million/foot

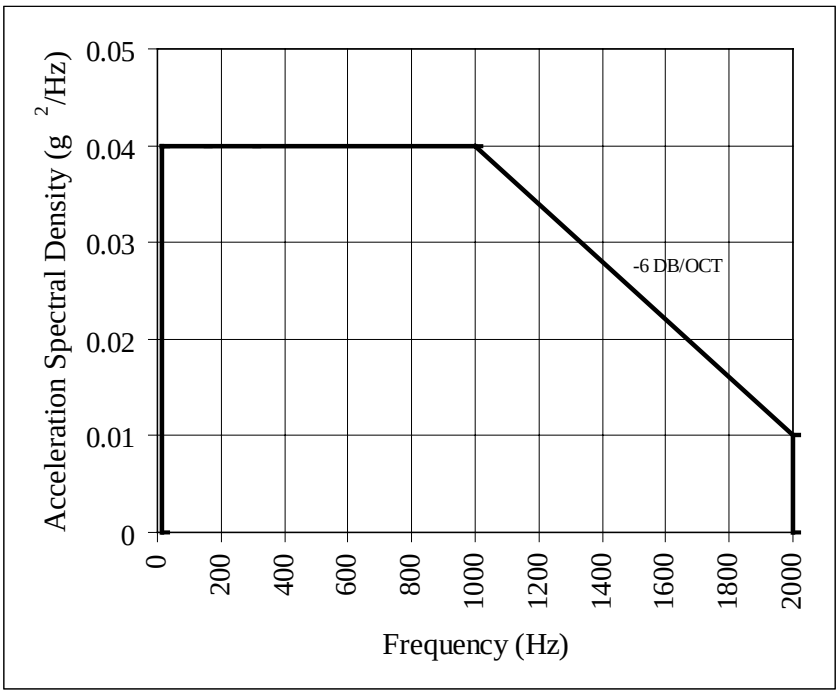

Figure 5: NASA's Vibration Test Requirement Curve A

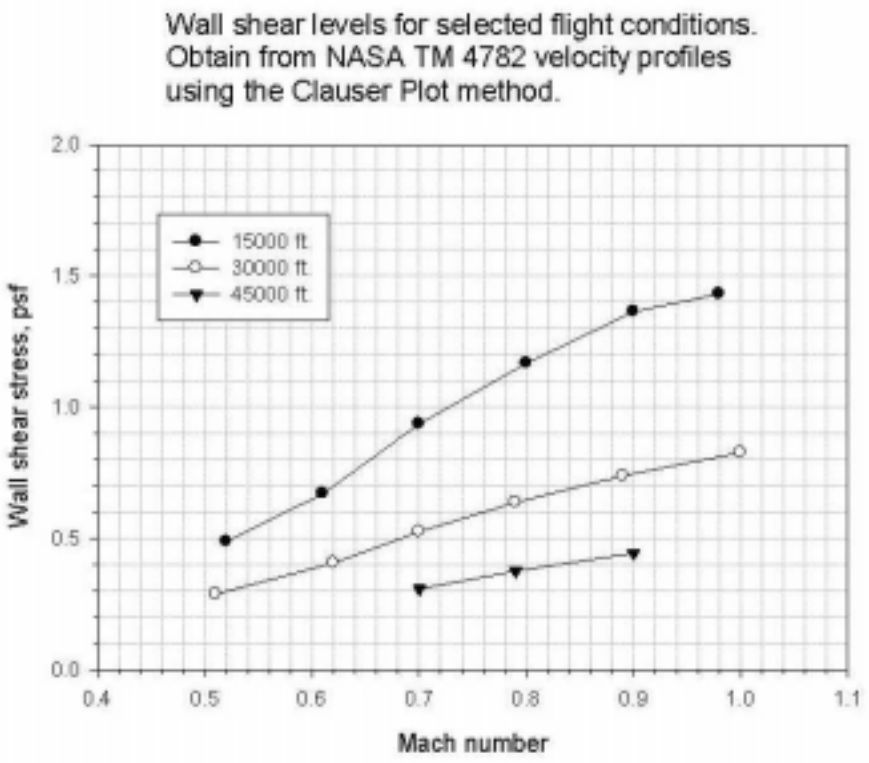

Figure 6: Anticipated Shear Levels at Various Flight Profiles

According to NASA, the flight profile that the F-15 runs during its test leads to anticipated shear levels in the range from 0.3 to 1.45 psf. on the FTF-II plate. The anticipated wall shear stresses found on the FTF-II plate are plotted for each of the flight profiles in Figure 6. At higher altitudes, the ambient pressure and temperature will decrease. Thus, the dynamic pressure will be less for the aircraft moving at the same Mach number, and the wall shear will decrease with altitude. Also, as the Mach number increases, the shear forces will increase according to the Equation 3.

$$\tau_w = C_f q = C_f (\frac{1}{2} P_s \gamma M^2) \qquad [3]$$

Where τ_ω represents the wall shear stress, q represents the dynamic pressure, C_f represents skin friction coefficient, P_s is the static pressure, γ is the specific heat ratio, and M is the Mach number.

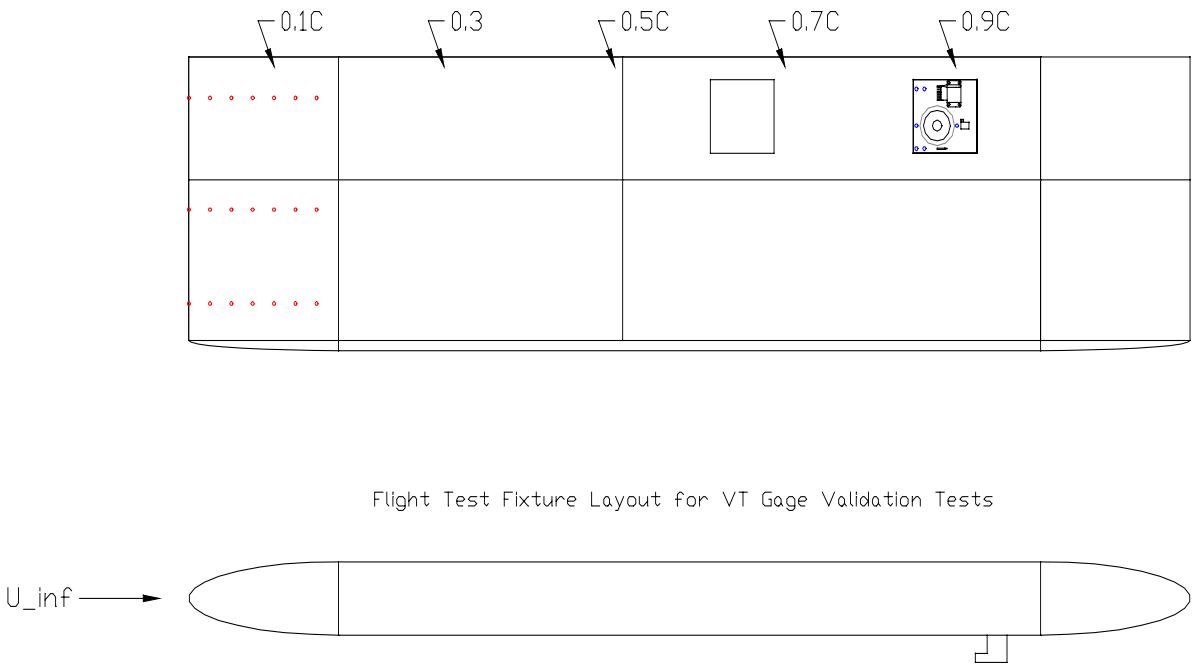

Figure 7: Proposed F-15/FTF-II Configuration

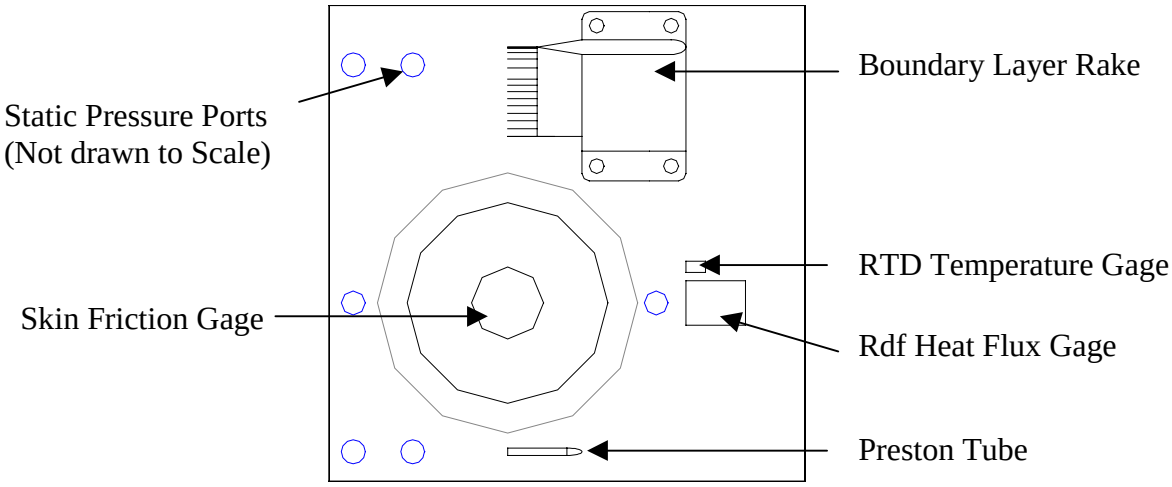

Figure 8: Details of Sensor Complex

NASA has also provided sketches of the location of the skin friction gage for future tests on the FTF-II flight test plate. Figure 7 and Figure 8 are of the anticipated location of the skin friction gage on the flight test plate drawings provided by Dr. Trong Bui of the NASA Dryden Research facility. Figure 8 shows the location of the gage as well as the location of a variety of other sensors that may be tested simultaneously during flight tests.

1.3.3. Approach

Of the seven damping mechanisms previously explored to replace the oil fill, three methods were researched further. It was concluded that the first option to be tested would be a damping mechanism utilizing air in small gaps as a damping mechanism. This was chosen, because the effects of the severe vibration on current skin friction gages were unknown. This method used a configuration with only minor changes from previous designs where vibration was not considered in great detail during the design process. It would produce results that would identify the severity of the vibration issue, yet employ a design that would not necessitate a great deal of change in future configurations.

The second method chosen to be tested was an eddy current damped configuration with a permanent magnet. This method possesses several positive characteristics. The inherently passive damping system requires no additional power sources. The small magnets can also be placed inside the gage without increasing the gage size to the point that it becomes too bulky.

Depending on the success of the permanent magnet concept, the third choice would be the eddy current damped configuration utilizing an electromagnet. This configuration maintains most of the benefits of the permanent magnet configuration. There would be some disadvantages though. The size of the gage would increase due to the large size of the electromagnet. Also, the electromagnet would require a power source in order to operate. Heating could become a concern as well. But, it possesses a variety of other important benefits beyond those of the permanent magnet concept. First and foremost, an electromagnet is capable of producing a significantly larger level of magnetic flux density and consequently greater damping. This method would allow the damping of the gage to still

be passive, yet the level of damping could be controlled by the amount of current that was allowed to pass through the electromagnet. It could eventually become tunable. If the concept was successful, an active system could be adapted into the system in a later design.

Experiments were first set up to measure the vibration performance of the gage under the flight conditions which NASA anticipated on the FTF-II plate (see Figure 5). The goals of the skin friction gage vibration experiment were three fold. First, the natural frequencies of the gage were to be measured and analyzed. The strain gage output amplitudes at those natural frequencies were also to be measured to determine if the gage head would hit the wall with the anticipated flight vibration loads. If those natural frequencies fell within the 15-2000 Hz frequency domain expected during the F-15 flight, then a damping method would be used to decrease the effects of those natural frequencies. The second goal of this experiment was to shake the skin friction gage following the NASA vibration test requirement curve A (Figure 5) in order to determine if the shaking of the F-15 during its flight would cause vibration output comparable to the expected output due solely to the skin friction loading. If the vibrations caused a comparable or greater output than the expected output due to skin friction, then methods of altering the undesirable vibration characteristics would be needed. The damped configuration would be tested and compared to the undamped case. If damping was not adequate, then other means of decreasing the effects of those natural frequencies were to be explored. The third goal of this experiment was to shake the skin friction gage following a less strenuous vibration test requirement curve in order to determine if the shaking of the F-15 during a smooth flight would cause vibration output comparable to the expected output due solely to the skin friction loading. This experiment was done in the same manner as the tests for the second goal except with a 2 g_{rms} loading instead of an 8 g_{rms} loading. The damped configuration was then compared to the undamped case, and the effects were to be analyzed.

A final wind tunnel experiment was planned to verify the operability of the gage. The gage would be mounted in the Virginia Polytechnic Institute and State University supersonic wind tunnel. It would be tested at comparable shear levels of τ_w=3.5-4.0 psf, at M=2.4, P_o=55 psi, T_o=300 K, and Re/m=4x10^7. These shear level values were slightly larger of than the shear levels on the F-15 flight test plate during the flight test, but adequate for verification purposes.

Chapter 2. Theory

2.1. Skin Friction Theory

The pertinent skin friction equation involved comes from Equation 1 which, when rearranged, produces the desired variable.

$$C_f = \frac{\tau_w}{q} = \frac{\tau_w}{(\frac{1}{2} P_s \gamma M^2)} \qquad [4]$$

Since the gage produces a voltage output, a calibration curve relating voltage to shear force is required. This linear calibration curve is determined by hanging known weights attached to the head and plotting the corresponding voltage output. A thorough description of the calibration procedures can be found in Chapter 3.3, Calibration Procedures. This gage specific calibration is utilized so that the voltage can be related to a shear force (psf). This shear force value is used in conjunction with the measured static pressure, and the calculated Mach number of the flow over the gage during testing to calculate a skin friction coefficient value.

A calculation of the skin friction coefficient based on the boundary layer thickness at the balance location was used to compare with the experimental values. This was done by first finding the boundary layer thickness using Pitot pressure profile data. Then, the empirical Schultz-Grunow relation for the skin friction coefficient of wall-bounded incompressible turbulent boundary layers was used to get an initial estimate.

$$C_f = 0.0456(\mathrm{Re}_\delta)^{-0.25} \qquad [5]$$

This relation is valid up to approximately $Re_x=10^7$. The flow of interest is obviously a compressible flow. Therefore, the estimate can be refined with the incompressible to compressible relation from Van Driest. This relationship is based upon experimental data and calculation for a given Reynolds number [38]. A theoretical skin friction value of approximately 0.0017 was calculated for the experimental supersonic wind tunnel runs.

Van Driest [39] produced turbulent skin friction drag coefficient results from flat plate studies as a function of Reynolds number and Mach number. The turbulent data is plotted against laminar results for contrast in Figure 9. For a flat plate, skin friction values tend to decrease as Reynolds number increases and also as Mach number increases. The skin friction decreases more rapidly for cases in which the flow is laminar instead of turbulent.

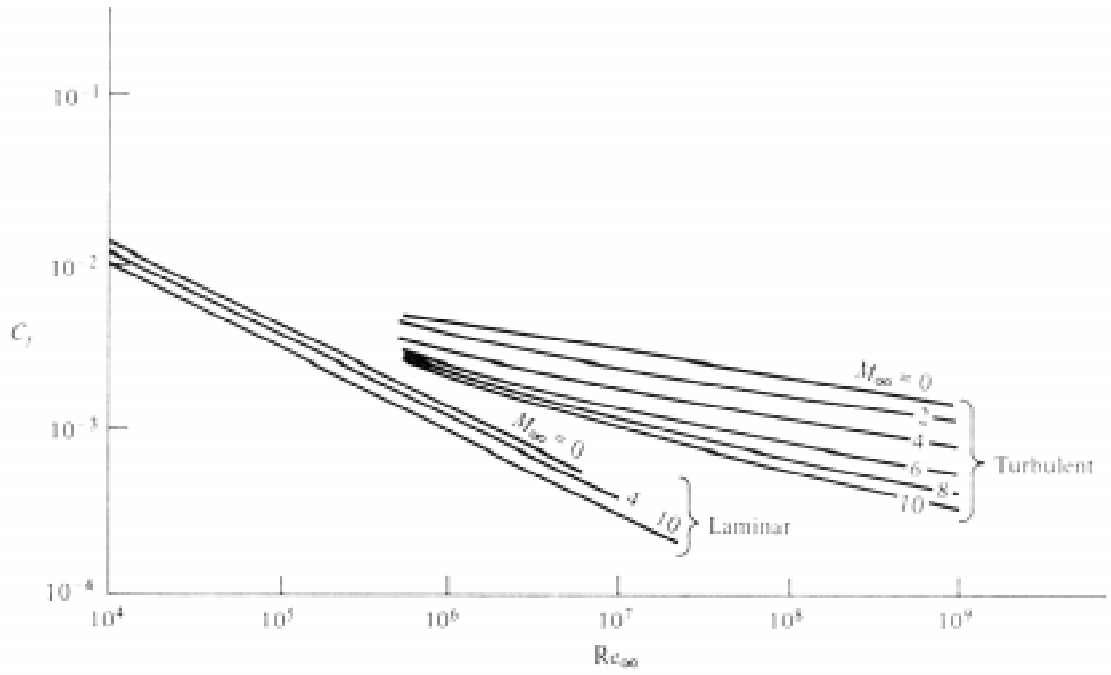

Figure 9: Skin Friction Drag Coefficient for a flate plate [1]

2.2. Experimental Vibration Theory

The fundamental theories underlying the principles of the vibration methods used in this study can be found in most modern vibration textbooks. Three textbooks [40],[41],[42] describe the system dynamics of a cantilevered beam experiencing a forced random noise vibration.

The vibration measurement techniques applied throughout this study come from experimental modal analysis [33]. The major reasons for performing vibration tests are to determine natural frequencies, verify analytical models, and verify the survivability of the gages in extreme vibration environments. The vibration test methods discussed depend on several assumptions. It is assumed that the structure or machine being tested can be

described adequately by a lumped parameter model. There are several other common assumptions made during testing. Most importantly, the system being tested is assumed linear and is driven by the test input only in its linear range.

The basic hardware elements required consist of a source of excitation, called an exciter, for providing a known or controlled input force to the structure, a transducer to convert the mechanical motion of the structure into an electrical signal, a signal conditioning amplifier to match the characteristics of the transducer to the input electronics of the digital data acquisition system, and an analysis system in which signal processing and modal analysis computer programs reside. A schematic for the modal testing of the gage is shown below in Figure 10. Complete details of the experimental setup are contained in Chapter 4.1, Vibration Test.

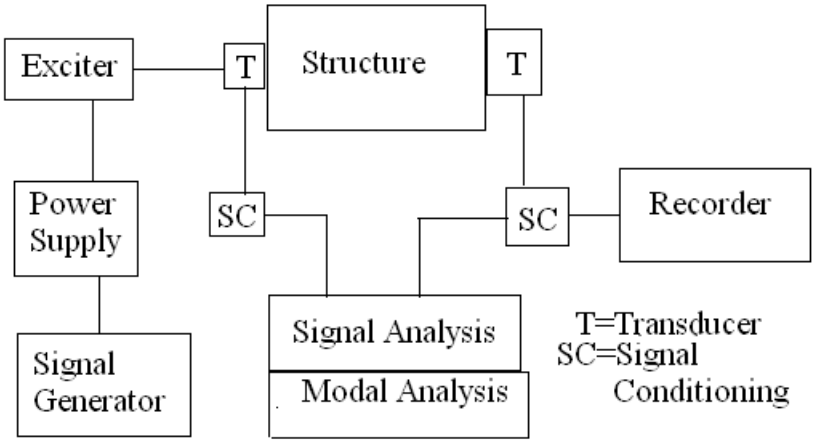

Figure 10: Schematic of Hardware used in performing the Vibration Test [33]

For the experimental testing performed in this study, the arrangement includes a power amplifier and a random signal generated from a spectral analyzer. The exciter used is an electromagnetic modal shaker that has the ability to provide inputs large enough to result in easily measured responses utilizing an easily controlled electronic output with force feedback. The electromagnetic modal shaker is basically a linear electric motor consisting of coils of wire surrounding a shaft in a magnetic field. An alternating current applied to the coil causes a force to be applied to the shaft, which, in turn, transfers force to the structure. A voltage from the signal generator causes a proportional force to be applied to the test

structure. Thus, the signal generator can provide a variety of input signals to the structure. The structure is mounted to the shaker with a stinger, which minimizes the effects of mass loading. The stinger isolates the shaker from the structure, reducing the added mass, and causing the force to be transmitted axially along the stinger, controlling the direction of the applied force. An impedance head is used in these experiments as well. It consists of a force transducer and an accelerometer. A signal conditioning amplifier is used to manipulate the signal into an appropriate form. Once the response signal is properly conditioned, it is routed to an analyzer for signal processing. The same dynamic signal analyzer that generates the random signal also processes the output signal using a Fast Fourier Transform Analyzer. This analyzer accepts analog voltage signals of acceleration, force and strain from the signal conditioning amplifiers and filters and digitizes it for computation. The discrete frequency spectra of the individual signals are computed in addition to the cross-spectra between the input and various outputs. These processed signals are then presented in the pertinent graphical formats required such as power spectral density plots, frequency response functions, phase plots, coherence and time history plots.

The coherence function is essentially a measurement of the similarity of the signals. The transducer used to measure the input and output during a vibration test contains various levels of noise. If the coherence function equals zero, then the measurement is pure noise. If the function equals one then the signal is not contaminated with noise. In practice, data with a coherence of less than 0.75 are not used [33].

The damping ratio associated with each peak of a natural frequency is assumed to be the modal damping ratio, ζ, in the modal coordinate system. For systems with light enough damping such that the resonances are defined, the modal damping ratio is related to the frequencies on the magnitude plot according to the half-power relation [43].

$$\zeta = \frac{f_b - f_a}{2f_d} \qquad [6]$$

f_d represents the natural frequency of the damped signal, f_b and f_a represent the frequencies of the at .707 times the magnitude of the signal at the natural frequency.

Aliasing and leakage are two problems that are common when discussing digital signal processing of vibration data. Aliasing is caused by sampling the data at an improper time interval. If the sampling rate is too slow to catch the details of the analog signal, then

the digital signal will represent the high frequencies as low frequencies. In order to avoid aliasing issues, the sampling interval must be small enough to provide at least two samples per cycle of the highest frequency to be calculated. Leakage stems from the finite sampling period over which a signal is analyzed. There is no convenient way to make a complicated signal finite while cutting off the signal at an integral multiple of its period. Because signals are cut off at mid-period, erroneous frequencies may appear in the digital representation of the digital Fourier transform. The actual frequency will leak into a number of fictitious frequencies, because the finite signal assumes that the signal is periodic within the sample record length. This error can be corrected by the use of window functions. The most prevalent window function for leakage correction is the Hanning window. These windows multiply the original analog signal by a weighting function, or window function, w(t), which forces the signal to be zero outside the sampling period [44].

2.3. Beam6 Code Theory

A computer-aided design program for beam analysis called BEAM6 was used during this study. This version was developed in 1992 under Prof. Mitchell at the Virginia Polytechnic Institute and State University. The program was designed for beam and rotor analysis using the Transfer Matrix Method. An in-depth review of the theory involved is available in the BEAM6 User's Guide [45]. Essentially, this method is based on the principle that a complicated continuous beam can be segmented into component parts. Each segment consists of simple elastic and dynamic properties that can be expressed in a matrix. These component matrices, when fitted together by successive matrix multiplication can be evaluated with the proper boundary conditions that will result in the response of the entire beam. It provides the following analysis for a damped and undamped beam or circular whirl rotor system of arbitrary configuration.

1) Free Vibration (eigenvalue-eigenvector analysis)
2) Static Response with Stress Analysis
3) Forced Dynamic Response (damped or undamped) at a particular frequency over the entire structure with stress analysis
4) Frequency Response (damped or undamped) at a point on the structure for a specified frequency range with stress analysis.

This program required a computer model, which incorporates the material properties of the gage, the gage geometry, as well as the anticipated damping and loading that the gage would experience. From this model, the program can predict the natural frequencies and dynamic vibration characteristics.

The program is capable of simulating a random noise vibration of a desired intensity, and calculating the transfer function. This transfer function is then used to calculate the dynamic response of the gage according to Equation 7.

$$G_{yy}(\omega)=|H(\omega)|^2 G_{xx}(\omega) \qquad [7]$$

Here, the function H represents the transfer function from the BEAM6 program. G_{yy} represents the power spectral density (PSD) output of the response, and G_{xx} represents the PSD of the input driving force, which is known. G_{xx} can be related to the NASA vibration curve A. In which G_a represents the curve A. Thus, the relationship for G_{xx} can be represented by Equation 8.

$$G_{xx} = G_a\left(\frac{g}{(2\pi f)^2}\right)^2 \qquad [8]$$

This program was useful in determining the structural vibrations of the skin friction gages. In this manner, a variety of potential designs can have their vibration characteristics evaluated before the hardware is actually manufactured. This saves time and money. The computer analysis program does possess some weaknesses. It is unable to incorporate visco-elastic materials into the theoretical model, which causes some modeling inaccuracies. BEAM6 did prove to be a valuable tool in the process of designing skin friction gages.

2.4. Electromagnetic Theory

The fundamental electromagnetic field equations pertaining to the design and analysis of an eddy current damper for use in a skin friction gage are derived from Maxwell's

equations [46]. These equations can be simplified to produce an effective eddy current damping coefficient.

B is the basic magnetic field vector called the magnetic induction or magnetic flux density in Gauss or Tesla (Webers/meter^2). The definition of B is as follows: If a positive test charge q_o is fired with velocity U through a point P and if a (sideways) force F acts on the moving charge, a magnetic induction B is present at point P, where B is the vector that satisfied the relation.

$$F=(q_o)U \times B \qquad [9]$$

Faraday's Law of Induction says that the induced emf, ξ, in a circuit is equal to the negative rate at which the flux through the circuit is changing.

As an example, consider Figure 11, which shows a rectangular loop of wire of width L, one end of which is in a uniform magnetic field B pointed at right angles to the plane of the loop.

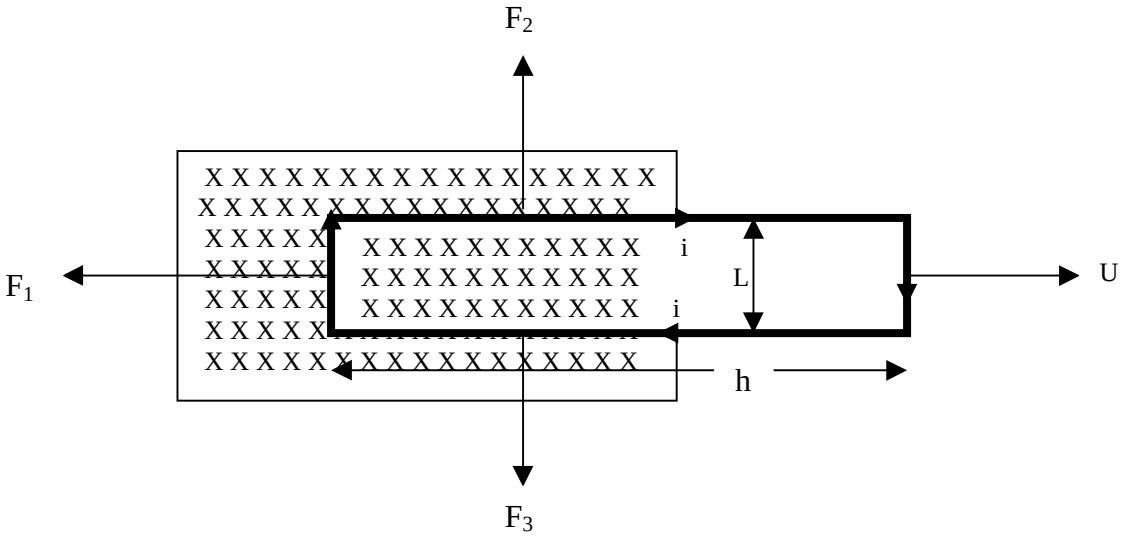

Figure 11: A Rectangular Loop is Pulled out of a Magnetic Field with Velocity, U, and Current i Flowing Through the Loop.

This B field may be produced in the gap of a large permanent magnet or an electromagnet. The box shows the assumed limits of the magnetic field. The experiment consists of pulling the loop to the right at a constant velocity, U. The flux, ϕ_B, enclosed by the loop is

$$\phi_B = BLx \qquad [10]$$

From Faraday's Law, the induced emf, ξ, is

$$\xi = \frac{-d\phi}{dt} = \frac{-d(BLx)}{dt} = -BL\frac{dx}{dt} = BLU \qquad [11]$$

This induced emf sets up a current in the loop determined by the loop resistance R.

$$i = \frac{\xi}{R} = \frac{BLU}{R} \qquad [12]$$

From Lenz's Law, this current must be clockwise in the above Figure 11, since it opposes the change (the decease in ϕ_B) by setting up a field that is parallel to the external field within the loop. The current in the loop will cause forces to act on the three conductors, as given by Equation 9. Because F_1 and F_2, are opposite they cancel each other. F_1, the force that opposes any effort to move the loop, is given by Equation 13.

$$F_1 = iLBSin(90^o) = \frac{B^2L^2U}{R} \qquad [13]$$

The resistivity, ρ_e, is a characteristic of the material rather than a particular specimen of the material. Since the resistance of an electrical conductor is directly proportional to the length of the conductor and is inversely proportional to the cross sectional area, it is related to the resistivity as follows:

$$R = \frac{\rho_e L_{loop}}{A} = \frac{\rho_e(2h + 2L)}{A} = \frac{2\rho_e(h + L)}{A} \qquad [14]$$

Thus, substituting this relation for the resistance, R, into Equation 13 yields

$$F = \frac{B^2 L^2 AU}{2\rho_e (h + L)} = \frac{B^2 LAU}{\rho_e \left[2\left(1 + \frac{h}{L} \right) \right]} \qquad [15]$$

This force is directly opposite to the direction for motion of the conductor and could be considered as the eddy-current damping force. This force is proportional to the velocity. The damping coefficient, C_d, can be calculated by introducing a constant of proportionality.

$$F = C_d U \qquad [16]$$

The damping coefficient, C_d, can therefor be assumed to be

$$C_d = \frac{B^2 LA}{\rho_e} \left[\frac{1}{2\left(1 + \frac{h}{L} \right)} \right] \qquad [17]$$

Where B is the magnetic flux density in Teslas. L represents the length of the conductor in meters. A is the cross section of the conductor in meters^2, and ρ_e represents the resistivity of the conductor material in ohm-meters. In many textbooks and papers (See for example [35],[36],[47]) the damping coefficient is expressed with a factor K which takes into account losses from the configuration of the damper and other potential losses due to imperfections in real applications which extend this principle beyond the rectangular wire in the magnetic field example. This K factor is an extension of the factor found in brackets in Equation 17. Here a square loop of wire would have a factor of 0.25 associated with it.

$$C_d = K \frac{B^2 LA}{\rho_e} \qquad [18]$$

Some textbooks assume that the factor K=0.3 [34]. Many scientists believe that there are losses associated with real applications which require the factor K to be smaller, expecially when a disk made of a conducting material replaces the rectangular wire from Figure 11. The

equivalent value of this constant has been analytically estimated to be between 0.0 and 0.25 for a various geometries of the "C" configuration eddy current damper according to Nagaya and Kojima [47]. Some recent research has anticipated that the range of this value is much harder to predict. Gunter, Humphris and Severson [36] found that the losses associated with this constant when this principle is used in real world applications are much larger. The values they found experimentally were considerably less than the theoretical predictions. A paper by Weinberger [48] realized that the exact calculation of the drag force exerted by an eddy current damper in a realistic configuration is a difficult problem and attempted to derive a solution utilizing the geometry of the concept, but for a less general case than that of Nagaya and Kojima [47].

The application of these laws, which produce eddy-current dampers and electromagnets, date back to late 1700's. There are myriads of textbooks, which discuss the design, use, and application of magnetic devices. These tools range from magnetic brakes to magnetohydrodynamic power generators, but they are all based on the same fundamental principles. A great deal effort has been focused on the refinement of the applications of these tools. Of particular interest in this study were books that discussed the application of permanent magnet devices [35], [49], [50]. Also of interest were devices and studies involving electromagnets [51], [52]. Cherry found the eddy current concept useful in his application in the aircraft industry [53]. He found that the vibration of skin sections of an aircraft fuselage are subject to intense sound levels which require damping in order to prevent rapid fatigue of the metal. He used electromagnetic induction damping to reduce the amplitude of vibration of the skin section using a unique aluminum ring configuration. More complicated concepts which improve current structural vibration absorbers have been researched as well. Research has focused on servo vibration dampers [54] and a new type of dynamic vibration absorber consisting of three permanent magnets [55]. A great deal of effort has also been put into exploring the family of smart magnetic tuned-mass dampers [56].

Many of these tools and applications of magnetism require higher levels of magnetic flux density in order to produce acceptable results. When this is the case and permanent magnets produce an inadequate level of magnetic flux density, then often electromagnets are the answer. They are able to produce a greater level of magnetic flux density, and the magnetism can be turned on and off. The trade-off is in the bulkiness of the electromagnet.

An electromagnet can easily become too large for an application. This is due to the number of wraps of wire around the electromagnet core required to produce the desired flux. In addition, the cooling mechanisms that are recommended to keep the electromagnet from overheating can add size to the electromagnet as well. The principles behind this type of magnet are based on the same fundamental electromagnetic theories that were discussed above.

The magnetic flux density that an electromagnet can produce is rooted in its configuration, the number of wire wraps around the core, the material in the core, the gap size, the medium that the flux lines are flowing through, and the gap dimensions. For a "C" shaped configuration the flux density of the electromagnet is well understood. A magnet with an air gap (a "C" shaped configuration) has most of its magnetomotive force (mmf) dropped across the air gap. Figure 12 shows this configuration as a toroidal core with an air gap of length l_g.

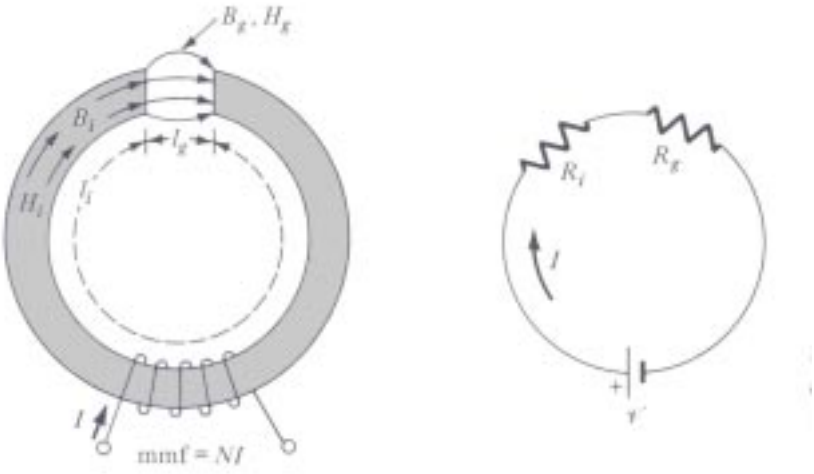

Figure 12: "C" Shaped Electromagnet Configuration [52]

The magnet can be described with an analogous electrical system, in which the toroid and its gap are a series circuit. Thus, Kirchoff's law for a magnetic circuit of this type can be approximated as

$$mmf = \phi R \cong \phi R_{gap} \qquad [19]$$

where ϕ represents the magnetic flux, and $\mathcal{R}$ represents the reluctance. The electromagnet possesses a concentrated winding with a current flowing through it that serves as the source of mmf. The same flux flows through the iron as flows through the gap.

$$\phi_i = \phi_g \qquad [20]$$

the series then becomes

$$mmf = \phi\mathcal{R} \cong \phi(\mathcal{R}_{core} + \mathcal{R}_{gap}) \qquad [21]$$

$$mmf = \phi\left(\frac{l_i}{\mu A_i} + \frac{l_g}{\mu A_g}\right) = \frac{\phi}{\mu A}\left(\frac{l_i}{\mu_r} + l_g\right)_{A_i=A_g} \qquad [22]$$

$$mmf = \frac{B}{\mu_o}\left(\frac{l_i}{\mu_r} + l_g\right) \qquad [23]$$

For this case, the relative permeability of the ferromagnetic core is given by $\mu_r=\mu/\mu_o$, and the areas of the core and the gap are identical $A_i=A_g=A$. Remember from the fundamentals of electromagnetism that mmf=Ni and the flux are related by ϕ=BA.

$$B = \frac{\mu_o Ni}{\frac{l_i}{\mu_r} + l_g} \qquad [24]$$

If the core is made of a material with a high permeability like iron or hiperco, then μ_r is an extremely large value as much as $\mu_{r\text{-iron}}$= 2000 or $\mu_{r\text{-hiperco}}$ = 10,000 [52], [57]. Consequently, $l_i/\mu_r \ll l_g$ for most practical gap geometries. Thus, Equation 24 can be reduced to

$$B = \frac{\mu_o Ni}{l_g} \qquad [25]$$

Equation 25 is an extremely useful relationship for use in the design of electromagnets. If an electromagnet needs to produce a specific level of magnetic flux density, then a design can be created utilizing the design size limitations and power restrictions.

2.5. Eddy Current Optimization Theory

The analysis used for the optimization of an eddy current damper follows the work of Mikulisnksy and Shtrikman [58]. The analysis studied the optimization of an eddy-current damping device that contained a metal disk moving in a magnetic field of cylindrical symmetry. This theory was then further tested in 1983 by Gunter, Humphris and Severson with cryogenic turbomachinery at the University of Virginia [36]. This theory accounted for the geometry and materials used in the configuration. It was discovered that the geometry of the eddy current damper was a vital aspect of the configuration. The damper needs to be sized to precise specifications, otherwise dramatic losses occur. The general optimized configuration consists of a cylindrical conducting disk moving perpendicular to the flux lines induced by 4 separate magnetic rings as shown in Figure 13. The poles of the primed and non-primed rings are oriented in opposite directions. Each small, gray arrowhead points to in the direction of the polarity. The various radii and lengths have a profound effect on the performance of the gage.

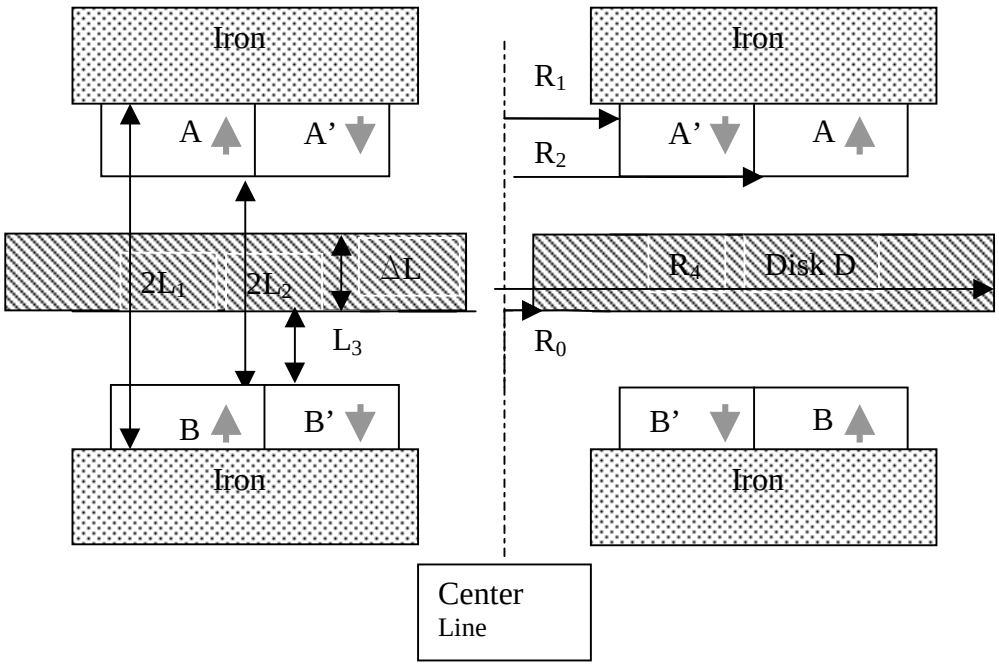

Figure 13: Optimized Eddy Current Configuration

The analytical equations, which were used for the derived damping equations, were a result of a wide range of geometrical parameters. The geometry that produces the maximum damping under size constraints was then obtained. After an involved derivation, the final result of the damping coefficient for the optimized geometry is as follows

$$C_d = \left(\frac{4\pi M^2}{27\rho_e}\right)\left(\frac{(L_1 - L_3)^3}{L_1^{\,2}}\right)\left(R_3^{\,2} - R_1^{\,2}\right) \qquad [26]$$

To obtain the maximum damping coefficient, C_{do}, the following parameters should be used

$$\left(\frac{R_2}{R_3}\right)^2 = 0.5 \qquad [27]$$

$$\Delta L = L_1 - L_2 = \frac{2}{3}(L_1 - L_3) \qquad [28]$$

Chapter 3. General Gage Description

3.1. Overview

This entire study utilized a general gage design that was modified in an attempt to improve the performance of the gage. In general, all the gages were designed following the direct skin friction measurement approach using a non-nulling design. The configuration utilized a floating wall sensing element attached to a cantilevered beam surrounded by a small gap. Figure 4 shows the general configuration for the gage used in this study. The top surface of the sensing head is mounted flush with the wall, so that it does not disturb the flow which it is measuring. The floating element responds to shear from the tangential flow that passes over it. This shear force acts on the floating head sensor and causes a deflection in the cantilevered beam to which the head is attached. The cantilevered beam is instrumented with a strain gage unit. The extended length of the cantilevered beam increases the effective length of the moment arm of the sensor. This results in an increase in the resolution of the gage. This moment arm can be altered in conjunction with the diameter of the sensing head to produce the desired sensitivity. If the diameter of the head increases for a specific test, then the effective moment that the strain gage unit experiences increases as well. This produces a useful design tool to alter the size of the gage and still be able to maintain the desired sensitivity.

A sensitive instrument is required to detect the small shear forces, which cause the floating element to deflect. Thus, a sensitive semi-conductor strain gage unit produced by Kistler-Morse was employed. For the flight tests which this gages was designed for, the gage must have a sensitivity capable of measuring surface shear forces on the order of τ_w= 0.3 to 1.5 psf. This should produce the equivalent of hanging 1 to 5 grams off the head during calibration. Also, for the wind tunnel verification tests with an estimated dynamic pressure of q=13.77 psi, and typical C_f values, the anticipated shear level was approximately 3.96 psf. The wind tunnel verification tests required a reduced floating head diameter. With this reduction in head size, the gage must be able to accurately measure a weight of 0.614 grams from the head.

The gages are made out of aluminum. This is the same material that is on the plate surface of the FTF-II plate and supersonic nozzle test plate. It is important to keep the gage material consistent with the test surface that it is being mounted to for a variety of reasons. Different materials would possess different characteristics when exposed to a temperature change. The thermal expansion might become an issue as well as the heat transfers through the material.

An Omega brand type K thermocouple was mounted in each skin friction gage studied. The thermocouple was mounted as close to the strain gages as possible without damaging them. At this location, the temperature of the strain gages could be monitored. This is important due to the temperature sensitivity of the semi-conductor strain gages.

The variations in the gages designed for this study are centered on the damping mechanism used to provide improved vibration characteristics and increased survivability of the gage. Consequently, these damping mechanisms drove the sizing requirements of each gage. Each gage looks different because of this.

3.2. Strain Sensor System

The strain sensing gages that were used in this study were the Kistler-Morse Deflection Sensor Cartridge (DSC). It is a complete multipurpose displacement transducer. It has a variety of features that make it a useful method of measuring strain for this application. First and foremost, these units are not costly. They eliminate the tedious task of attaching strain gages to the cantilevered beams during assembly. The strain gage unit is extremely sensitive and can measure minute levels of strain, yet it is stiff enough so that the movement of the floating head is minimal. In addition, the DSC is small enough (max. length = 1.5 in., max diameter = 0.25 in.) to be used in these application. The dimensions are shown in Figure 14.

Figure 14: Kistler Morse DSC Unit

The DSC also produces a linear deflection with force. The particular model used for this study was the DSC-6 sensor. It is sensitive on two axes, so that it can accurately measure the wall shear in two orthogonal directions simultaneously. Two gages are mounted on each axis 90^o apart. The sensor is made of piezo-resistive strain gages. As the steel beam deflects, so do the crystals, the strain in the DSC is measured due to the consequent change in resistance within those crystals. One side of the beam goes into tension while the other side goes into compression. The strain gages possess a 1000 Ω resistance. The DSC can sense a deflection at the tip of the unit, up to a maximum of 0.012 in. with a linearity +/- 0.05%. Beyond 0.012 in., the gage will be damaged and render erroneous results. This makes it important to incorporate stoppers into the design of the gage, which inhibit the gage from experiencing deflections beyond its maximum capacity. The deflections caused from the anticipated shear levels ($\delta=10^{-4}$ in.) will be well below the maximum deflection. The undamped vibration levels expected during some vibration testing could become dangerously large on the order of $\delta=10^{-3}$ in.

The gage is axisymmetric, which allows for greater versatility in testing. This allows for more freedom when orienting the gage. Due to the sensitivities of the strain gage, the orientation of the gage with the flow remains a concern. The best results come from orientations in which the one axis is completely aligned with the flow. The gage possesses regions of sensitivity, which do not produce exact two-dimensionally orthogonal output components. Figure 15 shows the region of sensitivity of a single axis strain gage. Finally, it must be noted with regret that these units are no longer a standard item with the Kistler-Morse Corp.

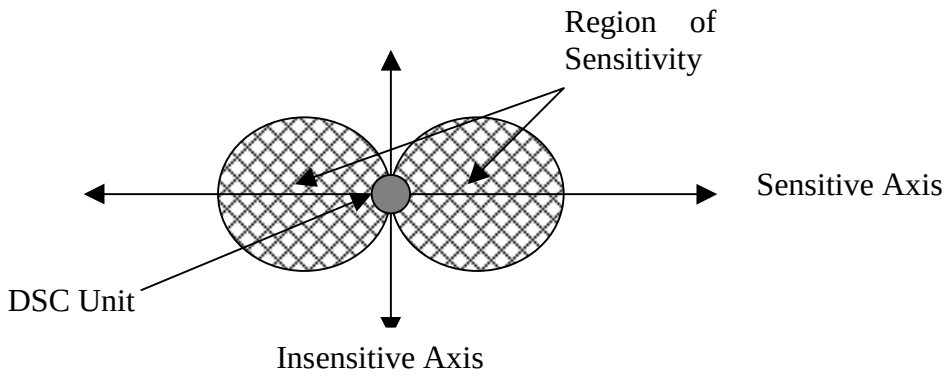

Figure 15: Sensitivity Regions of Single Axis DSC-6 Unit

The block diagram, shown in Figure 16, is the same for the wind tunnel test and flight test as well as the gage calibration.

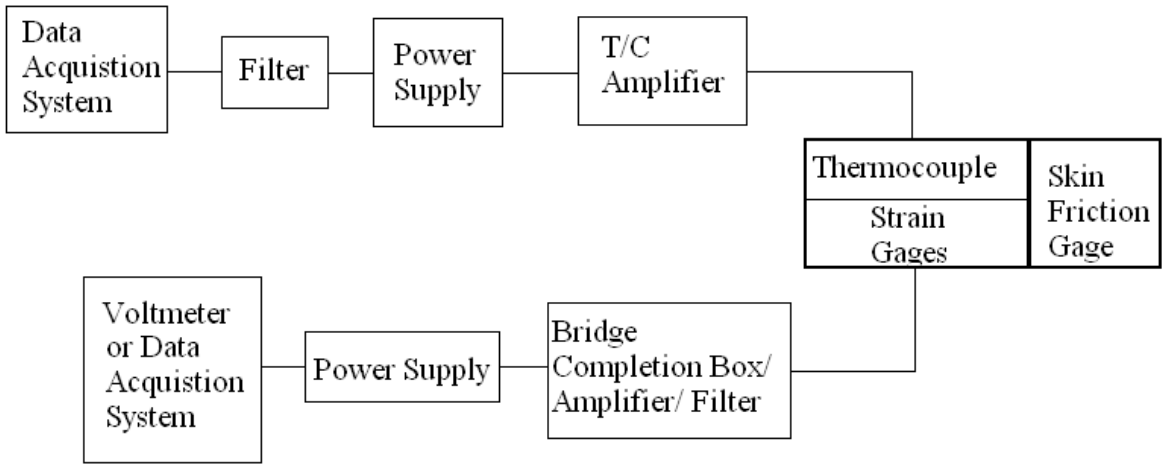

Figure 16: Block Diagram of Electrical Setup for Gage Calibration and Testing

In order for the experimental set-up to operate correctly, each axis of the gage must be wired directly to a bridge completion box found in a signal conditioning amplifier which converts the signal to an output voltage. The resistances inside the DSC-6 strain gage unit form two half-bridges perpendicular to one another. The bridge completion box contains the two other half-bridges which complete the bridge. The bridge sensor also contains a potentiometer for zeroing the signal from each axis. The unamplified voltages were then amplified by the signal conditioning amplifier 100 times, so that the signal could be more manageable. It could then be filtered by the signal conditioning amplifier for signal processing purposes. For calibration purposes, the skin friction gage output was then linked to a multi-meter, so that the resultant voltage could be recorded. Only a digital multi-meter was required for the data gathering of the calibration, because the calibration consisted of hanging a static weight on the floating head. The result should be a stable voltage. Thus, an intricate data acquisition system was not required.

For the wind tunnel verification tests, a more involved data acquisition system was required. The gage was linked from the wind tunnel to the signal conditioning amplifier to a data acquisition board which was capable of sampling the data at a high rate (100 Hz). The

output voltages were read into a Labview program, which plotted the voltage output of the skin friction gage with time, along with temperature and pressure readings in the tunnel.

The thermocouple mounted next to the strain gages was used to monitor the temperature so that temperature effects could be accounted for. This thermocouple was linked to a thermocouple amplifier and a power source which was put together in the AOE electronics shop. The data could be filtered through a Multimetrics, Inc. Model AF 420L Active Filter for signal processing purposes. It was also linked to a data acquisition system using the Labview program, so that the temperature history could be seen.

3.3. Calibration Procedures

A simple calibration procedure was established at Virginia Tech for the calibration of skin friction gages. Figure 17 shows the calibration setup.

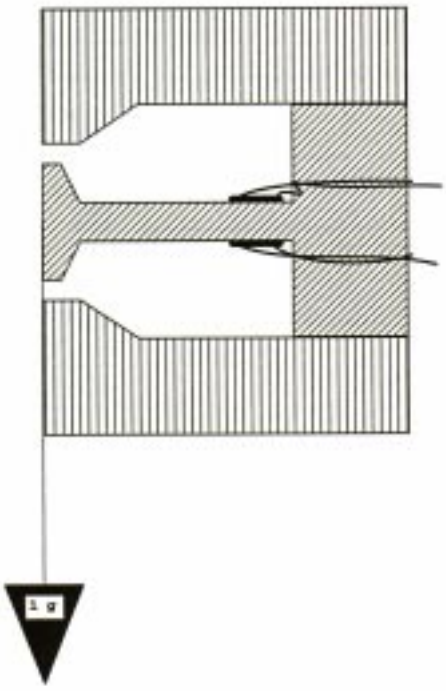

Figure 17: General Skin Friction Gage Calibration Setup [14]

The procedure involved hanging weights from a tare attached to the floating sensing element along the measurement axis of the gage. This direct force method was performed by placing the unit in a horizontal position, so that the desired calibration axis could be deflected

in a vertical manner. Next, a tare was hung from the floating head by a thin line of thread. The strain gage output was then balanced, so that when the tare was empty, the gage output was approximately 0 mV. In this manner, the weight of the beam, head, and tare would not offset the calibration curve. Next, weights were added to the tare, and the consequent change in voltage on both the measured axis and the orthogonal axis were recorded from the voltmeter. If the off-axis strain gage was mounted perpendicularly, then the output would be near zero. It was found that the axis mounts had imperfections which lead to an off-axis output of 4.8 % of the streamwise output. Next, larger weights were added into the tare with care. It was important to place the weights gently into the tare, so that pendulum motion did not begin. If a pendulum motion was excited, then the output of the strain gage would not settle for a period of time. After each weight had been removed, it was important that the strain gage output signal returned to the same zero. Thus, the response of the gage was found to be repeatable within the drift tolerances (approximately 3% of the total expected streamwise signal). After a variety of weights had been placed in the tare, and their respective outputs had been recorded, the gage was rotated 180^o, and the previous process was repeated. This was done to ensure that there was no sensitivity with the direction to which the load was applied. Next, the gage was rotated 90^o, so that the other measurement axis could be calibrated. Again, the axis was checked in both directions to ensure that there was no sensitivity with the direction to which the load is applied. The DSC-6 strain gages exhibited a linear relationship between voltage output and the calibration mass. The desired output needed to be related with shear force instead of mass. The mass could then be related to shear force by the relation in Equation 29.

$$\tau_w = K*m/A \qquad [29]$$

Here, m represents the mass of the weights, A represents the area of the floating head, and K represents the conversion factor from grams to lb_f. Thus, the calibration plots will produce a line with an equation directly relating voltage to a shear force according to

$$\tau_w = C_1*V + C_2 \qquad [30]$$

V is the voltage output of the strain gage, C_1 represents the slope of the calibration curve, and C_2 represents the y axis intercept which is generally equal to zero when the gage has been

properly balanced during the calibration procedure. A least-squares regression on each of the skin friction gage calibration curves showed that these curves were highly linear. A typical calibration curve from the gages used in this study can be found in Figure 18. This calibration curve has an R^2 value equal to one. Each curve represents the linear relationship between voltage and shear stress for one direction of each axis. The plots are displayed in both shear stress and calibration mass terms for easier interpretation.

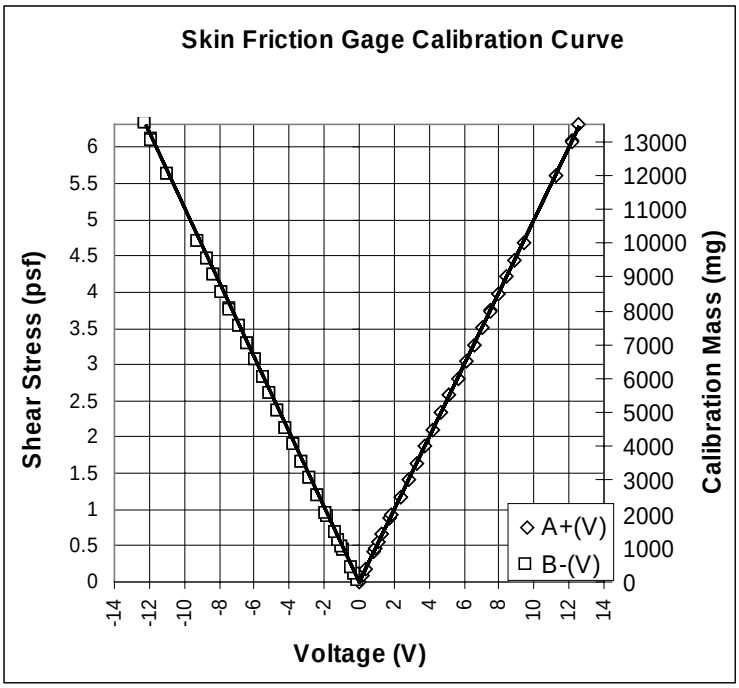

Figure 18: Sample Skin Friction Gage Calibration

3.4. Head Deflection

Another important assumption used for the analysis of this gage was the assumption of a linear relationship between the deflection at the head of the Kistler-Morse DSC unit and the force at the end of the sensing beam of the Kistler-Morse unit. This linear relationship stems from the assumption that the cantilever beam extension is much stiffer than the Kistler-Morse unit. Kistler-Morse relates this scheme to a spring mass damper system, and states that the unit has a spring constant of 50 lb_f/inch. Thus, if a deflection at the end of the Kistler Morse unit was known, then a deflection at the head of the gage could be related through a moment transfer assuming that the deflection is linear beyond the end of the Kistler Morse unit. This is illustrated in Figure 19.

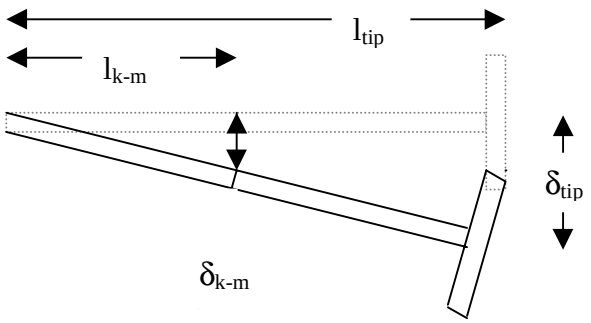

Figure 19: Gage sensor head deflection relationship

When calculating the deflection of the head, the equivalent force that the end of the Kistler-Morse unit experiences must be calculated by transferring the force at the head to a moment at the base. Then transforming that base moment to a force and moment arm at the end of the Kistler-Morse unit. From the equivalent force on the Kistler-Morse unit tip, a deflection at the end of the Kistler-Morse unit can be calculated using the known spring constant. Then using equivalent triangles, a deflection at the head can be deduced using Equation 31.

$$\delta_{head} = \left(\frac{l_{tip}}{l_{k-m}}\right)^2 \left(\frac{\tau_w}{k_{k-m}}\right)(A) \qquad [31]$$

The calculation of the deflection of the sensor head is vital because if vibration levels are severe, the gage could potentially have head sensor deflections that impact the housing. Deflections of this magnitude need to be avoided for survivability issues as well as measurement reasons.

3.5. Analysis of Errors

The uncertainty for this gage was analyzed following the uncertainty analysis methods outlined by Figliola and Beasley [59]. Measurement errors are typically grouped into three categories; calibration, data acquisition, and data reduction. From each of these categories a variety of errors sources are introduced.

The calibration of this gage produced error sources stemming from sensitivity to forward and axial rotation. When the gage head was rotated 90^{o} from the vertical to the horizontal, the error was within 2.0% for small rotations. The sensitivity to axial rotation was tested by mounting the gage horizontally and introducing small axial rotations. This test would demonstrate the error associated with inaccurate alignment of the axes with the flow during a wind tunnel test. Each of the strain gages had regions of sensitivity. The most accurate position would be testing a gage directly on an axis. In this manner, one strain gage would receive the full load and the other would not receive any strain. It was discovered that the output signal turned out to be within 1.5% of the full-scale signal for rotations of 10 degrees or less. Another error source that was present during calibration was the potential for the strain sensors to experience a drift induced by a temperature change. A calibration may take hours to perform, so it was important that the temperature of the strain gage unit was monitored. Fortunately, the calibrations were performed in a relatively stable temperature environment throughout the duration of the calibration. For the cases of this study, there were no measured temperature shifts during the calibration of any of these gages.

The errors associated with the actual act of measurement were referred to as data acquisition errors. These errors stem from actual sensor and instrument error, changes or unknowns in measurement system operating conditions, such as power settings and environmental conditions. For the skin friction gage, there were a variety of potential errors associated with the geometry of the sensing element, the thermal effects of the strain sensors, pressure gradient effects, and the most influential were the vibration effects.

The geometry of the floating head was a critical design consideration. The head could introduce a variety of error sources at the surface. A major design consideration involved the minimization of the errors caused by the misalignment of the head. Allen [60] wrote a summary of the error sources produced by the misalignment of the gage head. He found that the important parameters involved in the source of error stem from a misalignment of the gage head with the wall surface, the gap size between the head edge and the housing, and the lip size. The lip size involves the shape of the head. It describes the length of the region where the head diameter does not reduce from the maximum head diameter. The effects of these errors are illustrated in Figure 20.

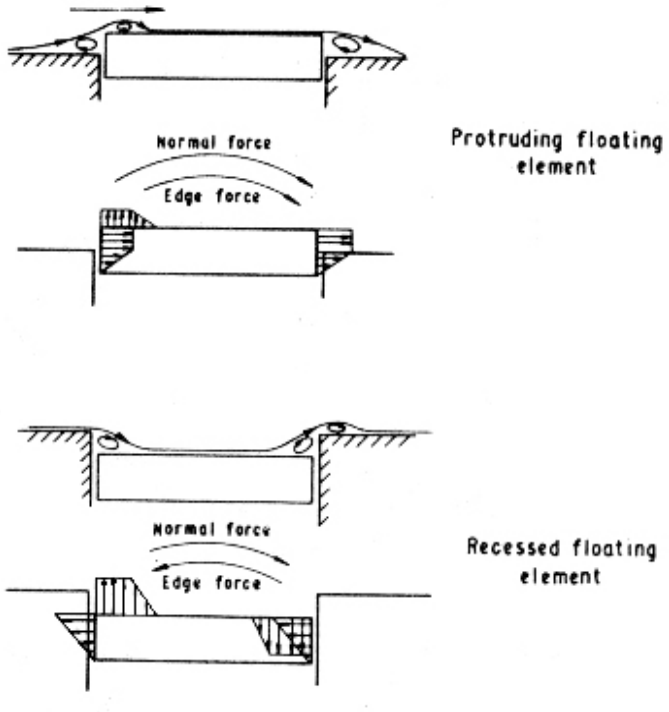

Figure 20: Misalignment Effects on a Floating Sensing Element [58]

Each gage used in this study was designed in an attempt to minimize the errors associated with misalignment. Allen relates all of these misalignment errors with boundary layer thickness. For the case of the wind tunnel verification, the boundary layer thickness was found to be δ=0.395 in. The gap size for the skin friction gages of this study were kept very small, approximately G=0.005 in. The first prototype had a head diameter of D=0.929 in., and the second prototype had a head diameter of D=1.5 in. The third prototype had two different head diameters. The first diameter was sized for the wind tunnel test at D=0.25 in., and second was sized for the vibration tests and flight tests at D=1.2 in. Each head was designed with a gap to head diameter ratio in a range that was relatively insensitive to misalignment. The G/D ratios for each prototype were 0.0053, 0.0033, 0.020, and 0.0042 respectively. When the misalignment was zero, the effect of gap size became negligible according to Allen [60]. His findings were somewhat counterintuitive, "The smallest gaps were found in the present study to be the most sensitive to misalignment, while the least sensitive were the largest" [60]. The Lip size of the head also produced an effect on the gage. It was found that a large lip size in conjunction with a small gap produced large errors; see Figure 10 of Allen's paper [60]. Thus, this design had a very small lip size in order to

minimize the possible errors. Each of these designs possessed a lip and gap ratio that produced a floating element insensitive to these uncertainty effects.

A common concern of these non-nulling designs was the effective error due to the tilt of the floating element when the beam deflects, called the protrusion effect. When the head tilts, it inevitably will enter the flow it is trying to measure. Fortunately, this concern was not an issue in this study due to the very small deflections of the sensing head. This negligible level of protrusion did not contribute to any noticeable pressure gradient effects. Allen claimed that protrusion effects were only an issue when the head protrudes 0.002 in. beyond the surface. In this gage design, the head protruded only a small fraction of that amount into the flow.

Thermal effects are another source of error. When the cantilevered beam increases in temperature, then a variety of errors arise. Most importantly, heat can be transferred down the length of the gage to the base of the beam where the strain gages are mounted. These strain gages are sensitive to small changes in temperature. There is a voltage drift associated with a temperature change at the strain gage. In addition to this, a concern with large temperature changes is the thermal expansion of the cantilevered beam. This could arise when air of a different temperature flowed over the head of the gage. The effect is more pronounced when the beam material was different from the wall material. The thermal expansion could potentially extend the sensing element into the flow stream, introducing additional protrusion errors. Thermal forms of errors are not a concern for this study, because during vibration and wind tunnel testing the gage temperature change was minimal. When the electromagnet was operational it only produced a temperature change after extended periods of operation (see Figure 60 and Figure 61), but due to the short 12 second operation of the wind tunnel tests, temperature effects were minimal. The error associated with this aspect of the testing produced only ± 1.0% error of the full scale signal. For potential flight tests at NASA Dryden, this source of error would affect the gage performance. The temperature change on the flight test plate ranges nearly 170^{o} F during a summer flight test. Due, to the fact that the gage and test plates are made of the same material, the errors associated with a temperature mismatch are minimal. The effects of the electromagnet on the flight tests would mean that a cooling system would be required, due to the long duration of the test flights. If the electromagnet were turned on for thirty minutes or

more without a cooling system, then the strain gages would experience a drift or possibly become damaged.

There is also a zero drift contribution associated with the uncertainty analysis. This is performed by monitoring the gage output periodically over an eight hour period, the signal was found to drift from the balanced zero level. This error was fairly small. It produced a voltage change which was ± 2.5% of the expected strain gage signal.

A major source of error associated with the output signal of the skin friction gage comes from the vibration levels which each gage encounters during testing. It was discovered during this study that a large continuous random noise vibration acting upon an operational gage could produce a large source of error. A large vibration interacting with an undamped gage was capable of producing noise levels orders of magnitude larger than the signal being measured. Attempts to average and filter this undamped data produce large levels of uncertainty in the output. Hence, a level of damping is required to stop the vibration from distorting the signal. Many of the damping mechanisms can produce output with smaller levels of error, but that magnitude of error is associated with the type of mechanism and the level of vibration. It was discovered that some of the best eddy current damping available was capable of reducing uncertainties due to vibration to ± 5.98 % during a smooth 2 g_{rms} vibration, and 24.0 % during an 8 g_{rms} vibration.

The final source of error that was associated with these measurements came from the data reduction. The errors associated with the calibration curve fits and truncation of data affect the overall skin friction measurement from the gage. Due to the highly linear calibration curves of the gage, as well as the amount of significant digits which the data reduction was performed with, the uncertainty due to the data reduction is minimal around ± 0.5%. A summary of the uncertainty analysis can be found in Table 3 in which the overall error was computed using the root-sum-squares method.

Table 3: Measurement Uncertainties

Type of Uncertainty	**Level of Uncertainty**
Calibration	
Forward Rotation	± 2.0 %
Axial Rotation	± 1.5 %
Temperature drift during calib.	Negligible
Data Acquisition	
Zero Drift -electronic noise from computers sensors, wires, and connections	± 2.5 %
Gap ratio, Lip Ratio Errors	± 1.5 %
Protrusion Errors	± 0.5 %
Temperature Drift during Testing	± 1.0 %
Vibration Errors, 2 g_{rms}/ 8 g_{rms}	±5.98 % / ± 24.0 %
Data Reduction	
Truncation, Curve fits	± 0.5%
Overall Uncertainty, 2 g_{rms}/ 8 g_{rms}	**±7.21% / 24.3% of full scale output**

Chapter 4. Test Facilities

4.1. Vibration Test

The vibration testing for this study was performed at the Virginia Tech Modal Analysis Lab. The analyses that were performed involved the experimental determination of the natural frequencies and modes of the skin friction gages, as well as the simulation of the operation of the skin friction gages under the two vibration environments anticipated during the flight test.

The experimental setup involved the block-diagram shown in Figure 10 of Chapter 2.2. A photograph of the experimental setup can be seen in Figure 21.

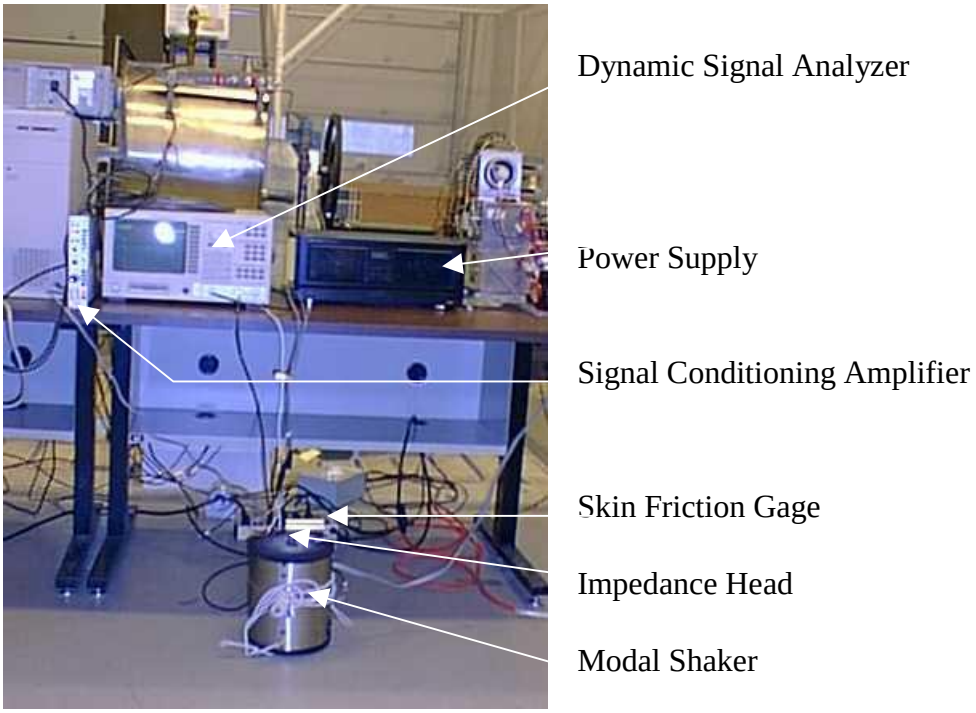

Figure 21: Photograph of Experimental Vibration Test Setup

The main equipment used during these tests involved a modal shaker from the Vibration Test Systems Corporation, which simulated the random noise vibration. The shaker is an electrodynamic vibration generator designed for laboratory and general industrial use. It stands 11.5 in. high and 10.25 inches in diameter. The experiment also utilizes a

Hewlett Packard 35665A Dynamic Signal Analyzer, which served as both the random signal generator as well as a signal analyzer and recorder. The tests utilized an Onkyo Integra stereo power amplifier as a means of supplying power to the experiment. A PCB 288D01 impedance head was used as an accelerometer and force transducer. During the vibration simulation tests, the voltage output from the strain gages was modified through a 2310 Signal Conditioning Amplifier manufactured by the Measurements Group Instrument Division. For signal processing purposes the output was amplified 100 times and filtered.

4.2. Electromagnetic Test

The electromagnetic tests utilized a Walker Scientific Inc. MG-5DAR gaussmeter to measure the actual flux density created between the poles of the electromagnet, and verify the estimated theoretical values. The gaussmeter had a range of 100 mG to 150 kG with a resolution of 0.05%. The Hall effect gaussmeter utilized a small Hall probe that could be inserted inside the electromagnet, so that the flux density profiles could be ascertained. The probes have an accuracy of ± 1.0% of a full-scale reading. These probes measure the magnetic fields perpendicular to the axis of the probe. A picture of the probe can be found in Figure 22.

Figure 22: Walker Scientific Gaussmeter

4.3. Supersonic Wind Tunnel

The wind tunnel verification tests were performed in the Virginia Tech 9 x 9 inch (23 X 23 cm) supersonic/transonic wind tunnel. This wind tunnel was designed and originally constructed at the NASA Langley Research Center. The tunnel has been in operation at Virginia Tech since 1963. Schematics of the tunnel can be found in Figure 23.

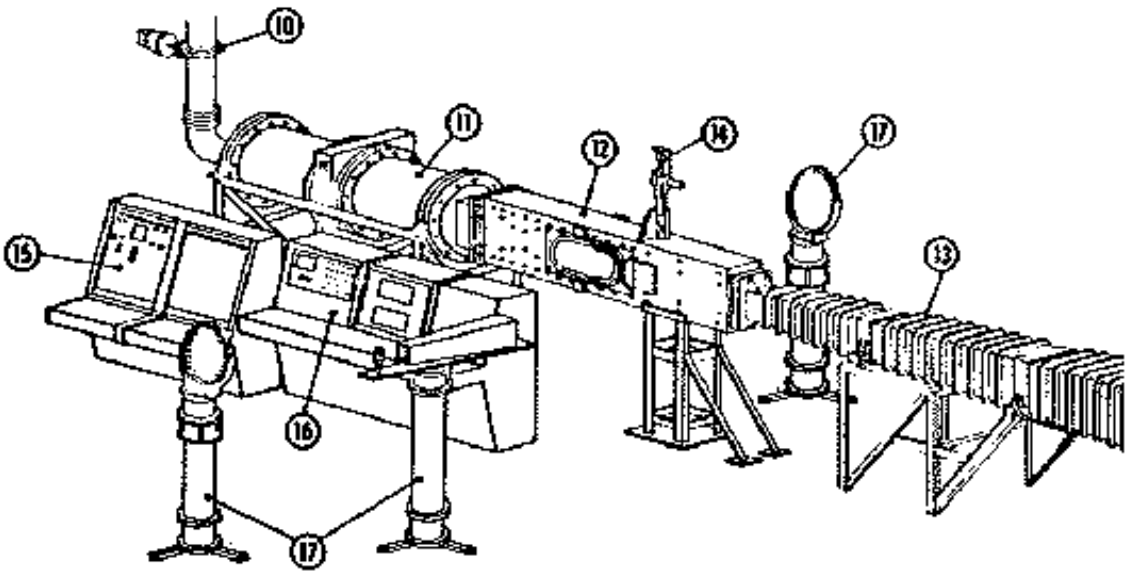

Figure 23: Virginia Tech Supersonic Windtunnel

10)-Pressure Regulator,

11)-Settling Chamber,

12)-Test Section,

13)-Diffuser,

14)-Model Support and Drive System,

15)-Tunnel Control Panel,

16)-Measurement Panel,

17)-Schlieren Apparatus

It has had a variety of modifications introduced into the air pumping, tunnel control, and instrumentation in attempts to keep the tunnel current and increase its capabilities. These specifications and more can be found on the supersonic tunnel web sight at http://www.aoe.vt.edu/aoe/physical/superson.html. The air pumping system consists of an Ingersoll-Rand Type 4-HHE-4 4-stage reciprocating air compressor driven by a 500 hp, 480V Marathon Electric Co. motor. The compressor can pump the storage system up to 51 atm. A drying and filtering system is provided which includes both drying by cooling and drying by absorption. The air storage system consists of two tanks with a total volume of 23 m^3. The tunnel control system includes a quick opening butterfly valve and a hydraulically actuated pressure regulating 12 in. (30.5 cm) diameter valve. The settling chamber contains a

perforated transition cone, several damping screens, and probes measuring stagnation pressure and temperature. The nozzle chamber is interchangeable with two-dimensional contoured nozzle blocks made of steel. The tunnel is equipped with three complete nozzle chambers, which presently are fitted with the nozzles for the Mach numbers 2.4, 3.0, and 4.0. The working section of the tunnel is equipped with a remotely controlled model support, which allows one to vary the position of a model in the vertical plane. An arrangement for a sidewall model mounting is also available. An extractable mechanism can be provided for supporting the model during the starting and stopping of the flow. Due to large doors containing the windows in the nozzle and working sections, a very good access to the model is ensured. After passing through a diffuser the airflow is discharged into the atmosphere through a muffler located outside of the building. Table 4 lists the tunnel specifications.

Table 4: Technical Specification of the Wind Tunnel

Test section size	23 x 23 cm
Stagnation pressure	3 - 20.5 atm
Mach number	2.4 - 4 and 0.2 - 0.8
Reynolds number per meter	2×10^6 to 5×10^6
Run duration, depending on Mach number and stagnation pressure	8 - 60 sec
Dewpoint	Below -40C
Maximum model diameter at M=3	9 cm
Storage tank volume	23 m^3
Maximum air pressure in the storage tanks	51 atm
Total power rate of the compressor plant	500 hp

For the actual wind tunnel verification tests performed in this study, the tunnel was run with a Mach 2.4 nozzle at low stagnation pressures ranging between 55 and 75 psi. These conditions produced shear levels on the order of τ_w=3.9 to 5.3 psf. Three skin friction gages were tested simultaneously during the wind tunnel verification portion of this study. The arrangement can be found in Figure 24. The largest gage discussed in this study (Chapter 7: Prototype 3) was the electromagnetic eddy current damped skin friction gage.

The remaining two skin friction gages were a shock tunnel gage, and a fiber-optic skin friction gage, neither of which are discussed in this study.

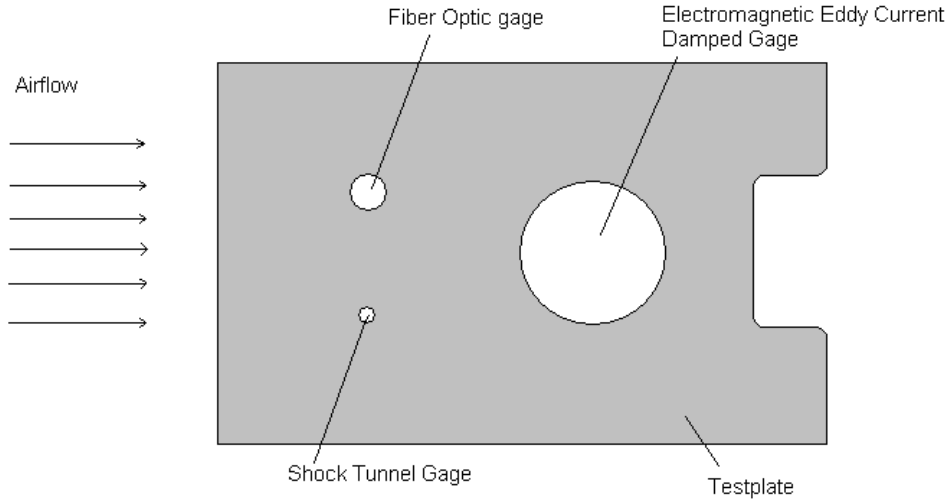

Figure 24: Supersonic Wind Tunnel Test Plate Arrangement

Chapter 5. Prototype 1 – Small Air Volume Damper Configuration

5.1. Objectives and Rationale for Design

The first prototype that was designed to investigate the NASA vibration test requirements utilized no oil damping whatsoever. In this manner, the gage would avoid the oil leakage and the maintenance problems associated with oil fill.

It was designed in hopes that small air gaps within the interior of the gage would provide adequate enough damping to survive the rigorous vibration environment which NASA expected, and be capable of producing accurate skin friction measurements. The gage possessed small 0.002 inch gaps underneath the floating sensor head which made it more difficult for air to flow in and out of the gage, as well as provide potential damping from vibrations. To this point, vibration testing had not been tested to this rigorous level, so the effects of this environment were unknown.

5.2. Design configuration Description

The gage was modeled closely after previous Virginia Tech designs [25]. It followed the same non-nulling, direct measurement technique with a Kistler-Morse DSC-6 unit as designs of previous years, yet it lacked any oil filling. Thus, if the gage performed adequately in the vibration simulation, little if any changes would need to be implemented into future designs which would also need to perform under similar rigorous test conditions.

The head was sized according to the anticipated 0.3 to 1.5 psf shear for the NASA flight test, and the length was determined to provide the desired level of accuracy. This gage was the smallest of the three prototypes researched in this study. The length from the top of the head to the back of the strain gage unit was 2.5 in. long. The head diameter was 0.9295 in., and 0.125 in. thick. The shaft was 0.25 in. thick to accommodate the diameter of the Kistler-Morse beam. The gage was assembled with a minimum number of parts in an attempt to minimize the complications encountered during the assembly phase of the gage. A CAD drawing of the gage can be found in Figure 25. A new two piece housing assembly was used

so that the gap found underneath the head could be accurately positioned. The 0.002 in. gap was measured with feeler gages to provide an accurate position for the head. After that piece was assembled, the outer housing was added and placed in a position such that the head and housing were flush with one another. In addition, the lower section of the outer housing was threaded, so that a nut could be used to secure the gage into position in the test plate

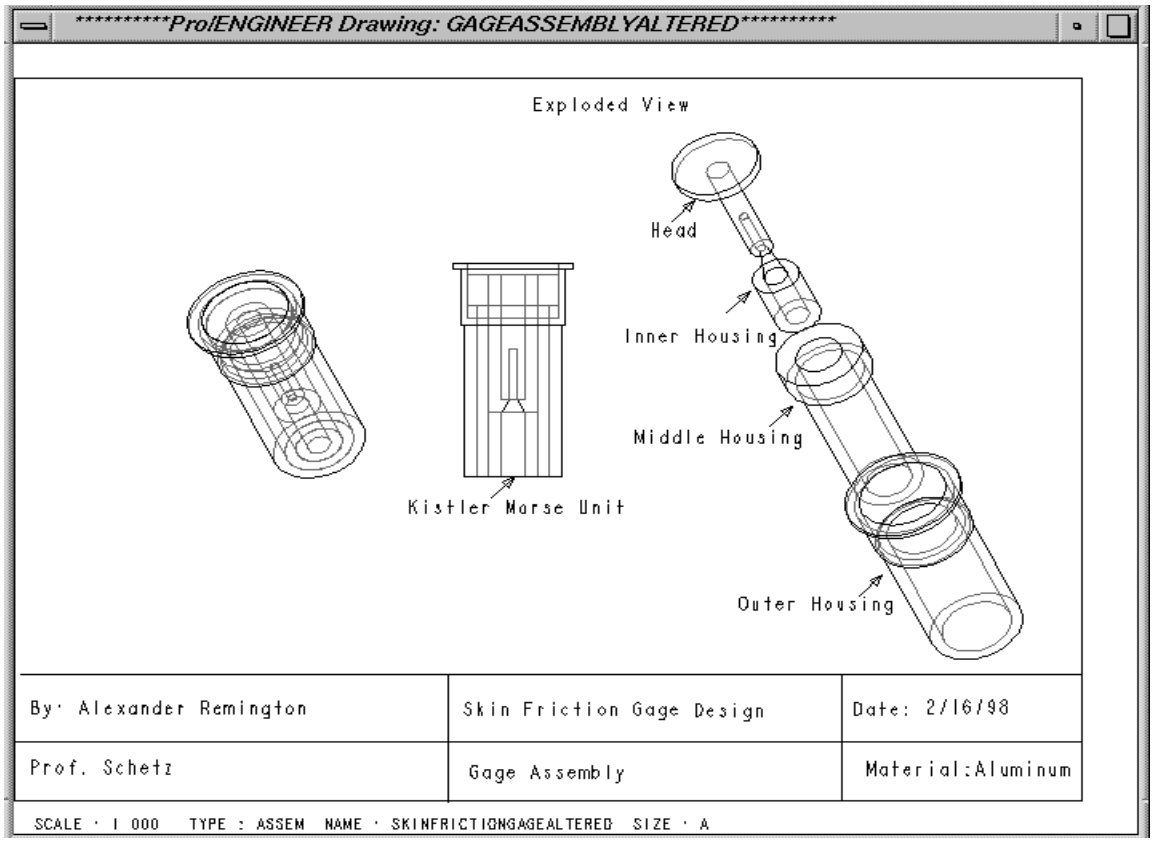

Figure 25: First Prototype Drawings

5.3. Prototype 1 Results

5.3.1. Experiment 1: Natural Frequency Measurement

The first experiment for the vibration analysis was the measurement of the natural frequency of the first skin friction gage prototype. This was done by physically vibrating the system on a VTS Modal Shaker in a uni-axial direction with a random noise input at a level of 25 mV_{pk} (2.5 g_{rms}). The force transducer and accelerometer were wired to the Hewlett Packard 35665A Dynamic Signal Analyzer which measured the frequency response of the

vibrating system along with the phase and coherence of the vibration over a range of 0 to 3200 Hz. This was the smallest range available to the Signal Analyzer which encompassed the 0 to 2000 Hz range specified by NASA. This frequency response analysis gave satisfactory results. The following graph has a logarithmic scale on the y-axis for easier analysis.

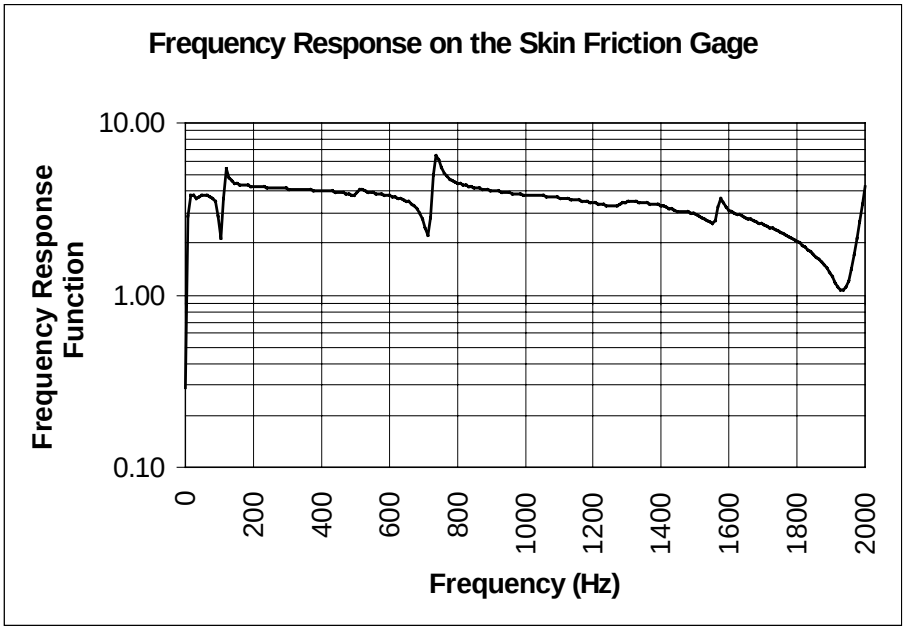

Figure 26: Prototype 1 Frequency Response of the Skin Friction Gage

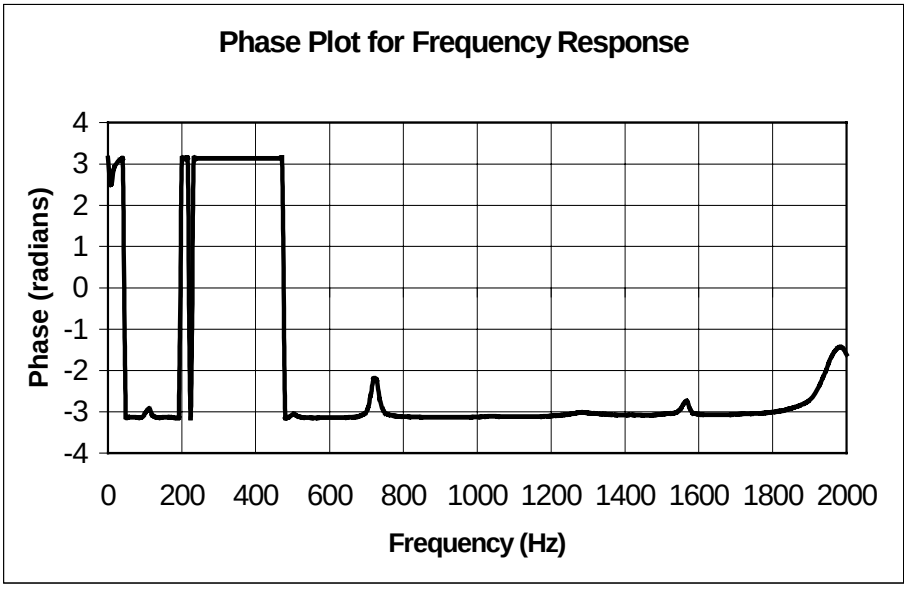

Figure 27: Prototype 1 Phase of Frequency Response Function

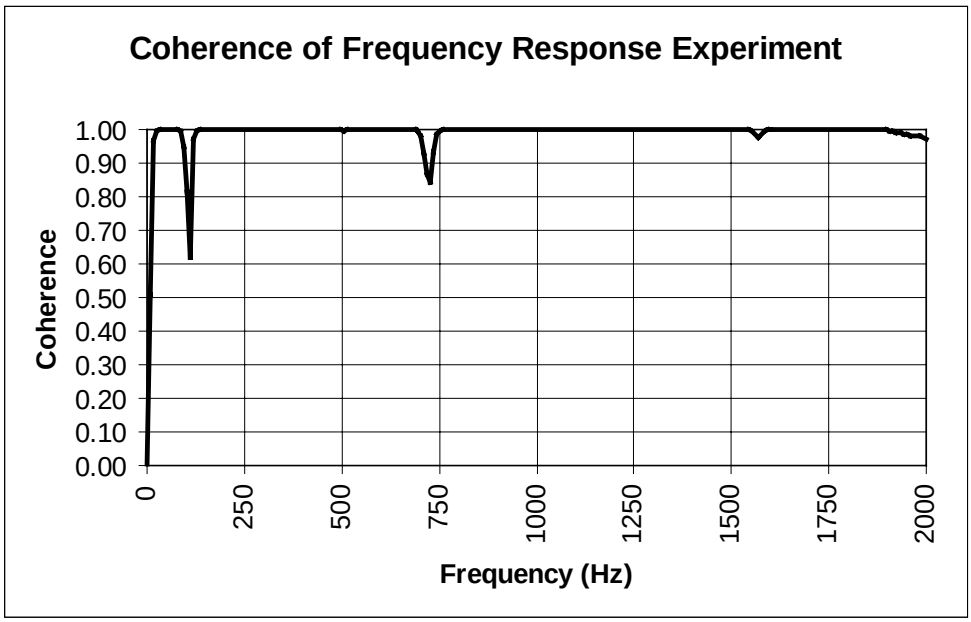

Figure 28: Prototype 1 Coherence of Frequency Response Function

The plots of frequency response function, phase, and coherence shown above in Figure 26, Figure 27, and Figure 28 were used to find the vibration characteristics of the gage. The frequency response and the phase were used to find the natural frequencies of the gage. The coherence of the vibration was nearly 1.0 over the entire frequency domain with the exception of the natural frequencies. This showed low noise in the measured signal. The frequency response measured four natural frequencies within the 2000 Hz range shown in Table 5.

Theoretical results for the frequency response of the system were calculated using the BEAM6 vibration program [43]. The program used estimated damping coefficients as well as the geometry and material properties of the first skin friction gage prototype from Figure 25 as inputs for the theoretical model. Minimal damping was provided by both the air surrounding the beam and the inherent material damping of the beam itself. The material damping values were found from material property tables. Beam6 was then used to calculate the natural frequency of the modeled system. The results of the system are shown in the following Table 5.

Table 5: Comparison of Prototype 1 Theoretically Calculated and Experimental Measured Natural Frequency Modes

f_n Number	**Measured Natural Frequency, f_n (Hz)**	**Theoretical Natural Frequency, f_n (Hz)**
1	110.2	159.2
2	728.1	2294.4
3	1568.0	-
4	1998.7	-

The theoretical calculations only predicted two bending modes at 159.2 Hz, and 2294.4 Hz. These two modes coincide with the first and fourth modes measured experimentally 110.2 Hz and 1998.7 Hz, respectively. The discrepancy in the number of modes could be attributed to a number of reasons. From this experiment, the first and fourth experimentally measured natural frequency modes were due to the first and second bending modes of cantilever beam inside the gage. The second and third modes may have been a result of torsional bending of the cantilever beam or the natural frequencies of the housing and nut system containing the cantilever beam. If the system did have torsional bending or some housing natural frequencies, then those would not be calculated from BEAM6 code.

The discrepancy in the values of the two sets of natural frequencies may be attributed to inaccurate estimates of the material properties of certain sections. Another potential inaccuracy of the model was in the cantilevered base assumption. A real system may actually flex slightly at the secured base of the gage causing a discrepancy between the theoretical and experimental models. Consequently, the theoretical calculations for the beam were made with a slightly stiffer beam than the actual beam. Thus, the theoretical calculations were slightly higher, because the natural frequency is related to $\sqrt{k}$ for the general case of a cantilevered beam. Also, the BEAM6 program was unable to analyze visco-elastic materials. Thus, the silicone rubber casing surrounding the base of the Kistler-Morse unit may not have been modeled accurately, and that may be a source of error.

5.3.2. Experiment 2: Simulation of NASA Random Vibration Test Curve A

The second experiment for the vibration analysis of the first skin friction gage prototype involved the simulation of a Random Vibration Test Curve provided by NASA in their vibration specification manual [36]. All devices which will be used on the FTF-II plate need to pass test specifications for use during flight experiments. The skin friction gage will be subject to Category II test requirements (turbojet powered aircraft tests). For acceptance on to the FTF-II the skin friction gage must be tested under representative FTF-II conditions. Vibration tests on all hardware would be performed using a random vibration test curve equivalent to the 8.0 g_{rms} to a maximum of 2000 Hz. NASA specified these conditions for operation in the flight test fixture as Curve A shown in Chapter 1.3.2. Figure 5.

This experiment followed the setup discussed in Figure 10 of Chapter 2.2 and of Figure 21 of Chapter 4.1. The experiment was set up with an 8 g_{rms} random noise vibration from the VTS modal shaker. The strain gages from the skin friction gage were than hooked up to a 2310 Signal Conditioning Amplifier that was then linked to the Hewlett Packard 35665A Dynamic Signal Analyzer so that the response of the gage from the random vibration test curve could be analyzed.

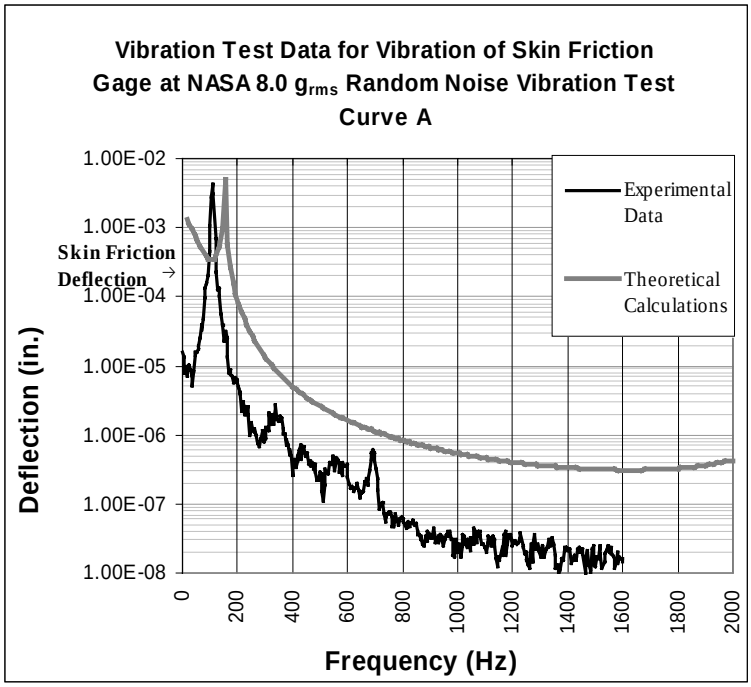

Figure 29: Comparison of Prototype 1 Gage Experimental and Theoretical Results of Head Deflection

First, a comparison was made between the experimental values measured from the NASA Vibration Test Requirement Curve A and the theoretical analysis which used the BEAM6 program. The comparison of the beam deflections over the frequency spectrum is shown in Figure 29. It is apparent that the results differed somewhat. This discrepancy could be attributed to the inability of the BEAM6 program to model visco-elastic damping. The Kistler-Morse Deflection Sensor Cartridge has a ring of silicone rubber surrounding the base of the unit which contributes additional damping to the system. The BEAM6 program is only capable of modeling viscous damping terms. Thus, the theoretical results are under-damped. The discrepancy in the natural frequencies is a result of the stiffness inaccuracies in the model discussed previously.

Figure 30 shows the same experimental data from Figure 29 except that the strain gage output has been non-dimensionalized with the anticipated strain gage output from skin friction during flight testing.

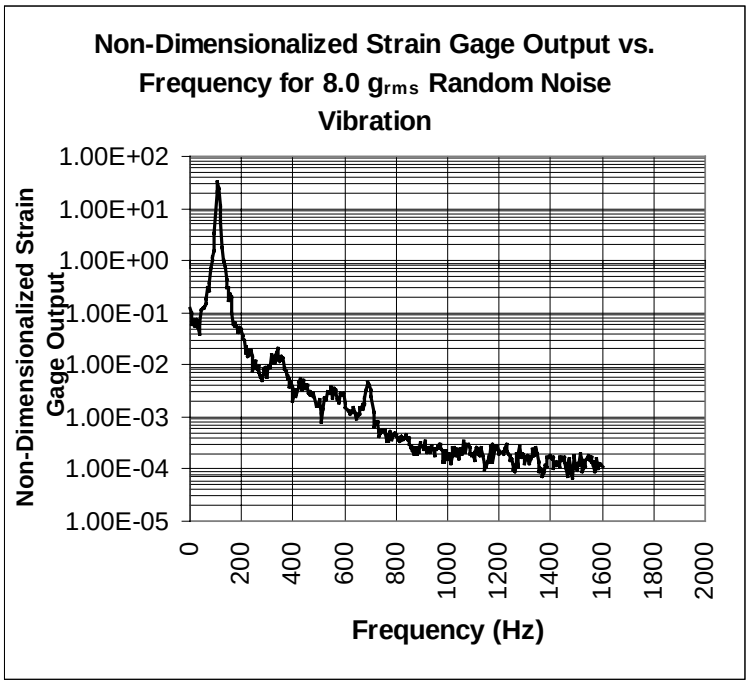

Figure 30: Non-Dimensionalized Deflection of Skin Friction Gage Head vs. Frequency for Curve A

This non-dimensionalized quantity represents the ratio of vibration induced noise to desired output. If the ratio is equivalent to 1.0, then the output due to vibration is equivalent to the output due solely to skin friction of the flow over the floating head. It is clear from this

graph that the largest vibration effects can be attributed to the first mode, 110.2 Hz, natural frequency. The deflections due to vibration at the natural frequency were more than 30 times that of the deflections due only to skin friction. It was apparent from this that the noise due to vibrations at the natural frequency produced an output that made the measurement of skin friction impossible. The effects of the vibration at other frequencies appeared to be trivial. A small peak can be seen at 728 Hz. This corresponds well with the second mode from the experimental frequency response analysis. It produces a peak significantly less than the first mode, yet it still would produce noise levels on the order of 4.0 % of the desired output. Beyond the effects of the 110.2 Hz, and 728 Hz natural frequency, the noise caused by the vibratory environment dropped below 1 % of the output measured from only skin friction.

During testing, it became apparent that the head was making contact with the outer housing at the first mode natural frequency. During an 8 g_{rms} random noise vibration, the gage produced a clicking noise which upon closer visual inspection revealed that the head was experiencing deflections equivalent to the gap width in which it was free to move. Next, a time history at the first bending mode was performed in an attempt to gain a greater understanding of what was occurring. The system was then vibrated with an input sine wave at 8.0 g_{rms} and the following data was obtained.

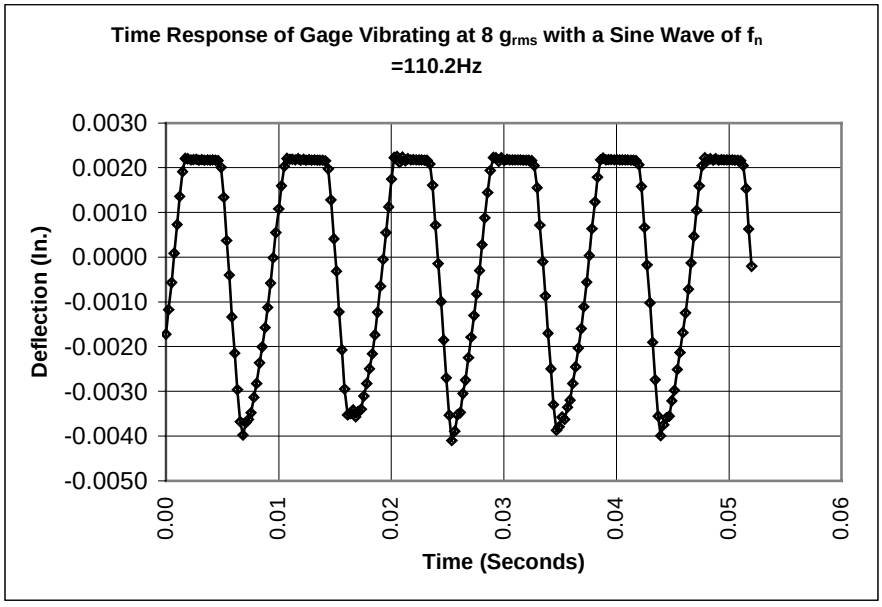

Figure 31: Time Response of Skin Friction Gage Vibrating at Natural Frequency at 8 g_{rms}

Figure 31 shows that when the skin friction gage was excited at 110.2 Hz, the head deflected well beyond the 1.32×10^{-4} in. expected from just skin friction. Positive deflections entail movement above the centered neutral position of the floating head, and negative deflections were movements below the neutral position of the floating head. It can be seen from Figure 31 that when the gage vibrated at its first mode natural frequency, the gage struck the side of the housing on the positive deflections. This can be inferred from the chopped amplitude of the sine curve at 0.0022 inches. However, the sine wave did not hit the housing on the negative deflections. Curiously, when the head struck the housing the deflections were smaller than the gap distance of 0.005 in. This discrepancy was due to the fact that the head was not centered perfectly during assembly. The head was shifted above the neutral position approximately 0.003 inches. Nonetheless, the head did strike the housing during the experiment which was an unacceptable vibration characteristic.

5.3.3. Experiment 3: Smooth Flight Vibration Simulation

It was anticipated that the gage might actually experience a smoother flight than the rigorous Curve A vibration level that NASA required. The third experiment of the vibration analysis of the skin friction gage involved the simulation of a random vibration test curve similar to the Curve A used in the second experiment. The only difference was that the gage was shaken at 2.0 g_{rms} instead of 8 g_{rms}. This smaller acceleration loading was a more accurate simulation of the vibrations that the FTF-II plate would undergo during a typical smooth flight. Figure 32 plots the deflections of the gage head for the required frequency spectrum. A plot of the strain gage output non-dimensionalized with the anticipated strain gage output produced solely from skin friction is shown in Figure 33.

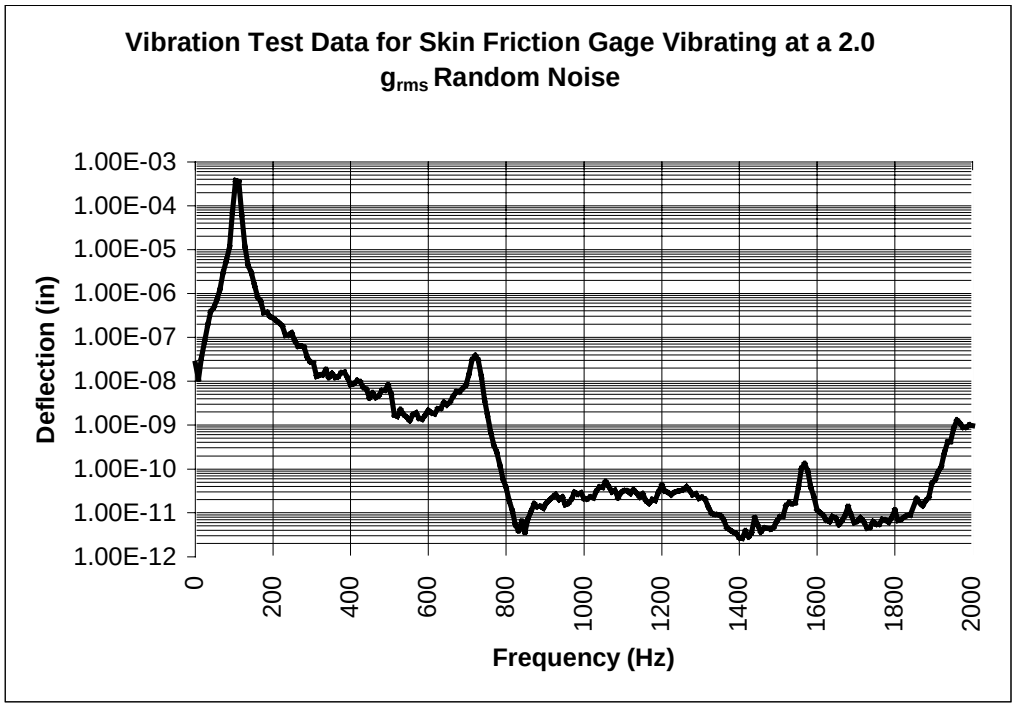

Figure 32: Deflection of Prototype 1 Gage Head for Smooth Flight

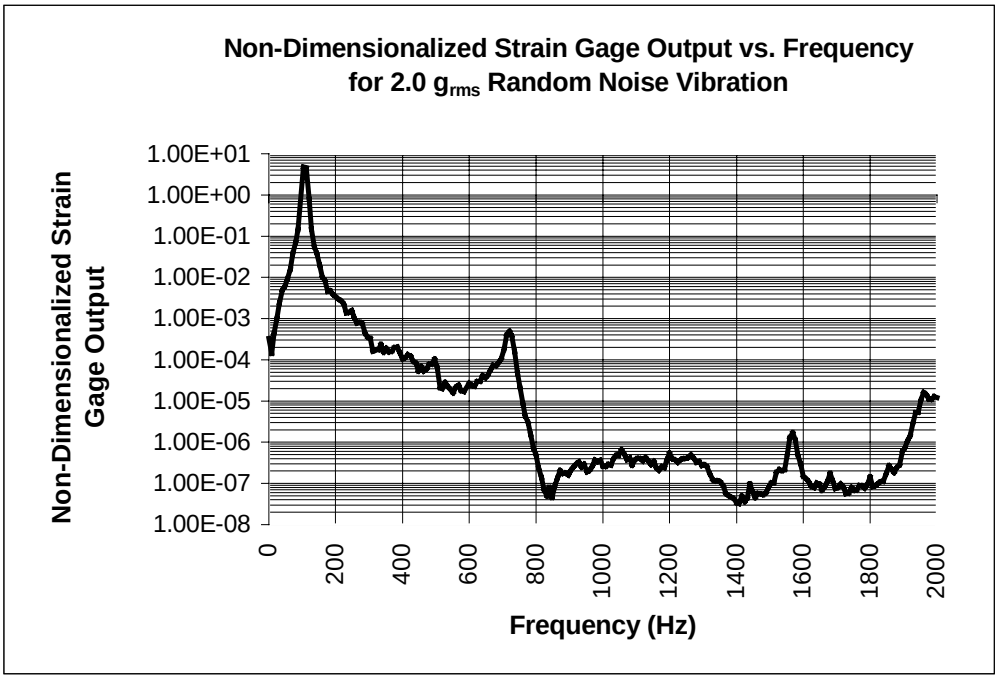

Figure 33: Non-Dimensionalized Strain Gage Output of Prototype 1 Gage for Smooth Flight

These graphs showed that even at lower acceleration loads of 2.0 g_{rms} the gage exhibited poor vibration characteristics. It was visible from Figure 32 and Figure 33 that the vibration effects due to the 110.2 Hz natural frequency were excessive. In a similar, yet less extreme manner than the 8.0 g_{rms} case, the noise due to 2.0 g_{rms} vibrations at the first mode natural frequency produced an output that would make the measurement of skin friction highly inaccurate. The deflections due to vibration at the natural frequency were still 5 times that of the deflections due only to skin friction. The effects of the vibration at other frequencies appeared to be trivial again, yet a second mode at 728 Hz produced a more distinct peak than in the 8.0 g_{rms} vibration. Beyond the effects of the 110.2 Hz natural frequency, the noise caused by vibration drops well below 1 % of the anticipated skin friction output. In this 2.0 g_{rms} experiment, the 1568 Hz third mode discovered in the frequency response analysis, became more distinct. Yet, both the 728 Hz, and 1568 Hz modes produced small enough amplitudes that they were inconsequential in the vibration analysis. The primary concern from this analysis were the effects of the first bending mode.

5.4. Prototype 1 Conclusions

It can be deduced from this experiment that vibration characteristics of this skin friction gage were poor for its intended use on the F-15 mounted FTF-II plate. From these experiments, it became apparent that a method of strongly damping these gages was critical. This first prototype gage would not give accurate results of skin friction when the gage vibrated near its natural frequency. Noise, which produced five to thirty times the expected skin friction output value, created experimental output of very little value. Both the 8 g_{rms} and the 2 g_{rms} environments produced poor vibration characteristics in the skin friction gage. So, this gage had to be redesigned in a manner that would decrease or eradicate the vibration effects at the natural frequency. This can be done in two ways. First, the system can be damped which would decrease the amplitude at the natural frequency and, consequently, decrease the effects on the output of a vibrating system. This can be performed by any of the seven methods discussed in Chapter 1.3.1. The second method of altering the performance of the gage is to resize the structure so that the natural frequency is forced above or below the experimental frequency range. Attempts to do this had been made in the past, yet were unsuccessful.

A variety of other changes need to be implemented in the first prototype of the skin friction gage. Another major issue unveiled during this experiment was the fragility of the electronics on the gage. During testing the vibrations caused the lead wires from the strain gage and the thermocouple to sever, as well as causing the floating head to become damaged. Thus, a wire guard must be placed at the bottom of the gage to inhibit the movement of the brittle Kistler-Morse Gage voltage output wires. In attempts to decrease the influence of the vibration on the performance of the gage, the neck weight and head weight must be decreased. Also, it is critical that the deflections of future prototypes remain within the housing-head gap width of 0.005 in. so that the survivability of the gage is increased.

Chapter 6. Prototype 2 - Permanent Magnet Eddy Current Damper Configuration

6.1. Objectives and Rationale for Design

The second prototype that was designed for this study attempted to improve upon the first configuration. These improvements were implemented by changing four aspects of the first prototype gage. Most importantly, an eddy current damper was incorporated into the design in an attempt to reduce the influence of vibration on the sensing head. The eddy current damper would replace the oil filled damping methods of previous Virginia Tech gages. This would hopefully provide a system that resolved all of the oil leakage and maintenance issues of previous gages yet still achieve significant damping. Second, NASA specified that the new design needed to have three times the sensitivity of the first prototype. Consequently, the size of the gage was changed accordingly. The head needed to be increased to a diameter of 1.5 in., and the length of the cantilevered beam needed to be increased as well. Thus, the length of the gage from the top surface of the head to the back surface of the Kistler-Morse gage increased to 3.25 in. Third, decreasing the mass of the head and cantilevered beam would diminish the effects of the vibration on the gage. So, the mass of the head and beam were decreased by making the head and shaft thinner. Fourth, careful analysis needed to be performed throughout the design to ensure that the gage head would not strike the housing during testing, thus increasing both the survivability of the gage and the quality of the skin friction results.

6.2. Design Configuration Description

In order to size the gage correctly, a variety of trade studies were performed, to see which combination of length and head diameter would produce a gage with the appropriate characteristics. Figure 34 and Figure 35 show trade studies illustrating the effects of shaft length and head diameter on accuracy and weight. The sensitivity of the first gage was quantified by calculating the force that the end of the Kistler-Morse DSC unit senses from the test condition shear forces (τ_w=0.3 - 1.4 psf). This force, F^*, had a value of .0028 lb_f for

τ_w=0.3 psf. This can then be used as a basis for the sensitivity. The sensitivity needed to be tripled, so the end of the DSC unit needed to sense an F^*=.084 lb_f. A goal was set at getting the sensitivity to within 10 % of the request from NASA.

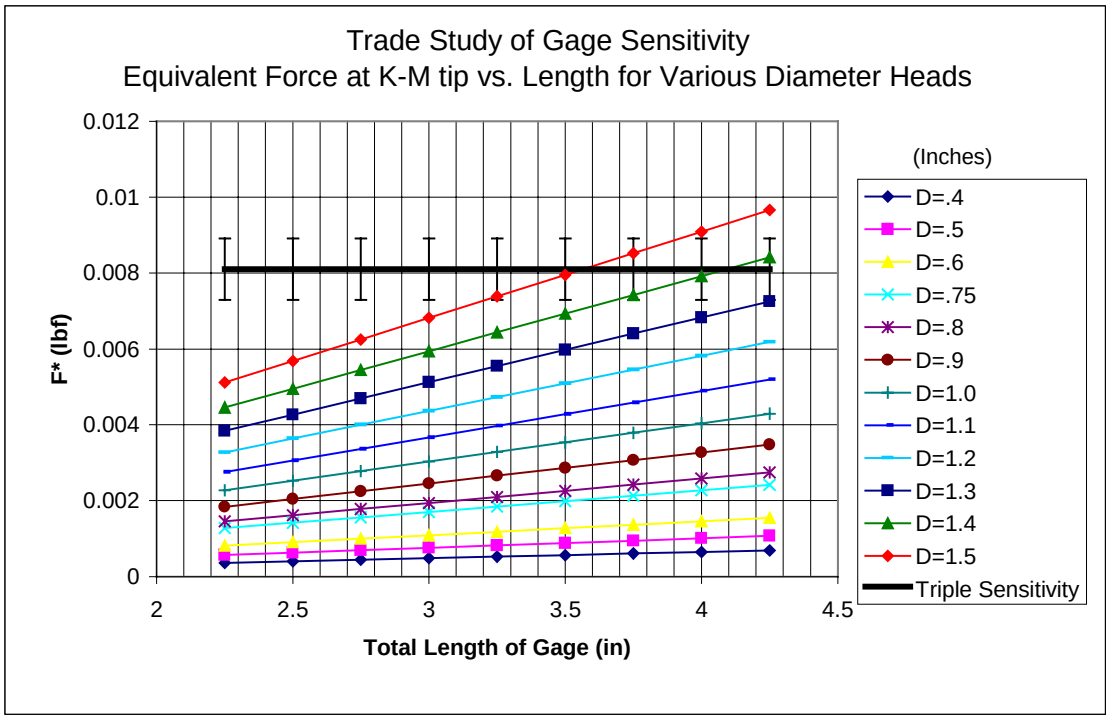

Figure 34: Sensitivity Study for Gage Resizing

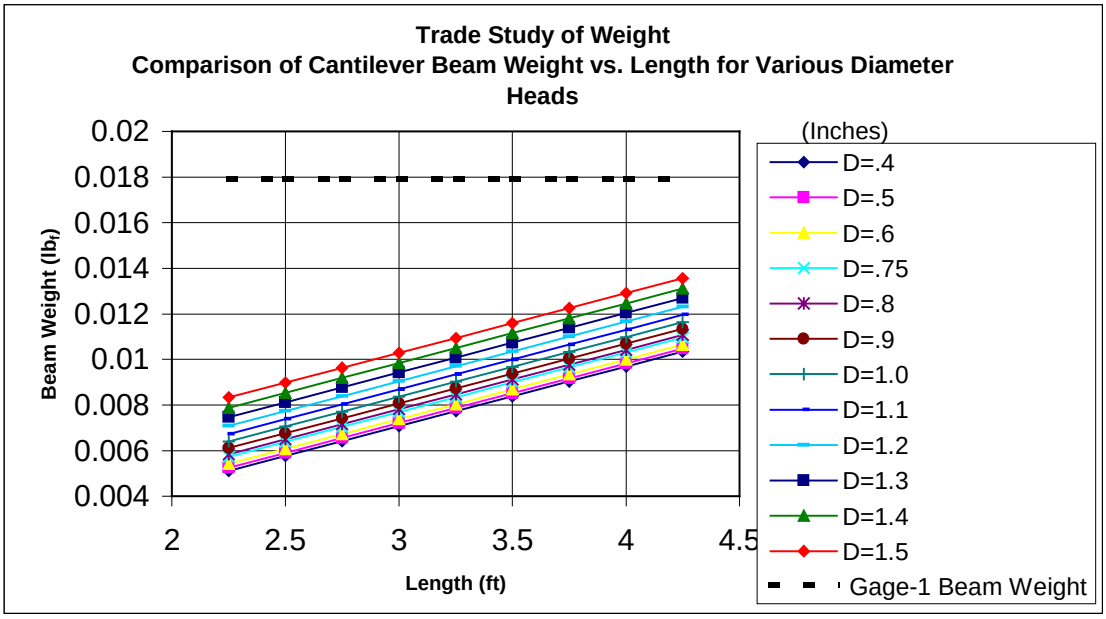

Figure 35: Weight Study for Gage Resizing

It was apparent that increasing sensitivity by increasing the gage dimensions would inevitably increase the gage sensitivity to vibration. So a head diameter of 1.5 in. and a length of 3.25 in. was chosen which meets the lower end of the goal. The weight analysis in Figure 35 showed that all of the new configurations were well under the weight of the first prototype. This can be attributed to the thinner head and shaft. The head thickness was reduced to 0.0625 in., and the shaft diameter was reduced to 0.020 in. So the new diameter and length were deemed acceptable under that parameter. It was also calculated that under the load of anticipated test condition shear forces, the head would not touch the housing.

Next, a method of implementing the eddy current optimization configuration from Figure 13 within the parameters of this design was required. Further sizing of the magnets and conductor within the gage housing were performed using the parameter established by Mikulisnksy and Shtrikman [58] with Equation 26, Equation 27, and Equation 28. The end result was the skin friction gage of Figure 36 with the internal schematics shown in Figure 37.

Figure 36: Photograph of Prototype 2 Skin Friction Gage

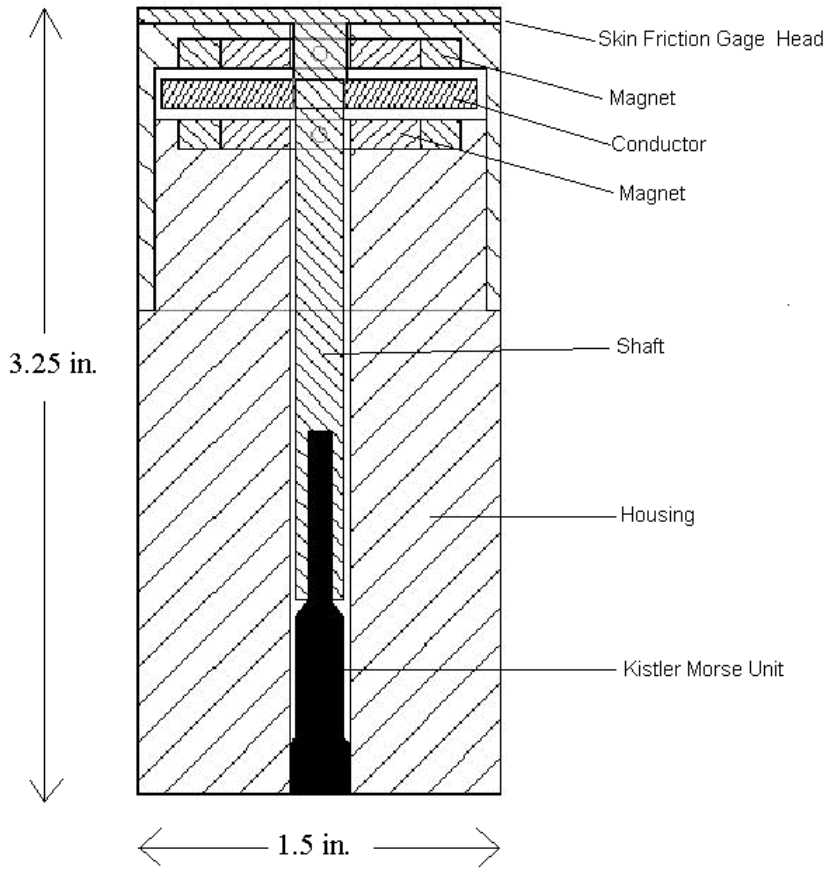

Figure 37: Prototype 2-Permanent Magnet Eddy Current Damped Skin Friction Gage

The conductor disk shown in Figure 37 was constructed from aluminum due to its small resistivity of $\rho_e=2.66x10^{-8}$ Ω-m and low density. Copper has a slightly smaller resistivity, yet its density is much larger. The theoretical results of the design with copper and aluminum were compared. Aluminum was deemed the superior material for this application. The conductor disk was located as close as possible to the head of the gage, so that the vibration resistive force induced by the eddy currents acted on the location with the largest amplitude. The eddy current damping is related to the velocity of the vibrating beam, and the greatest velocities occur at the area of maximum amplitude. This location is also advantageous, because it is important to keep the magnets as far away from the electronics as possible to minimize magnetic interference. Tests showed that at the desired location, the magnets provided no measurable interference. This was accomplished by varying the axial proximity of the magnets from the strain gages and observing the effects on the strain gage output. Interference occurred only when the magnets were directly next to the wires or strain gages. Interference also occurred when the magnets were positioned so that the flux lines

attracted the steel core of the Kistler-Morse unit. Fortunately, the eddy current damper location that provided the best damping coincided with the location of minimum magnetic interference.

The number of pieces in the design setup remained an important design consideration. Again, it was important to attempt to minimize the pieces. This gage was designed with a two part housing which made the assembly of the eddy current damper simpler. A sleeve adapter, not shown in Figure 36 or Figure 37, would be required for assembly onto the test plate of a wind tunnel or flight test application. An adapter was not required for vibration tests performed in this study. Figure 38 shows the assembly view of the skin friction gage.

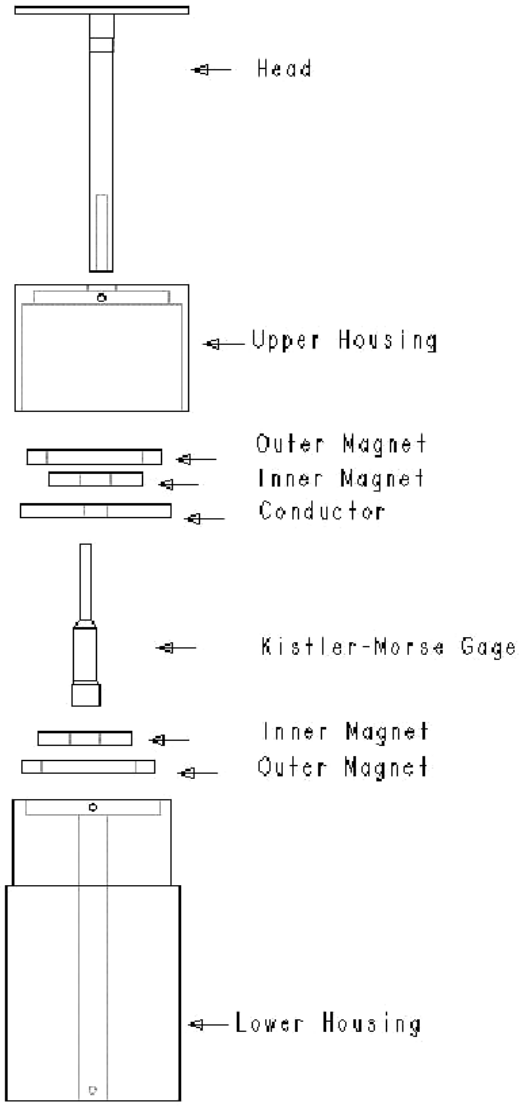

Figure 38: Exploded View of Prototype 2 Assembly

6.3. Magnetic Analysis

A magnetic analysis of the eddy current optimization technique was performed using a magnetic boundary analysis code called MAGNETO 3.1 provided by the Dexture Magnetics Company. This company offered to manufacture the magnets specified by second gage prototype and provide analytical support through their magnetic analysis program. The desired material was the one that provided the most magnetic flux density in the gap of eddy current optimized configuration. Alnico 5 produced the best theoretical results of all the available magnetic materials. Figure 39, Figure 40 and Figure 41 are graphic renderings of the model configuration, flux lines, and the level of the magnetic flux density in the gap.

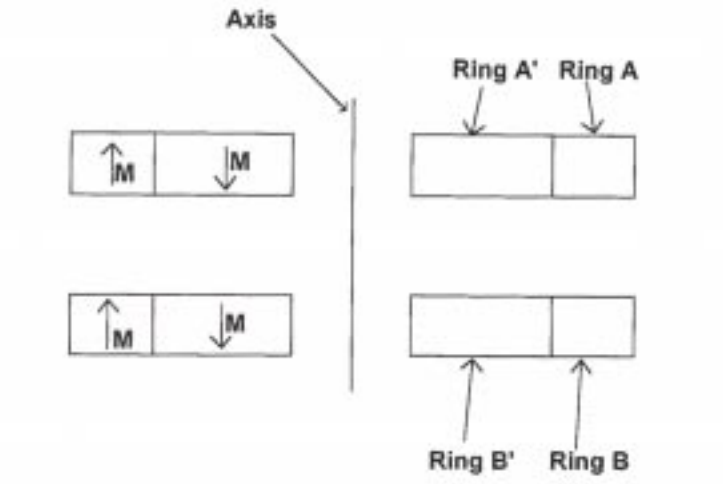

Figure 39: MAGNETO Model of optimized Configuration

Figure 39 is a representation of the optimized eddy current damped model used by the MAGNETO program. The model used the material properties of the Alnico 5 magnetic rings in addition to the geometry of the magnet to generate flux calculations.

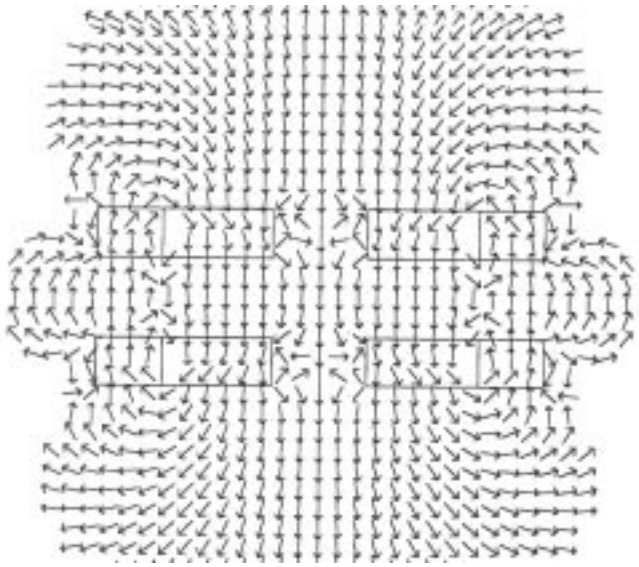

Figure 40: Theoretically Calculated Direction of Magnetic Flux Lines

Figure 40 shows the direction of flow of the magnetic flux lines. It is apparent from this figure that the flux lines flow in an intuitive manner in the direction of attraction from one polarity to the other. The magnitude of the magnetic flux density in the gap between the magnets is the primary quantity of interest from these theoretical analyses. This is plotted in Figure 41.

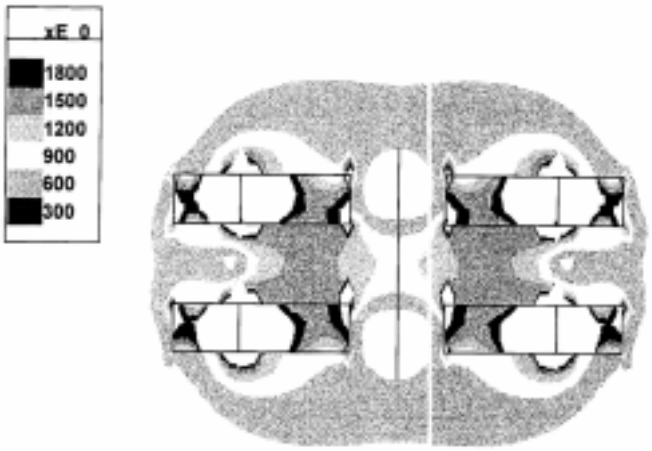

Figure 41: Optimized Eddy Current Damper Configuration Magnetic Flux Densities

From Figure 41 it can be deduced that the magnetic flux density in the gap ranges from 1200 Gauss to 1800 Gauss. A significant portion of the conductor disk will be in the 1500 Gauss region. The average value assumed to interact with the conductor disk during experiments was calculated to be 1500 Gauss.

6.4. Prototype 2 Results

6.4.1. Experiment 1: Natural Frequency Measurement

The first experiment of the vibration analysis was the measurement of the natural frequency of the skin friction gage. This was done in the same manner as the natural frequency measurement of Prototype 1. The gage was vibrated with a large VTS modal shaker in a uni-axial direction with a random noise input at a level of 25 mV_{pk} (2.5 g_{rms}). The gage was tested over a frequency range of 0 to 3200 Hz. This was the smallest range available to the signal analyzer which encompassed the 0 to 2000 Hz range specified by NASA. Figure 42 shows the frequency response analysis of the second prototype. The analysis provided satisfactory results. Figure 43 is a graph of the phase of the frequency response function, and Figure 44 is a plot of the coherence of that data.

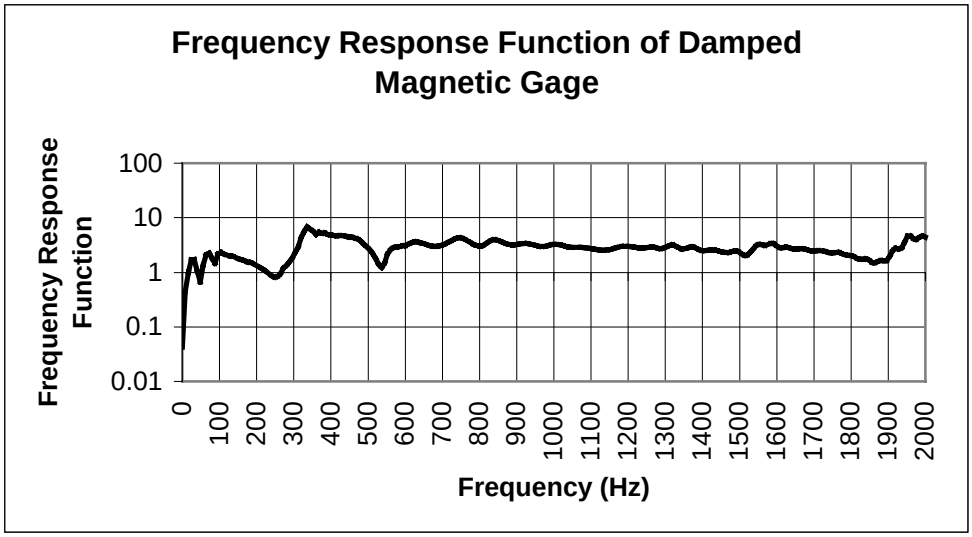

Figure 42: Prototype 2 Skin Friction Gage Frequency Response Function

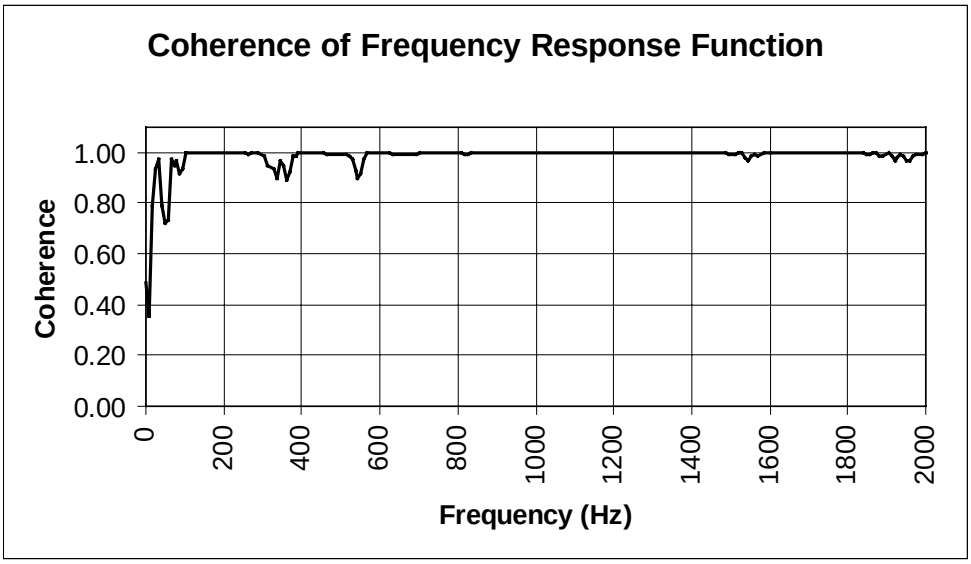

Figure 43: Prototype 2 Coherence of Frequency Response Function

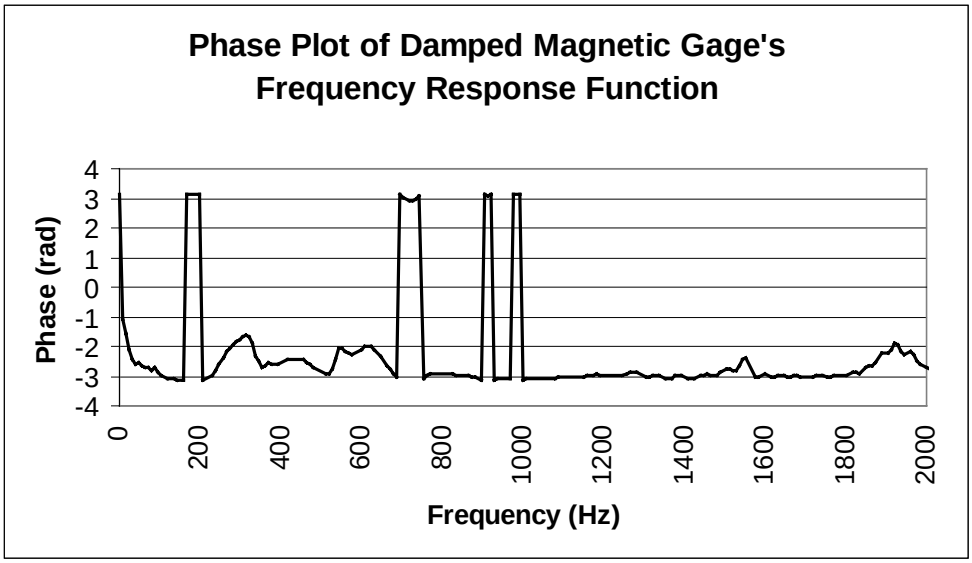

Figure 44: Prototype 2 Phase of Frequency Response Function

The coherence of the vibration was nearly 1.0 over the entire frequency domain with the exception of the natural frequencies. This showed excellent coherence. The frequency response function analysis measured four influential frequencies within the 2000 Hz range. These values were then compared with natural frequencies calculated from the BEAM6 theoretical model. This model utilized the geometry and material properties of the second gage prototype as well as the damping provided by the air surrounding the beam, the inherent material damping of the beam itself, and the estimated eddy current damping acting on the

conductor. The material damping values were found from material property tables, and the eddy current damping values were calculated from the analysis from the work of Mikulisnksy and Shtrikman [58]. The results of the two analyses are shown in Table 6 for comparison.

Table 6: Comparison of Prototype 2 Theoretically Calculated and Experimental Measured Natural Frequency Modes

f_n Number	**Measured Natural Frequency, f_n (Hz)**	**Theoretical Natural Frequency, f_n (Hz)**
1	48.0	73.6
2	310.2	765.7
3	550.2	
4	816.0	

The theoretical calculations only calculated two bending modes at 73.6Hz, and 765.7 Hz. These two modes coincide with the first and fourth modes measured experimentally at 73.6 Hz and 765.7 Hz, respectively. The discrepancy in the number of modes could be attributed to a number of reasons. From this experiment, the first and fourth experimentally measured natural frequency modes were due to the first and second bending modes of the cantilevered beam inside the gage. The second and third modes may have been a result of torsional bending of the cantilever beam or the natural frequencies of the housing and nut system containing the cantilever beam. If the system did have torsional bending or some housing natural frequencies, then those would not be calculated from BEAM6 code.

The discrepancy in the values of the two sets of natural frequencies may be attributed to inaccurate estimates of the material properties of certain sections. Another potential inaccuracy of the model was in the cantilevered base assumption. A real system may actually flex slightly at the secured base of the gage causing a discrepancy between the theoretical and experimental models. Consequently, the theoretical calculations for the beam were made with a slightly stiffer beam than the actual beam. Thus, the theoretical calculations were slightly higher because the natural frequency is related to $\sqrt{k}$ for the general case of a cantilevered beam. Also, the BEAM6 program was unable to analyze visco-elastic materials. Thus, the silicone rubber casing surrounding the base of the Kistler-Morse unit may not have been modeled accurately, and that may be a source of error.

6.4.2. Experiment 2: Simulation of NASA Random Vibration Test Curve A

The second experiment for the vibration analysis of the second skin friction gage prototype involved the simulation of a Random Vibration Test Curve provided by NASA in their vibration specification manual [36]. For acceptance on to the FTF-II the skin friction gage must be tested under representative FTF-II conditions. Vibration tests on all hardware were performed using NASA specified random vibration test curve A (Figure 5) equivalent to the 8.0 g_{rms} to a maximum of 2000 Hz. for operation in the flight test fixture.

This experiment followed the setup discussed in Figure 10 of Chapter 2.2 and of Figure 21 of Chapter 4.1. The experiment was set up with an 8 g_{rms} random noise vibration from the VTS modal shaker. The strain gages from the skin friction gage were than hooked up to a signal conditioning amplifier that was then linked to the dynamic signal analyzer so that the response of the gage from the random vibration test curve could be analyzed. Figure 45 shows the deflection of the damped gage head for the given frequency spectrum.

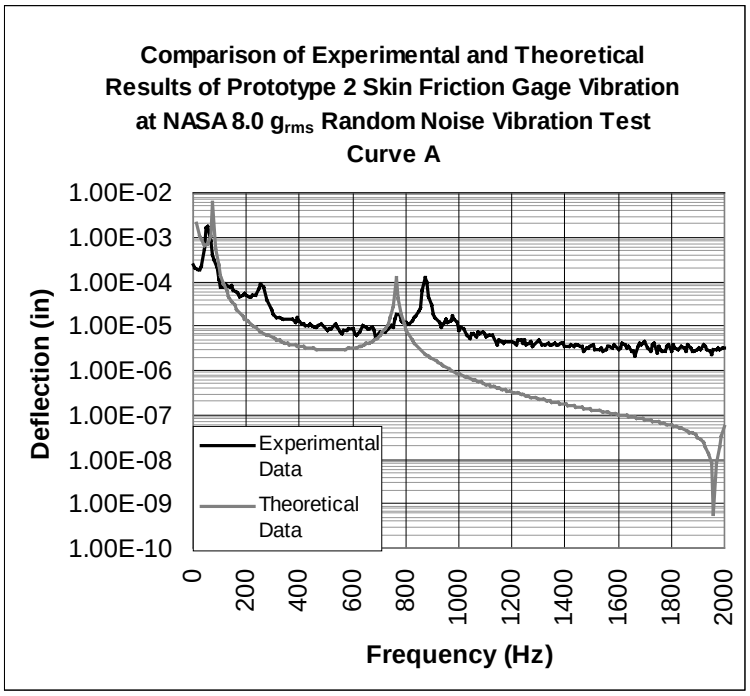

Figure 45: Comparison of Prototype 2 Experimental and Theoretical Results

First, a comparison was made between the experimental values measured from the NASA Vibration Test Requirement Curve A and the BEAM6 theoretical analysis. The comparison of the beam deflections over the frequency spectrum is shown in Figure 45. The general shape appears to be satisfactory, yet the theory predicted a first mode at a higher frequency and a larger amplitude. The magnitudes of the second mode were identical, yet theory predicted its influence at a lower frequency. The theoretical model also predicted a drop in the magnitude of the deflections as the frequency approached 2000, which the experimental analysis did not reflect.

The theoretical analysis also seems to have underestimated the damping provided at the first mode. It is apparent that the results differ slightly. This discrepancy can be attributed to the BEAM6 programs inability to model visco-elastic damping. As mentioned previously, the Kistler-Morse Deflection Sensor Cartridge has a ring of silicone rubber surrounding the base of the unit that would dampen the vibration of the system. The program is only capable of modeling viscous damping terms. Thus, the theoretical results are under-damped.

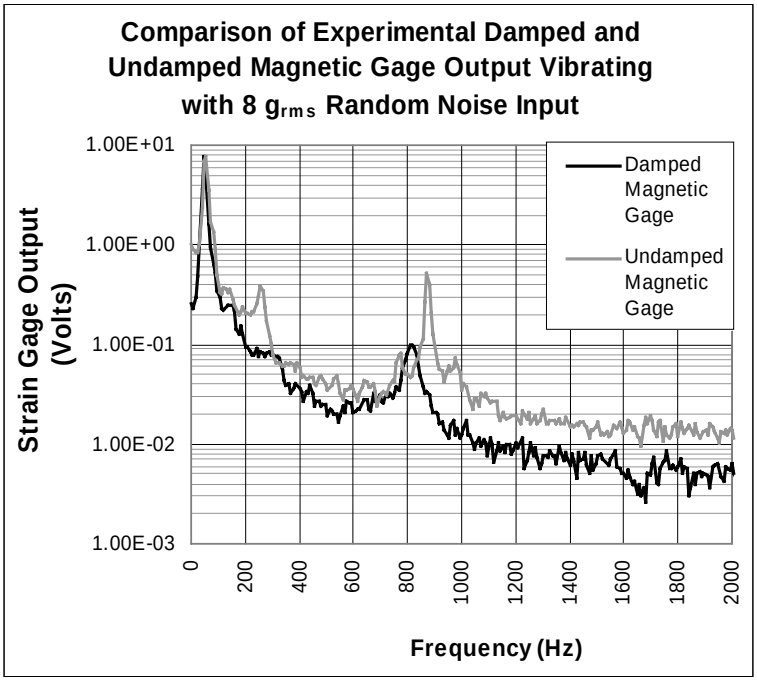

Figure 46: Comparison of Prototype 2 Damped and Undamped Strain Gage Output for 8 g_{rms} test

Figure 46 shows that the magnetic damper has a significant effect on the vibration of the skin friction gage. The eddy current damper affected the second bending mode the most. This can be assumed to be because of the frequency dependence of magnetic damping. The amplitude of the second mode was reduced from .515 Volts to .099 Volts, and the peak was shifted down in frequency from 872 Hz to 816 Hz.

A minor spike can also be found at around 280 Hz with the undamped results, this corresponds with the 310.2 Hz frequency found in the frequency response function analysis. This could perhaps be attributed to motion on the second axis of the beam. The motion of this axis could be excited because the gage mount may not have been perfectly situated on one strain gage axis. In order to determine if this was an issue, the gage underwent another 8 g_{rms} vibration, yet the axis perpendicular to the direction of motion (the off-axis) was monitored instead of the active axis. A comparison of the on-axis and off-axis results are plotted in Figure 47. It is apparent from this graph that the off-axis was excited, yet the off-axis amplitudes were only approximately 5 % of the on-axis amplitudes. So, the off axis was not excited to a large enough degree which would cause the mode at 280 Hz.

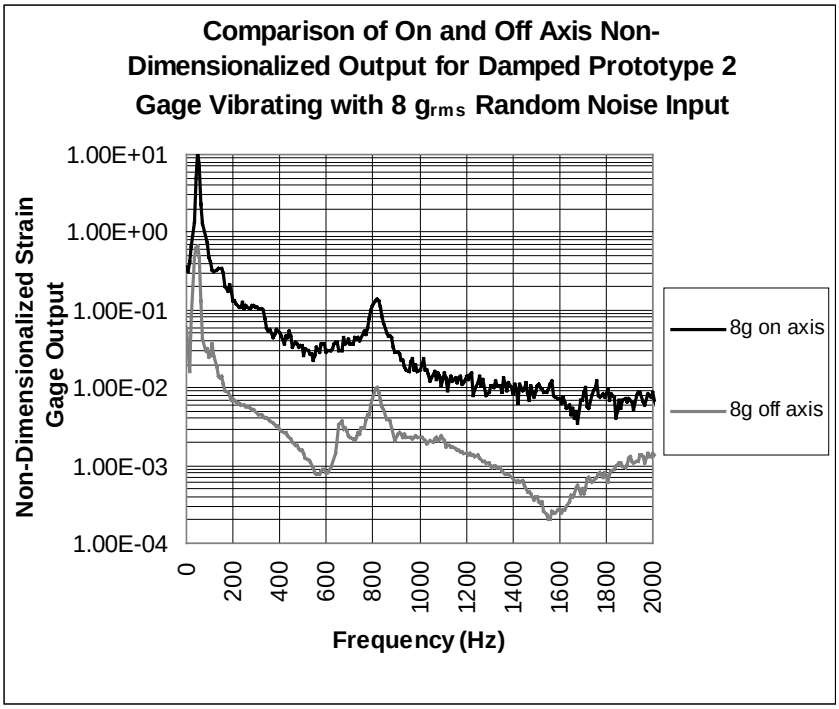

Figure 47: Comparison of the On-Axis and Off-Axis Output for an 8 g_{rms} Random Noise Vibration

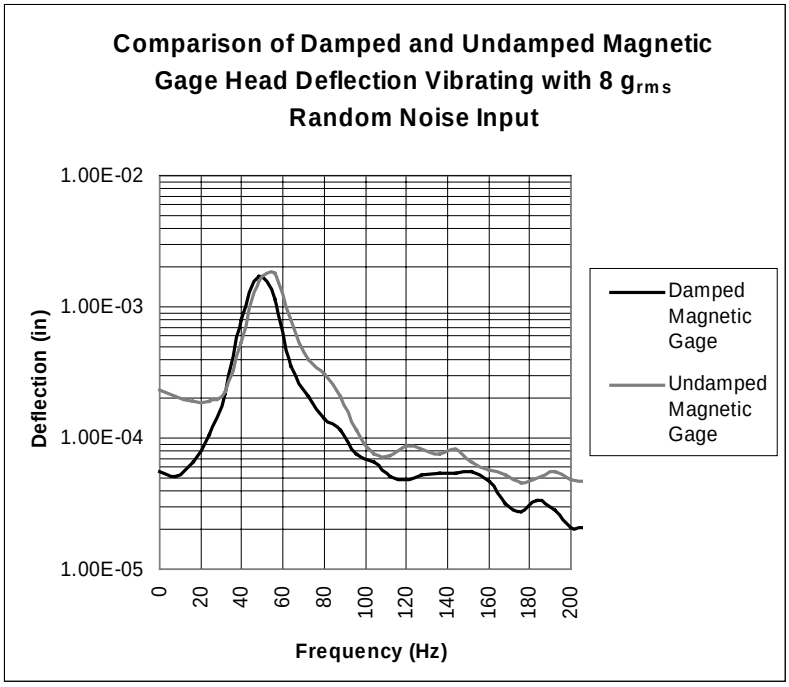

Figure 48: Prototype 2 Gage Deflections at First Bending Mode with 8.0 g_{rms} Random Noise Input

The deflection of the head at the first bending mode natural frequency was an important piece of data. This data would indicate if the head would contact the housing of the gage during heavy vibrations. The voltage output from the gage could be related to a force at the head, which could then be related to a deflection at the head through the methods described in Chapter 3.4 Equation 31. Figure 48 shows more dramatically the effects of the eddy current damper on the first mode. Only the data from the 0 to 200 Hz is plotted, so that the effects of first mode are clearer.

Figure 46 showed that the eddy current damper provided a greater effect on the second bending mode than the first. Figure 48 showed that the amplitude of the first bending mode remained at about the same magnitude with only a slight reduction from $1.80*10^{-3}$ inches and reduced to $1.57*10^{-3}$ inches. The damped configuration also caused a slight shift of the natural frequency from 56 Hz to 48 Hz. The effect of this vibration was large with respect to the magnitude of the anticipated output due solely to the skin friction of the flight profile. According to NASA, the flight profile expected shear forces on the FTF-II plate at a range from 0.3 psf to 1.45 psf. Figure 49 is a plot that uses the lower bound of this range to non-dimensionalize the strain gage output. This produces the worst case scenario in terms of noise due to the large deflections from vibration and the smallest deflection occurring due to

skin friction during the flight profile. Figure 49 is a plot of the shear force output of the strain gage normalized with the expected shear force corresponding to the F-15 flight profile at Mach 0.7 and 45,000 feet (0.3 psf).

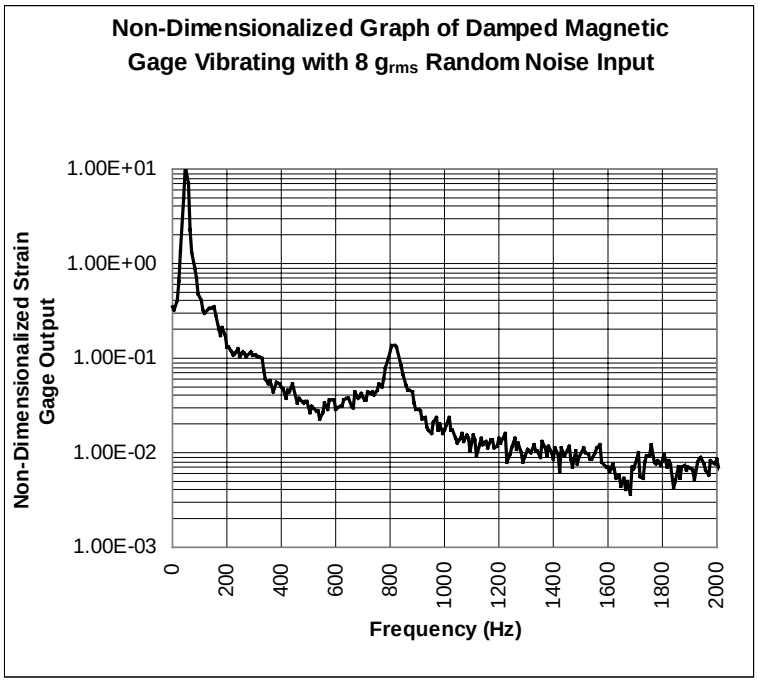

Figure 49: Non-Dimensionalized Plot of Damped Prototype 2 Strain Gage Output Normalized at 0.3 psf

It is apparent from Figure 49 that at the first mode natural frequency the strain gage output from the vibration is 9 times the value of the quantity which will be measured. This is an improvement on the factor of 30 found during the first gage prototype, but still having the noise output larger than the output of the desired measurable quantity is unacceptable.

6.4.3. Experiment 3: Smooth Flight Vibration Simulation (2.0 g_{rms})

It was anticipated that the gage might experience a smoother flight than the rigorous Curve A vibration level that NASA required. The third experiment of the vibration analysis of the skin friction gage involved the simulation of a random vibration test curve similar to the Curve A used in the second experiment. Again, the only difference was that the gage was shaken at 2.0 g_{rms} instead of 8 g_{rms}. This smaller acceleration loading was a more accurate

simulation of the vibrations that the FTF-II plate would undergo during a typical smooth flight. A plot of the strain gage output is shown in Figure 50.

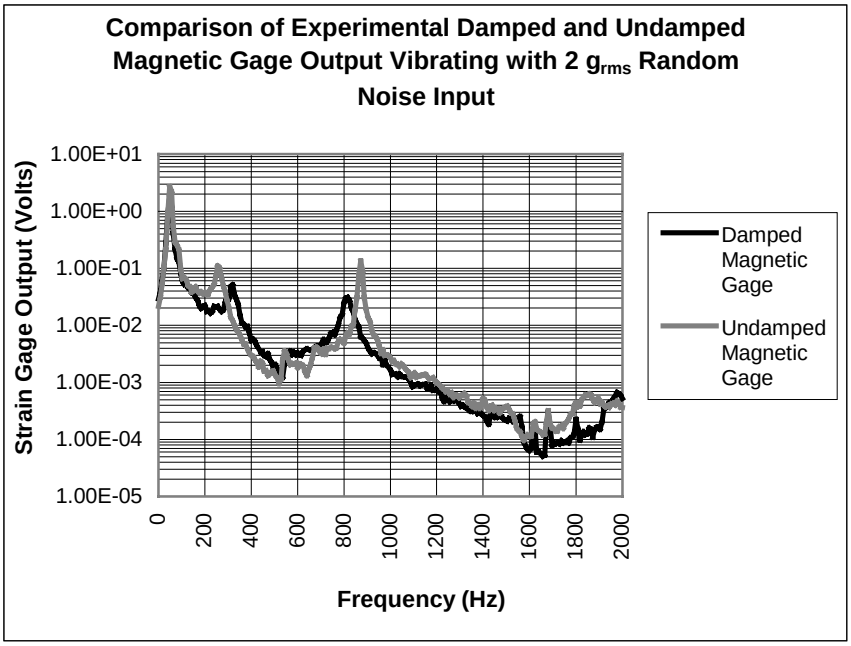

Figure 50: Comparison of Prototype 2 Damped and Undamped Strain Gage Output for 2 g_{rms} Random Noise Input

Figure 50 shows that the magnetic damper has an effect on the vibration of the skin friction gage even at smoother vibrations. Again, the eddy current damper affected the second bending mode the most. The amplitude of the second mode was reduced from 0.134 Volts to 0.0271 Volts, and the peak was shifted to down in frequency from 872 Hz to 824 Hz. There also appears to be more emphasis on the secondary mode found at 280 Hz, which did not appear as strongly during the 8 g_{rms} loading. This may have occurred because the skin friction gage was not lined up perfectly on its axis, or due to a torsional mode.

Figure 51 is a detailed plot of the deflection of the gage head at the first bending mode. This data would indicate if the head would contact the housing of the gage during vibrations. Figure 51 shows more dramatically the effects of the eddy current damper on the first mode. Only the data from the 0 to 140 Hz is plotted, so that the effects of first mode are clearer.

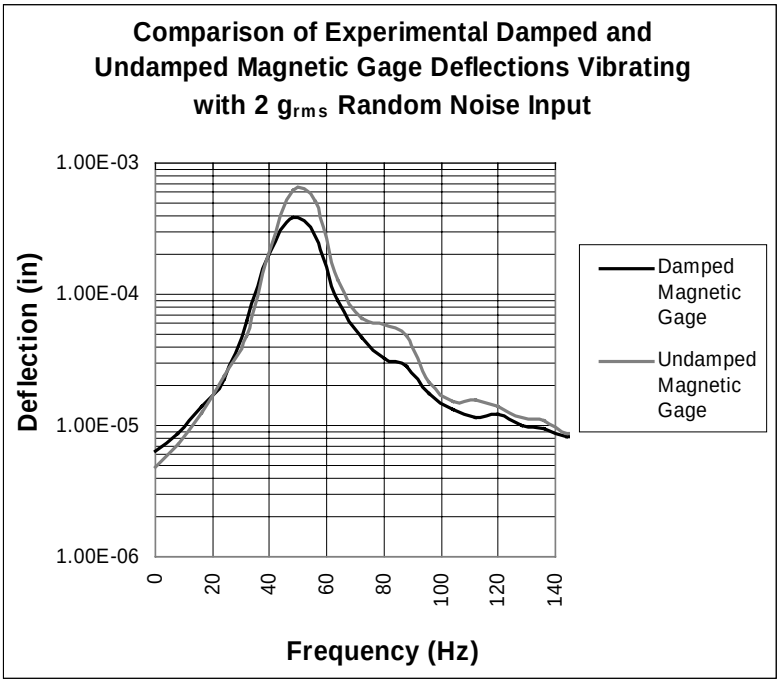

Figure 51: Prototype 2 Gage Deflections at First Bending Mode with 2 g_{rms} Random Noise Input

The amplitude of the damped vibration showed a 34 % reduction from $6.1x10^{-4}$ inches and reduced to $4.0x10^{-4}$ inches. The damped configuration also caused a slight shift of the natural frequency from 56 Hz to 49 Hz. As expected, the effect of this 2.0 g_{rms} vibration was not as large as the 8.0 g_{rms} results.

The flight profile anticipated shear forces on the FTF-II plate at a range from 0.3 psf to 1.45 psf. Figure 52 is a plot that uses the voltage output of the lower bound of this range to non-dimensionalize the strain gage output. This is a plot of the shear force output of the strain gage normalized with the expected shear force corresponding to the F-15 flight profile at Mach 0.7 and 45,000 feet (0.3 psf). It is apparent from Figure 52 that at the first natural frequency the strain gage output from the vibration is approximately 1.1 times the quantity which will be measured. Having the noise output comparable to the output of the desired measurable quantity produces poor experimental results.

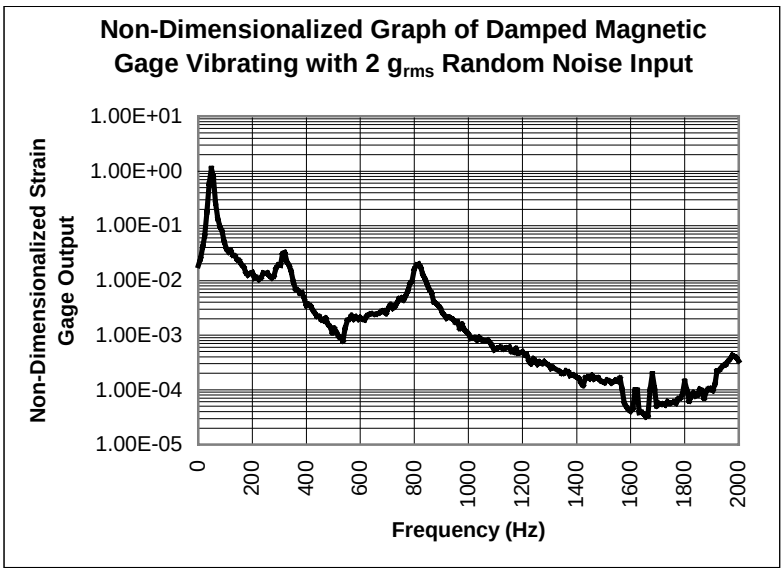

Figure 52: Non-Dimensionalized Plot of Prototype 2 Strain Gage Output Normalized at 0.3 psf

6.5. Prototype 2 Conclusions

The vibration characteristics of the second prototype were an improvement on the first prototype, but it can be concluded from these experiments that the vibration characteristics of the damped skin friction gage were not adequate for its intended use on the F-15 mounted FTF-II plate. This was primarily due to the poor characteristics at the first mode, yet the damped characteristics at the second mode showed promise. The magnetic damper improved the vibration characteristics of the skin friction gage, yet not to a satisfactory degree. This gage would not give accurate results of skin friction when the gage vibrated near its first mode natural frequency. Vibrations which created noise levels up to 9 times the value of the anticipated skin friction measurement produce unsatisfactory experimental output. Both the 8 g_{rms} and the 2 g_{rms} loadings produced poor vibration characteristics in the skin friction gage. As expected, the 2 g_{rms} output produced better results, and produced an output due to vibration that was on the same order as the quantity being measured. So, this gage must be redesigned in a manner that would decrease or eradicate the vibration effects at the natural frequency.

Chapter 7. Prototype 3 - Electromagnet Eddy Current Damper Configuration

7.1. Objectives and Rationale for Design

The rationale for the third skin friction gage prototype involved the improvement of the damping characteristics of the second skin friction gage prototype. This can be done in a variety of ways. First, the system damping can be increased which would decrease the amplitude at the natural frequency and consequently decrease the effects on the output of a vibrating system. This can be done using an electromagnet, which would produce a stronger magnetic flux. With this change, the strain gages would need to be tested to make sure that their output was not distorted by the stronger magnetic flux densities. Another concern would be the heat produced by the current flowing through the electromagnet wires. In order to increase the magnetic flux density, the current must increase. Whereby, heat is produced by the proportionality of Equation 32.

$$\text{Heat} \propto i^2R. \qquad [32]$$

The current is squared, so effort must be place into keeping the current low enough, so that the heat does not create a problem with the strain gage while the electromagnet is operating.

The increase in damping was accomplished by replacing the permanent magnets used in the prototype 2 gage with a closed-loop electromagnet eddy current damper system. The Alnico 5 permanent magnets were capable of producing as much as 0.18 Teslas (1800 Gauss) in the magnetic gap. The small electromagnets used in these applications are capable of producing well over 1.0 Teslas (10,000 Gauss). This is important, because the damping coefficient relation associated with eddy current damping in Equation 18 is related to the square of magnetic flux density. Thus, the electromagnet should be able to produce more than 30 times as much damping.

The size of the electromagnet was set from a variety of new parameters stemming from the electromagnet. The overall increase in size of the gage was associated with the

required size of the electromagnet capable of producing the required damping. Electromagnets tend to be bulky, so the entire gage will become larger than the second prototype. For the flight test application of this gage, growth laterally was not a critical issue, but maintaining a reasonable length remained a concern. If the gage beam became to long, the unit might become more sensitive to vibration. Also, paramount to this issue was the required distance of the electromagnet from the strain gage unit. Due to the increased level of magnetic flux density flowing through the electromagnet, a stronger level of leaked magnetic flux density capable of distorting the output from the gage could be present. It was also important that the flux density associated with leakage be low enough that it did not induce movement of the ferromagnetic beam in the DSC unit. These sizing requirements were then compared with the sensitivity and weight minimization trade studies of Figure 34 and Figure 35.

The maximum diameter of the electromagnet was sized by the maximum diameter of Hiperco alloy that could be purchased from Carpenter Technologies (3.0 inch diameter rod). Equation 25 was used to determine the remaining dimensions of the electromagnet. This design equation utilized the number of winds of wire along with the amount of current used to produce the required magnetic flux density. Larger wires with greater insulation can support more current, but this increases the size of the gage. Increased current leads to increased heat production, which could pose a potential problem to the strain gages. Another parameter that could be varied was the gap between the poles. Each parameter was varied until an electromagnet fitting the diameter requirements, minimum length, and reasonable current was achieved.

7.2. Design configuration Description

7.2.1. Electromagnet design

The final design for the electromagnet possessed two spools, each containing 1154.2 winds of round Gauge 24 Copper Magnet Wire, with a maximum of 1.60 and 1.67 amps flowing through them, respectively. The gap between spools was 0.1425 inches from pole surface to pole surface. This dimension needed to be minimized according to Equation 25 in

order to maximize the magnetic flux density flowing across the gap. The gap was minimized by the available assembly capabilities. It allowed a .04 in. (1 mm) gap between the surface of the conductor disk and the pole surface. A smaller gap could potentially cause contact between the conductor and the electromagnet pole. The required size of the pole surface area was determined to be 0.75 inches with a conductor disk of 0.80 inches. These dimensions were chosen using trade studies which varied those parameters. Each spool was linked with a 3.0 inch diameter yoke so that the spools were linked and the electromagnet became a closed loop system.

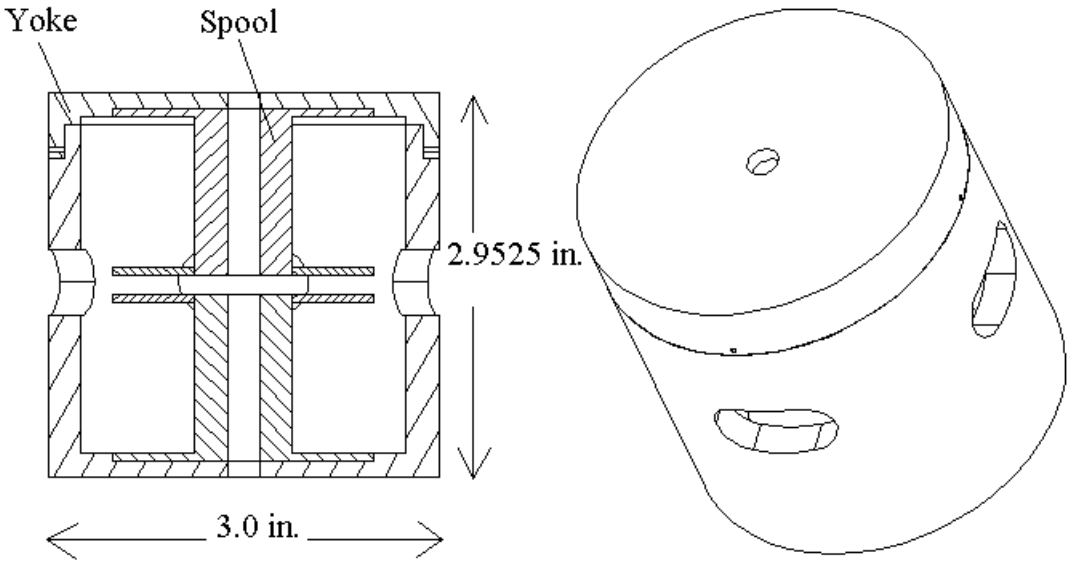

SCALE 1.200

By: Alexander Remington	Electromagnetic Skin Friction Gage	Date: 12/8/98
Prof. Schetz	Electromagnet Cross-Section	Material: Hiperco

Figure 53: Drawing of Electromagnet Used in Prototype 3

The magnetic flux will follow the path of least reluctance. Thus, a closed loop system was ideal for this application, because the magnetic flux density would stay contained in the yoke of the electromagnet instead of leaking out of the electromagnet. This system would minimize the magnetic flux density at the location of the strain gages. A CAD rendering of the electromagnet is shown in Figure 53.

For the magnetic verification portion of this experiment, the gaussmeter shown in Figure 22 was used to measure the magnetic flux densities inside the gage. Figure 54 shows a comparison of the theoretical estimations of the flux density in the gap of the electromagnet compared and the experimentally determined values. The analytical curve took into account the estimated losses associated with the geometry of the design, as well as a saturation limit with the electromagnet of approximately 11,000 Gauss. The potentiometer setting shown in Figure 54 represents the additional resistance added to each wire from the potentiometers.

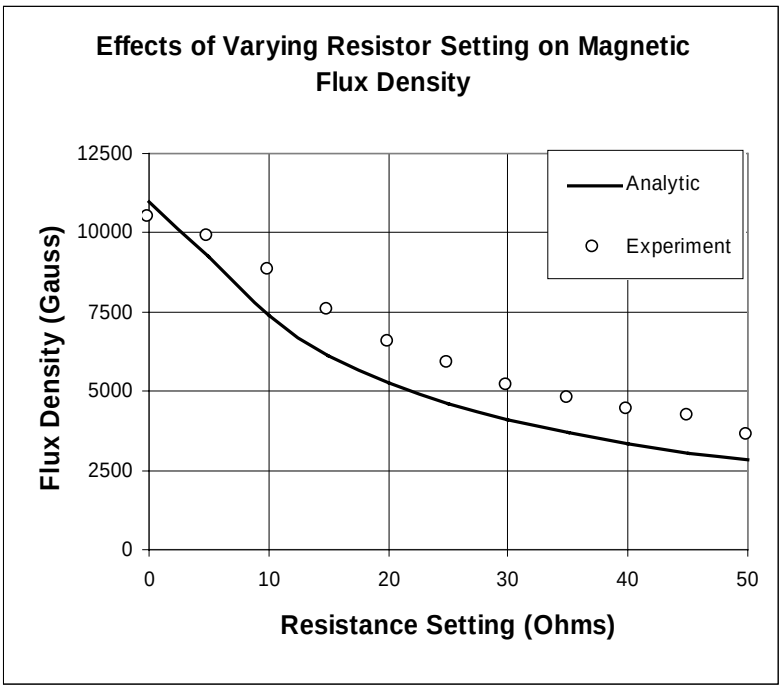

Figure 54: Comparison of Theoretical (with 5 % Safety Factor) and Experimental Values of Flux Density

It is recommended to use a safety factor when designing an electromagnet, because losses on the order of 5% can be expected due to the shape of the electromagnet and losses associated with the areas of contact in between each piece of the electromagnet. The areas of contact between the individual pieces of the electromagnet were not perfectly in contact due to machining imperfections. Thus, the areas of contact are assumed to be small air gaps which the magnetic flux must cross in order to continue its circuit. From Equation 25, the maximum calculated flux density at the gap of this electromagnet was B=13,084 Gauss (1.3084 Teslas), and the anticipated level assuming losses and saturation would be approximately B=10,367 Gauss (1.0367 Teslas). A variety of levels of flux density could be

achieved with this configuration. The current level of the wires inside the electromagnet could be decreased by increasing the resistance with the use of potentiometers that were linked to the electromagnet wires in series. The theoretical predictions underestimated the actual values by more than the 5 % safety factor. It can be assumed that the Hiperco alloy as well as the junction between the electromagnet parts provided negligible losses. The high permeability of Hiperco may have contributed to the large experimentally determined values. A variety of profiles were measured to determine both the characteristics inside and outside of the electromagnet at different current levels.

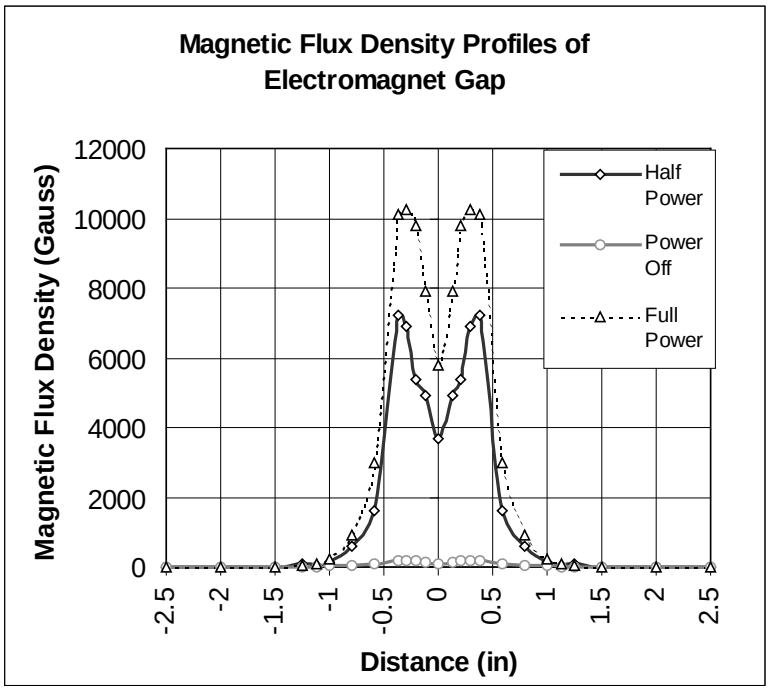

Figure 55: Measured Electromagnet Interior Flux Density Profiles

The flux density profile found inside the gage (shown in Figure 55) appeared as one might expect. It can seen that the flux density tended to drop off in the center where there was a hole in the spool, and the flux density diminished rather quickly beyond the pole edge. In this graph, a distance of zero inches represented the centerline of the gage. The pole edge was ± 0.375 inches beyond the centerline, and the yoke edge was ± 1.5 inches beyond the centerline. So, it was important to note that the conductor was operating in the regions of largest magnetic flux density.

Another issue was the magnetic flux density at the location of the strain gages, a distance of 1.75 inches from the yoke edge. Figure 56 showed that these values were well below the levels that cause interference. The flux density levels were close to the minimum level of measurement capable in a room with a variety of electrical equipment in it. The magnitude of magnetic flux density associated with the earth is approximately 0.7 Gauss. In a room with steel beams and electronics within it, the level of flux density found in the room could be as large as a few Gauss. Thus, it could be assumed that there was a negligible level of magnetic interference associated with the strain gages and the operation of the electromagnet.

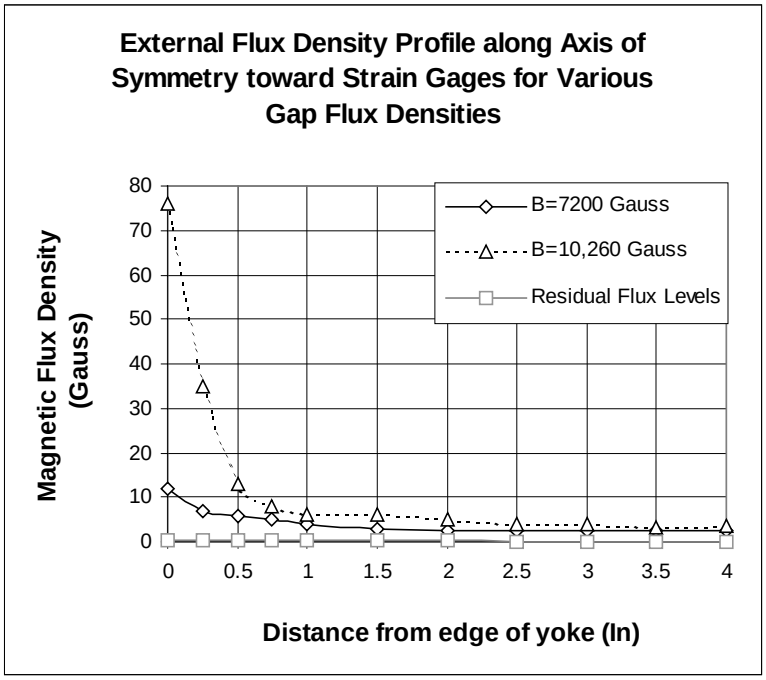

Figure 56: Measured Magnetic Flux Levels at the Strain Gage for Various Levels of Operation

7.2.2. Prototype 3 Gage Design

After the electromagnet had been sized, the size of the skin friction gage was determined. The tip of the Kistler-Morse Sensor was only in a maximum magnetic flux density field of 35 Gauss when the yoke was 0.25 inches from the gage tip, and at this location the magnetic interference with the strain gages was minimized. The position of the electromagnet from the DSC unit sized the length of the gage, and the diameter of the head was sized with this length and the sensitivity trade studies of Figure 34. Thus, the length of

the gage was 4.78 inches, with a sensing head diameter of 1.2 inches. The diameter of the electromagnet reached three inches pushing the outer housing to a diameter of 3.375 inches. So, the girth of the gage grew significantly. The flange, which was required to mount the gage on a test plate, extended even further to a diameter of 4.375 inches. Consequently, this method produced a gage of large proportions compared to other designs at Virginia Tech. Figure 59 shows a picture of the gage. Figure 57 shows the internal arrangement of the gage, and Figure 58 shows the pertinent dimensions of the third skin friction prototype.

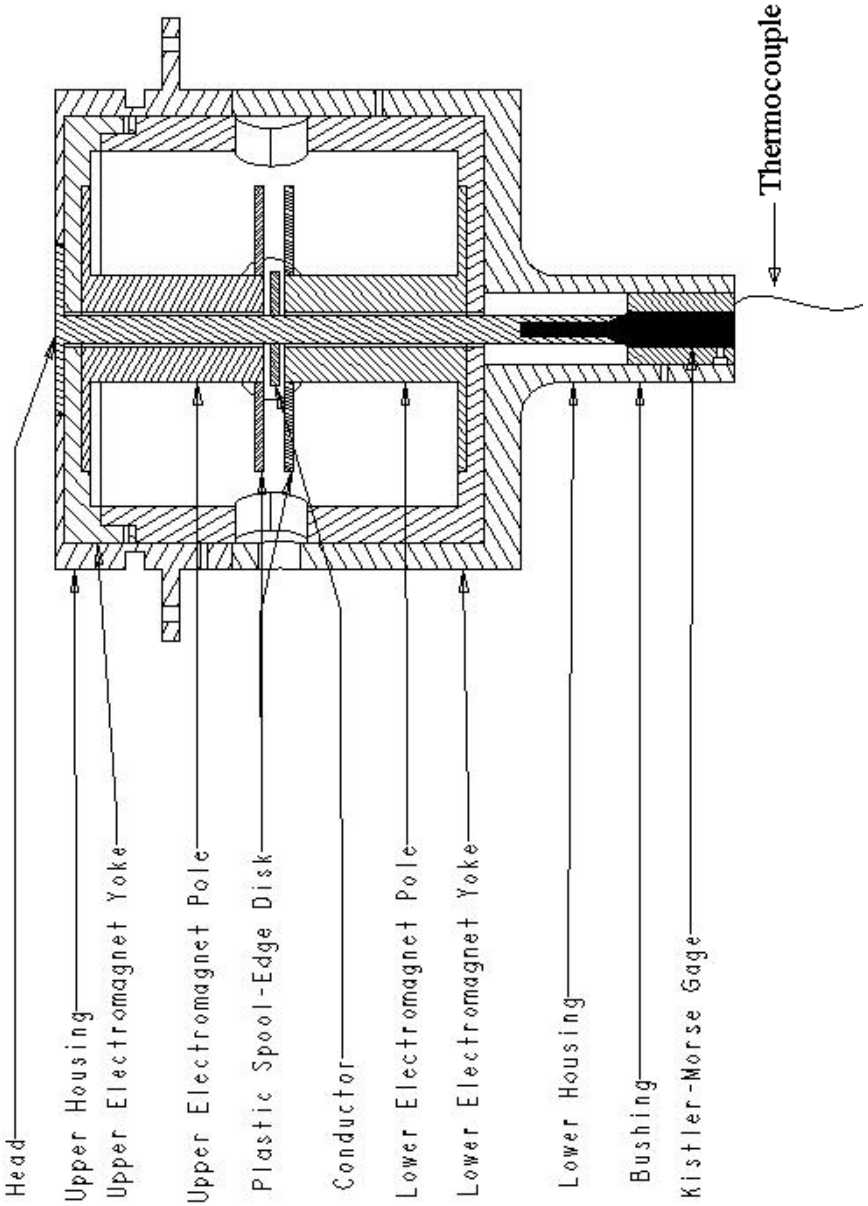

Figure 57: Prototype 3 Internal Arrangement

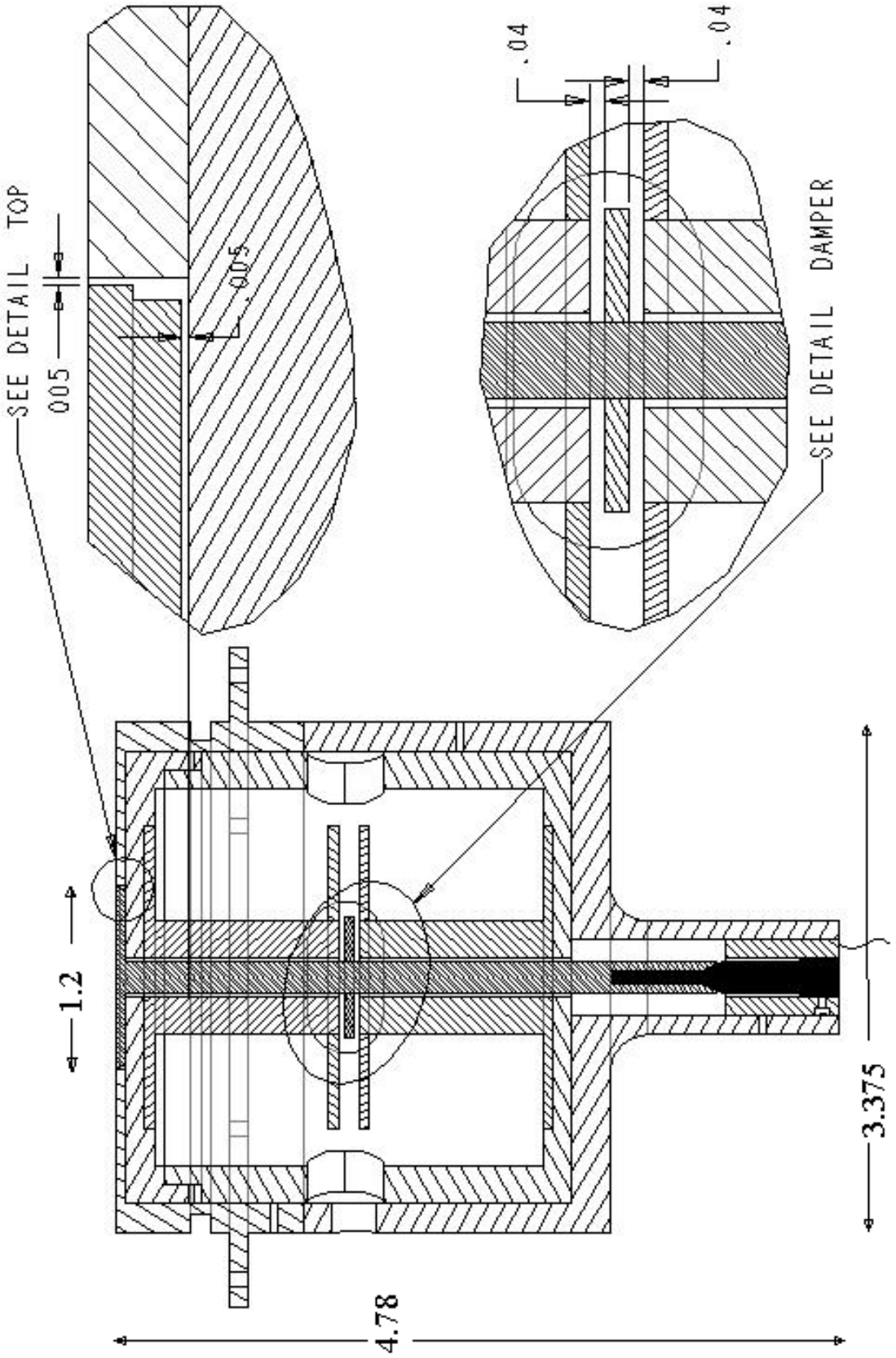

Figure 58: Dimensions of Third Skin Friction Gage Prototype

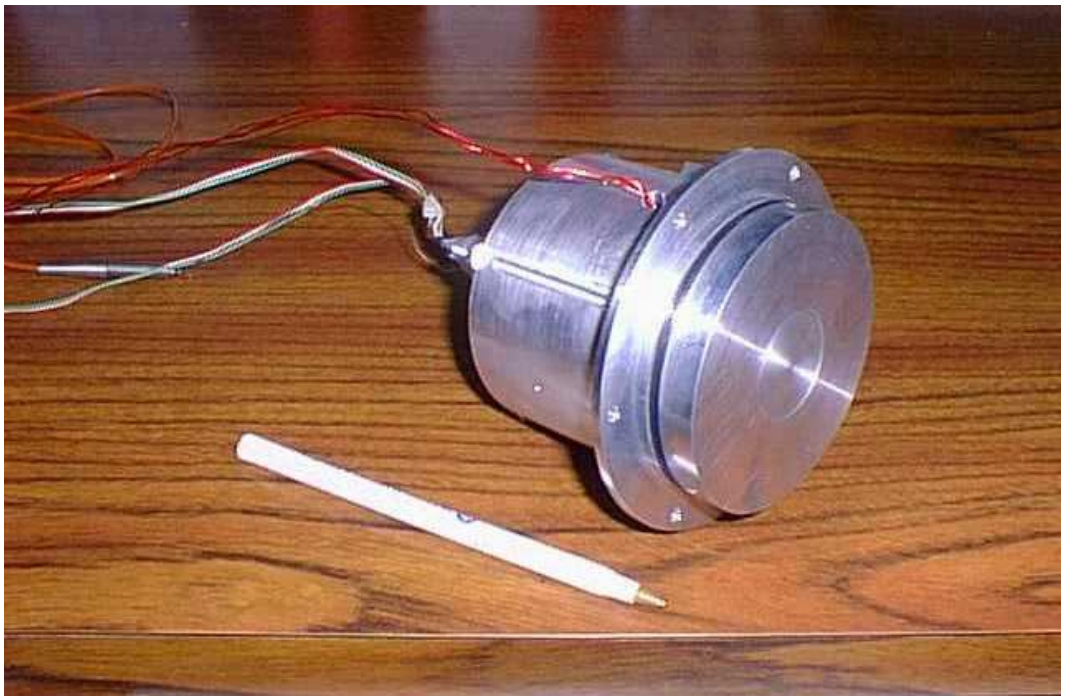

Figure 59: Photograph of Prototype 3 Electromagnetically Damped Skin Friction Gage

From the internal schematics of Figure 57, it can be seen that the skin friction gage was a good deal more complicated than previous designs, yet the general structure was only a modification of the prototype 2 gage. Figure 58 shows the large dimensions of the gage, as well as the important gap sizes. From Figure 59, the bulky nature of the gage can be seen. A pen has been placed next to the gage in an attempt to convey the size of the object. The electromagnet lead wires exiting the side of the gage and the strain gage lead wires and thermocouple wires exiting the base can also be seen in this picture.

7.3. Prototype 3 Results

7.3.1. Thermal Verification Tests

The first tests performed involve the assessment of the gage's ability to operate under the temperatures experienced during the electromagnet operation. The third prototype gage was activated, and the temperature at the thermocouple was monitored over a period of 15 minutes (900 seconds). The electromagnet was operated at a variety of different current settings, to show the advantage of the lower current operation. The thermocouple, located next to the strain gage, was sampled at a rate of 100 Hz for the time history plot shown in Figure 60. In addition to the temperature time history plots, the strain gage output was

simultaneously monitored over the fifteen minute (900 second period) to ascertain the effects of temperature drift. The strain gage temperature drift plots are shown in Figure 61.

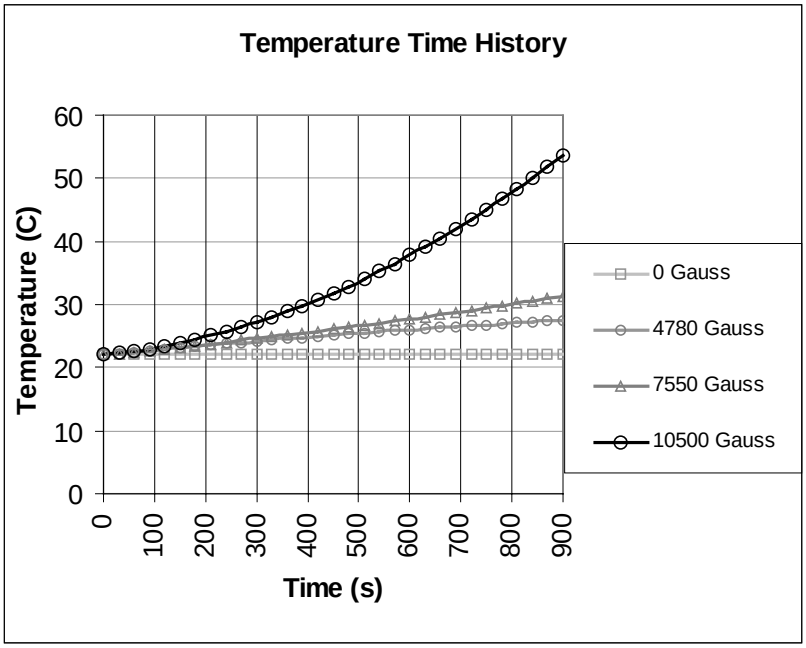

Figure 60: Temperature Time History of Thermocouple Located at the Strain Gage of the Prototype 3 Gage Operating at Different Current Settings

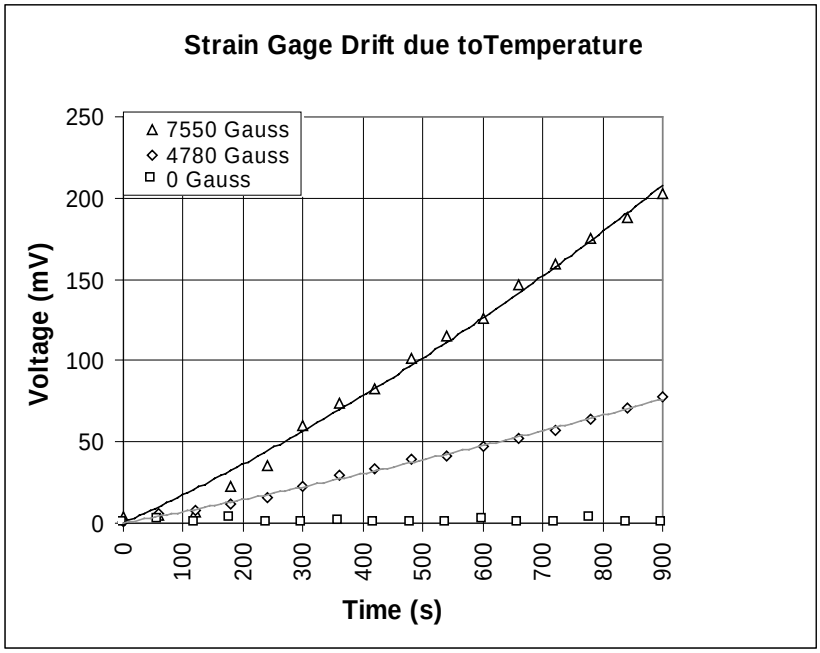

Figure 61: Prototype 3 Strain Gage Drift due to Temperature at Various Current Settings

It can be ascertained from Figure 60 that the temperature increase over a long period of time is substantial. The duration of wind tunnel tests are a much shorter duration than these temperature tests. Most wind tunnel test runs would require the electromagnet to operate only over a 12 second period, and over those periods of time, the temperature drift is negligible. Temperature effects over a large time duration are a matter of concern for flight tests, in which the gage may need to be operational for nearly 15 minutes. A 200 mV drift over 15 minutes only produced a drift of 10% of the expected output due to shear stress (2 Volts). This is substantial, yet not an unreasonable level of error.

7.3.2. Experiment 1: Natural Frequency Measurement

The experimental vibration analysis for the Prototype 3 gage was performed in the same general manner as the previous two prototypes, except for a minor alteration in the set-up of the vibration. Because the gage was going to be mounted vertically on the bottom test plate, the gage was shaken in the same orientation. A picture of the free-free setup can be seen in Figure 62. The gage was hung from a crane with bungee cords and mounted onto the shaker with a short sting. It was then shaken under the same conditions as the previous two prototypes.

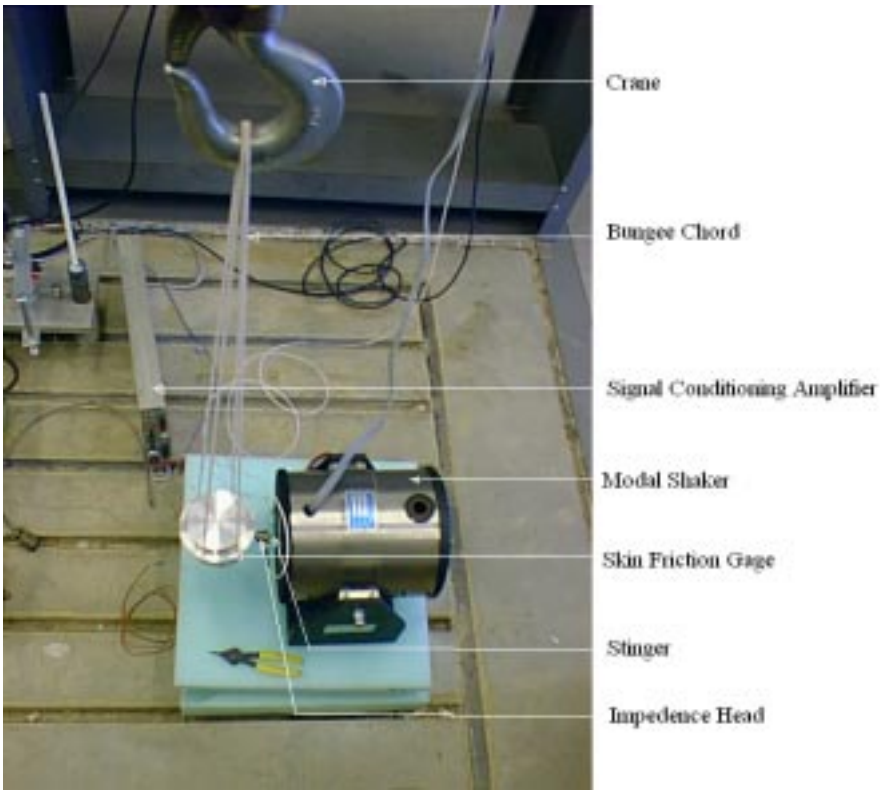

Figure 62: Photograph of Prototype 3 Vibration Setup

The first experiment of the vibration analysis was the measurement of the natural frequency of the skin friction gage. This was done in the same manner as the natural frequency measurement of Prototype 1. The gage was shaken with a large VTS modal shaker in a uni-axial direction with a random noise input at a level of 25 mVpk (2.5 g_{rms}). The gage was tested over a frequency range of 0 to 3200 Hz. This was the smallest range available to the signal analyzer which encompassed the 0 to 2000 Hz range which NASA specified.
Figure 63 shows the frequency response analysis of the third prototype. The analysis provided satisfactory results. Figure 64 is a graph of the phase of the frequency response function, and Figure 65 is a plot of the coherence of that data.

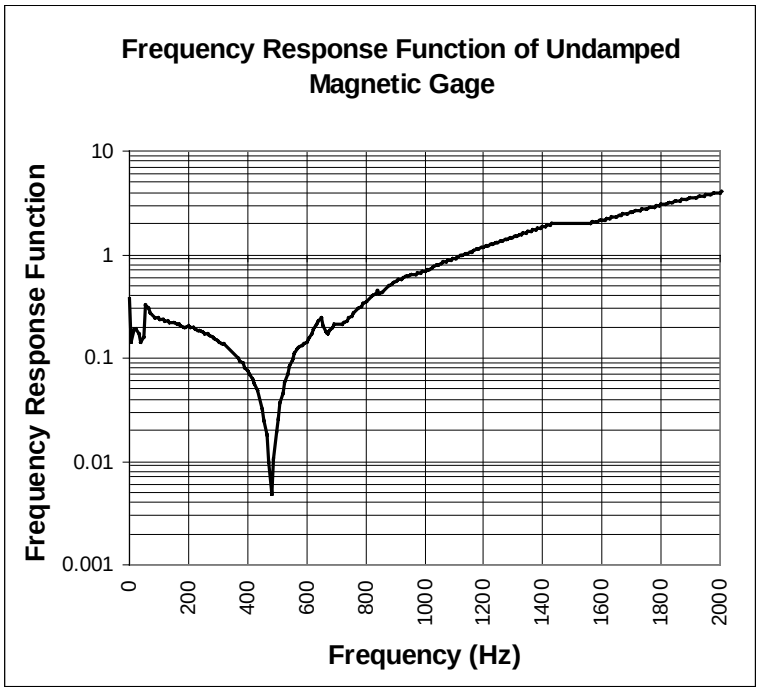

Figure 63: Prototype 3 Frequency Response Function

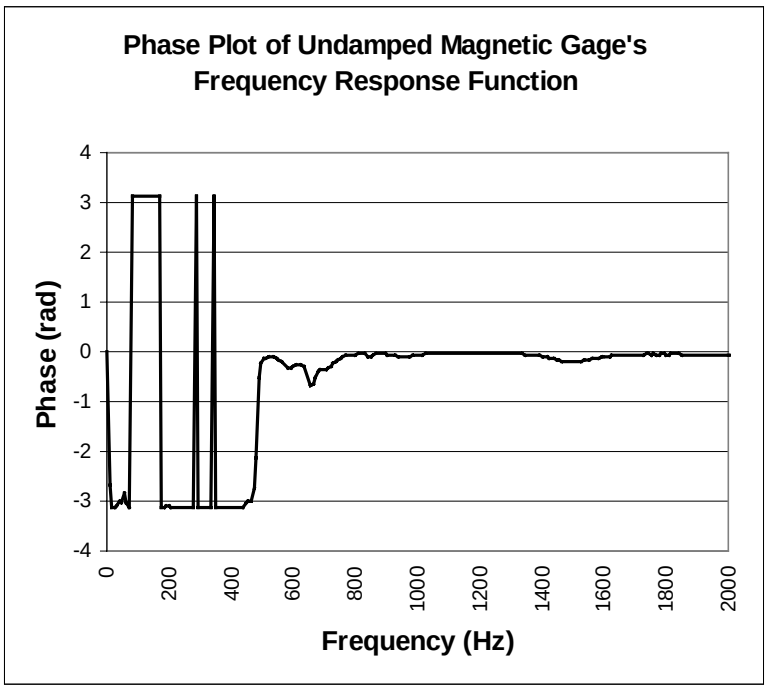

Figure 64: Prototype 3 Phase of Frequency Response Function

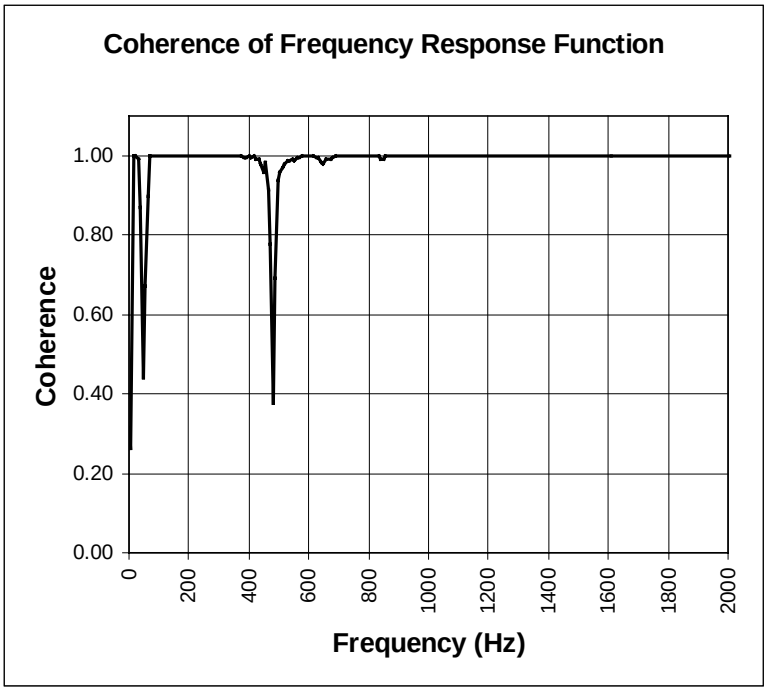

Figure 65: Prototype 3 Coherence of Frequency Response Function

From these three figures, two natural frequencies were determined, and these were compared with the values calculated from theory using BEAM6. The results are shown in Table 7.

Table 7: Comparison of Prototype 3 Theoretically Calculated and Experimental Measured Natural Frequency Modes

f_n Number	**Measured Natural Frequency, f_n (Hz)**	**Theoretical Natural Frequency, f_n (Hz)**
1	48	64.9
2	848	852.9

The theoretical calculations and experimental measurements corresponded well with each other. Both methods calculated two bending modes. The prediction from the theoretical model of the second bending mode matched the measurement very well. The prediction for the first mode was in the vicinity of the measurement, yet not as accurate as hoped.

The discrepancy in the values of the two sets of natural frequencies may be attributed to the same uncertainties found in the first two prototypes. Inaccurate estimates of the material properties of certain sections may cause some errors. Another potential inaccuracy of the model was in the cantilevered base assumption. A real system may actually flex slightly at the secured base of the gage causing a discrepancy between the theoretical and experimental models. Consequently, the theoretical calculations for the beam were made with a slightly stiffer beam than the actual beam. Thus, the theoretical calculations were slightly higher because the natural frequency is related to $\sqrt{k}$ for the general case of a cantilevered beam. Also, the BEAM6 program was unable to analyze visco-elastic materials. Thus, the silicone rubber casing surrounding the base of the Kistler-Morse unit may not have been modeled accurately, and may be a source of error.

7.3.3. Experiment 2: Simulation of NASA Random Vibration Test Curve A

The second experiment for the vibration analysis of the third prototype skin friction gage involved the simulation of a Random Vibration Test Curve provided by NASA in their vibration specification manual [36]. For acceptance on to the FTF-II the skin friction gage must be tested under representative FTF-II conditions. Vibration tests on all hardware must be performed using a random vibration test curve equivalent to the 8.0 g_{rms} to a maximum of 2000 Hz. NASA specified these conditions for operation in the flight test fixture as Curve A shown in Chapter 1.3.2.Figure 5.

This experiment followed the setup discussed in Figure 10 of Chapter 2.2 and of Figure 21 of Chapter 4.1. The experiment was run with an 8 g_{rms} random noise vibration from the VTS modal shaker. The strain gages from the skin friction gage were than hooked up to a signal conditioning amplifier that was then linked to the dynamic signal analyzer so that the response of the gage from the random vibration test curve could be analyzed.

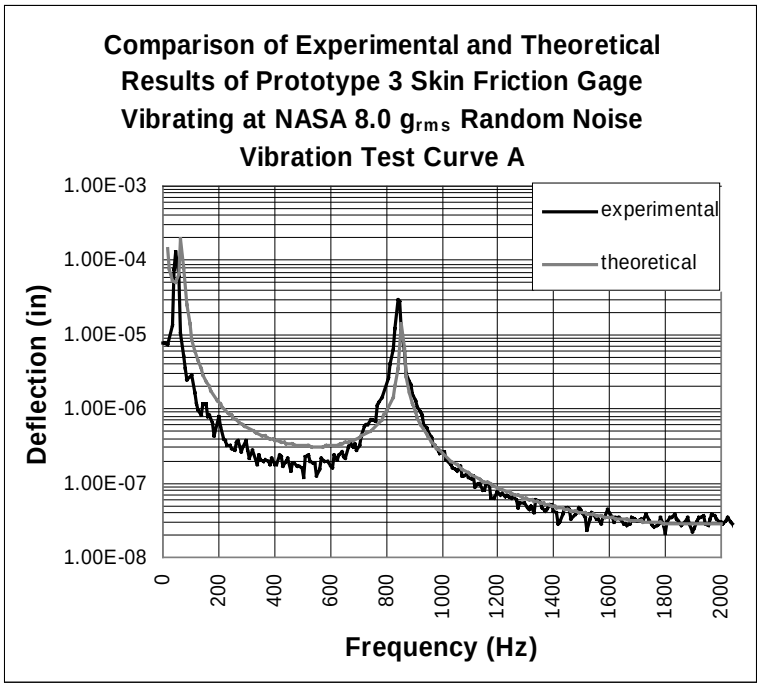

Figure 66: Comparison of Prototype 3 Gage Experimental and Theoretical Vibration Results at 8 g_{rms}

First, a comparison was made between the experimentally determined deflection values measured from the NASA Vibration Test Requirement Curve A and the predictions from the BEAM6 theoretical analysis. The comparison of the beam deflections over the frequency spectrum is shown in Figure 66. The general theoretical profile follows the measurement fairly well. The theoretical prediction of the first bending mode deflection was higher than the measured value, which is a common discrepancy found in all three prototype models. This discrepancy can be attributed to the BEAM6 programs inability to model visco-elastic damping. As mentioned previously, the Kistler-Morse Deflection Sensor Cartridge has a ring of silicone rubber surrounding the base of the unit that would dampen the vibration of the system. The program is only capable of modeling viscous damping terms. Thus, the theoretical results are under-damped at the first mode. The second mode matches fairly well with the experimental results. The theoretical model underestimated the amplitudes of vibration of the second mode slightly.

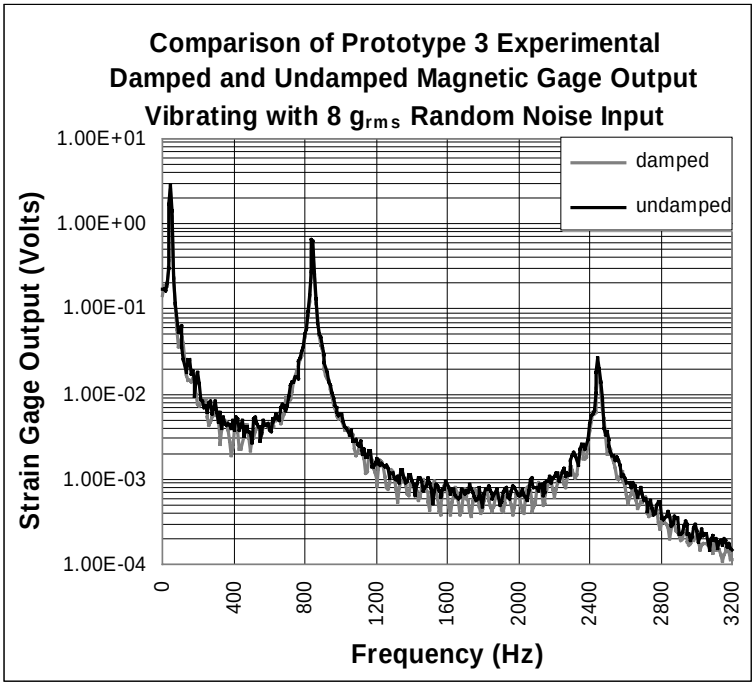

Figure 67: Comparison of Prototype 3 Gage Damped and Undamped Strain Gage Output for 8 g_{rms} Vibration Test

Figure 67 shows that the magnetic damper has an effect on the vibration of the skin friction gage. The damping appears to have a much less noticeable effect on the 8 g_{rms} case. The damping was at full power corresponding to a magnetic flux density level of 10,500 Gauss (1.05 Teslas). In an attempt to get a more detailed look at the effects on the first

bending mode of the gage, Figure 68 plots only the first bending mode. It can be seen from Figure 68 that there was there was a reduction in amplitude of the peak from 2.85 to 2.55 volts, which is not as significant a reduction as anticipated. The theoretical damped predictions are plotted in Figure 69.

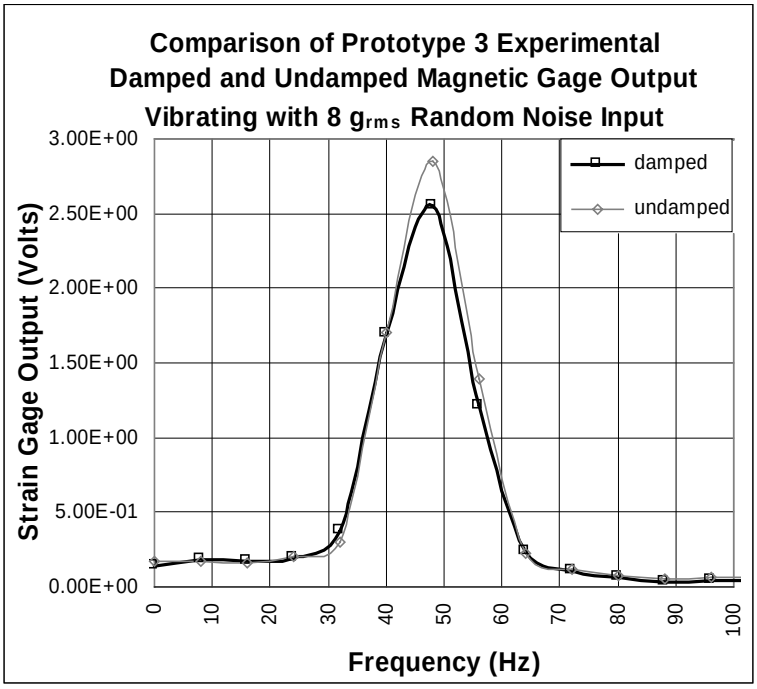

Figure 68: Prototype 3 Skin Friction Gage Output at First Bending Mode with 8.0 g_{rms} Random Noise Input

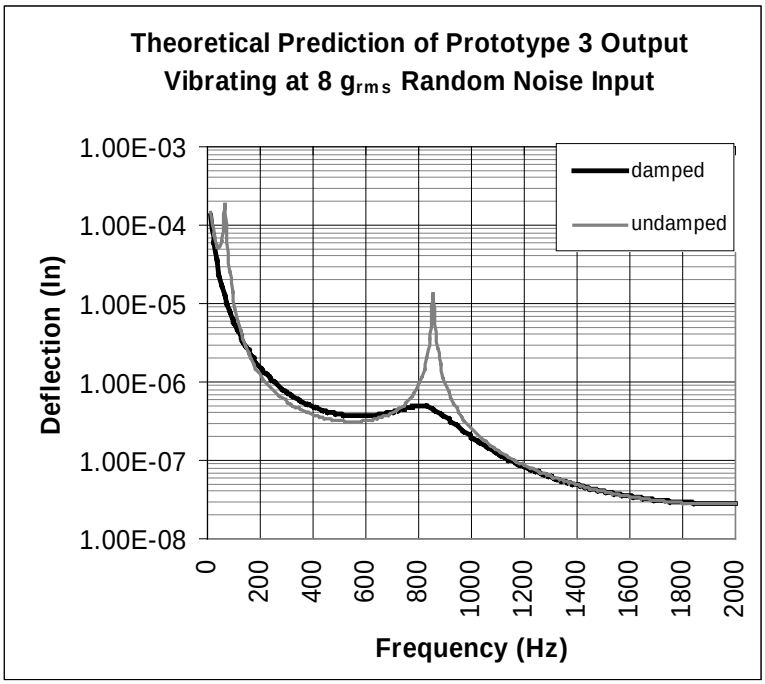

Figure 69: Theoretical Predictions of Prototype 3 Damping with 8 g_{rms} Vibration

From Figure 68 and Figure 69, it is apparent that there is a discrepancy between the predicted level of damping and the measured level of damping. A variety of reasons can be associated with this. First and foremost, there have been papers [35] which have found that the constant K used in the theoretical calculation of the damping coefficient is not a well understood term. As mentioned in Chapter 2.4, certain papers have predicted the value near 0.3, while others have found this value to provide erroneous results. Values as low as 0.05 have been reported.

The effect of this vibration with respect to the magnitude of the output due solely to the skin friction was not as pronounced as on the previous two gages. According to NASA, the anticipated shear forces for the flight profile on the FTF-II plate range from 0.3 psf to 1.45 psf. Figure 70 is a plot that uses the lower bound of this range, corresponding to the F-15 flight profile at Mach 0.7 and 45,000 feet (0.3 psf), to non-dimensionalize the strain gage output. This was the case that produced the worst case scenario in terms of vibration induced noise. It is apparent from Figure 70 that at the first mode natural frequency the strain gage output from the vibration is only 24 % of the shear force which will be measured. A 24 % noise level is large, but much more acceptable than a noise level comparable to the quantity being measured as found with the earlier prototypes.

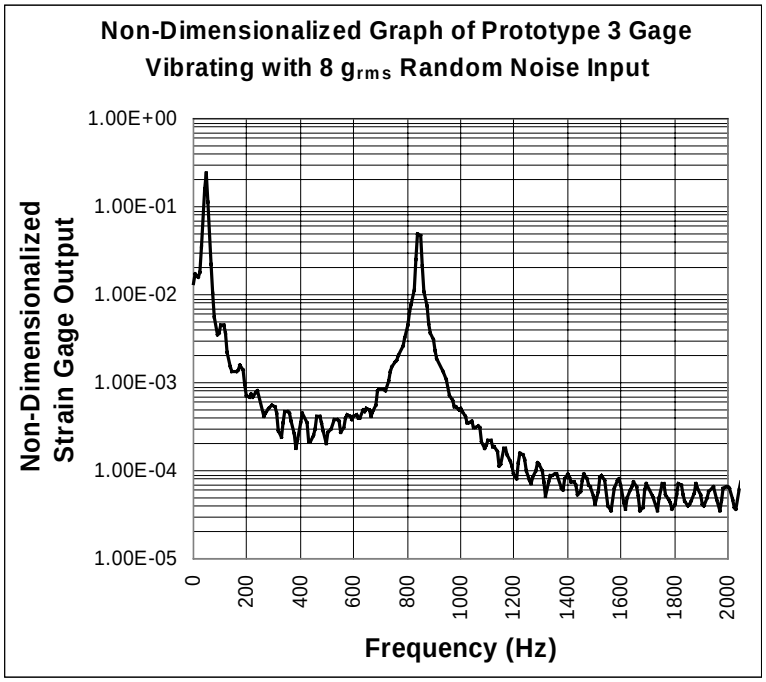

Figure 70: Non-Dimensionalized Plot of Damped Prototype 3 Strain Gage Output Normalized at 0.3 psf

7.3.4. Experiment 3: Smooth Flight Vibration Simulation (2.0 g_{rms})

It was anticipated that the gage might actually experience a smoother flight than the rigorous Curve A vibration level that NASA required. The third experiment of the vibration analysis involved the simulation of a random vibration test curve similar to the Curve A used in the second experiment. Again, the only difference was that the gage was shaken at 2.0 g_{rms} instead of 8 g_{rms}. This smaller acceleration loading was a more accurate simulation of the vibrations that the FTF-II plate would undergo during a typical smooth flight. A plot of the strain gage output normalized with the expected shear force corresponding to the F-15 flight profile at Mach 0.7 and 45,000 feet (τ_w=0.3 psf) is shown in Figure 71.

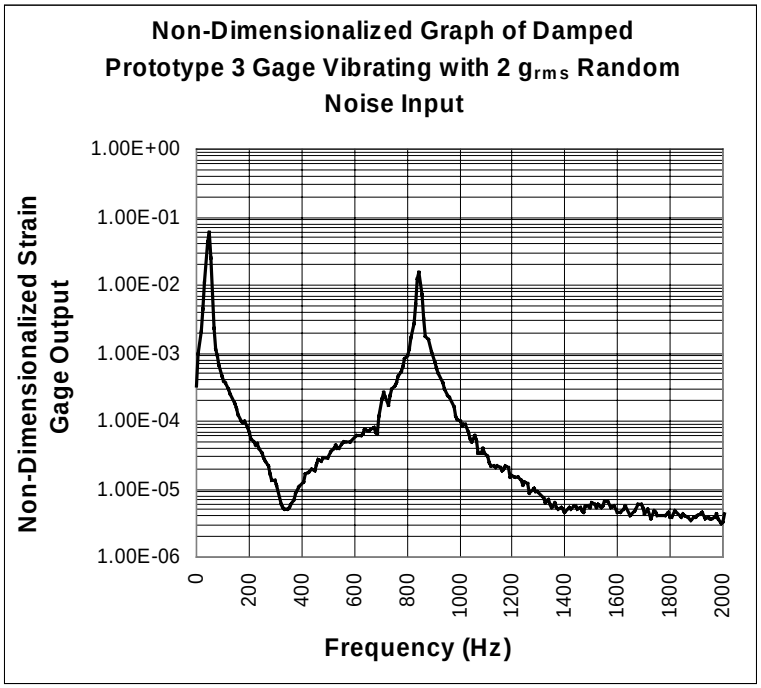

Figure 71: Non-Dimensionalized Plot of Prototype 3 Gage Strain Gage Output Normalized at 0.3 psf

Figure 71 shows that the electromagnetic damper still has an advantageous effect on the vibration of the skin friction gage even at smoother vibrations. The first mode would produce noise on the order of 6% of the full shear output, and the second mode would produce noise at 1.5%. These are much more reasonable and acceptable ranges of noise for operation.

It is important to look at the first bending mode more closely and see the effect that each magnetic flux density setting has on the vibration peak. Figure 72 is a plot of the

deflection of the gage head at the first bending mode from 0 to 200 Hz so that the effects at the first mode are clearer. The peak output induced by the vibration at 48 Hz was reduced by 33 % when the electromagnet was turned on to full power. The various settings provide the advantage of having the ability to reduce the amplitude of vibrations at the head yet produce less heat.

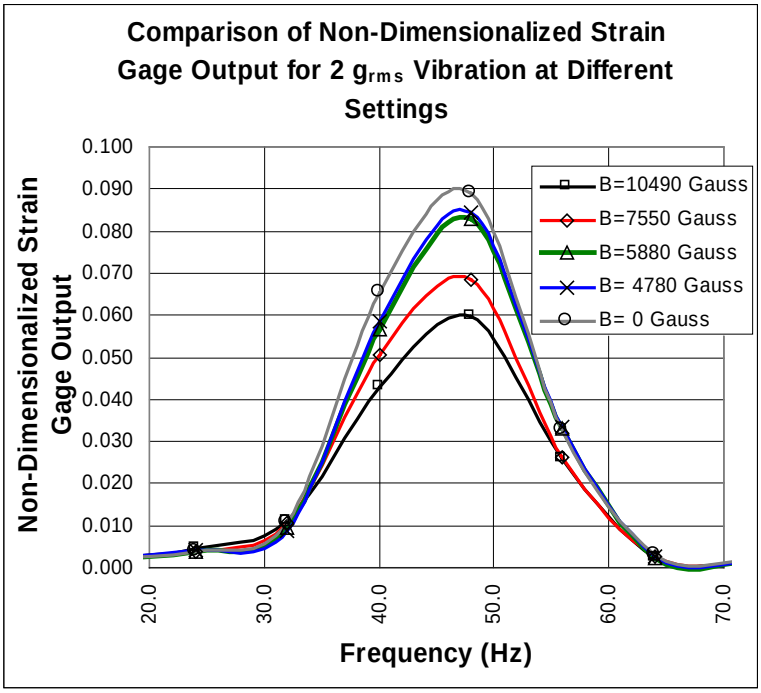

Figure 72: First Bending Mode Output of Prototype 3 Skin Friction Gage with 2.0 g_{rms} Random Noise Input

Another factor important in understanding the results of the Prototype 3 gage was the excitation of vibration in the axis perpendicular to the excited motion. Small perturbations perpendicular to the direction of induced excitation could excite the gage into motion perpendicular to the induced direction of motion. In order to determine if this was an issue, the gage underwent another 2 g_{rms} vibration with the axis perpendicular to the direction of motion (the off-axis) monitored instead of the active axis. A comparison of the on-axis and off-axis results are plotted in Figure 73. It was apparent from this graph that the off-axis was excited, yet the off-axis amplitude at the modes were only approximately 18 % of the on-axis amplitudes. So, the off-axis was not excited to a large enough degree to disrupt the on-axis output.

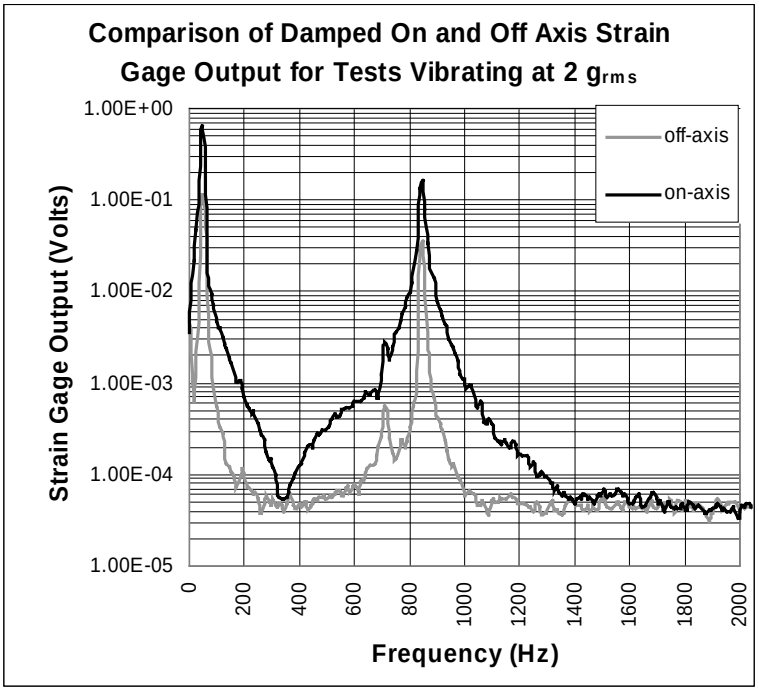

Figure 73: Comparison of the On-Axis and Off-Axis Prototype 3 Output for a 2 g_{rms} Random Noise Vibration

7.4. Prototype 3 Conclusions

The results produced from the third skin friction gage prototype showed that the electromagnet did possess a variety of advantages. It was capable of producing an output that was less sensitive to the noise caused by vibrations. An electromagnetically damped skin friction gage operating in a 8 g_{rms} or 2 g_{rms} flight testing environment will see reduced noise levels due to vibration of 24% and 6% of the lowest anticipated shear level, respectively. These non-dimensionalized strain gage outputs were for the worst case scenario, when τ_w=0.3 psf. The ratio of vibration induced noise to steady measured output decreases further as the shear levels increase to τ_w=1.5.

The damping levels obtained were not as large as analytically anticipated. This might be attributed to the K factor involved in Equation 18. Many scientists utilize a value of 0.3 for geometries similar to those found in this study, yet a report by NASA and UVA [34] found that this value of K produced erroneous results. For this case, a K factor of approximately 0.1 would be needed to reproduce the results obtained. This value is well within the range of values of K reported in the literature.

The off-axis excitation analysis showed that our vibration analysis did produce some perpendicular motion, yet the magnitude of these vibrations did not raise any concerns during testing.

The reduction of the head deflection amplitude during 8 g_{rms} and 2 g_{rms} random noise vibrations was a success. The head was not in any danger of contacting the housing during a test, and to verify this, there was no audible sound of the head making contact with the housing.

A variety of the concerns about gage operation were resolved as well. The bulky nature of the gage proved to be an inconvenience and an issue that needed to be resolved in the future. It turned out that the gage was capable of producing a substantial amount of heat over an extended period of operation, yet the effects were negligible for short duration testing (under 15 seconds). This was advantageous for wind tunnel tests, yet it could pose a problem during long-duration flight tests. A cooling system would need to be implemented to maintain a steady temperature at the strain gage. The magnetic interference proved to be a resolvable issue as well. The magnetic interference at the strain gage unit was negligible during full magnetic flux density operation of the electromagnet. This can be attributed to the use of a closed loop electromagnet design.

Overall, this gage concept proved to be a limited success providing a 33% reduction in noise associated with vibration.

Chapter 8. Wind Tunnel Verification Results

8.1. Wind Tunnel Vibration Tests

The ability of the third skin friction gage prototype to produce accurate results of skin friction needed to be verified at the Virginia Tech Supersonic Wind Tunnel before flight testing can be considered. The Virginia Tech supersonic wind tunnel shown in Figure 23 is capable of running at low enough Mach numbers and stagnation pressures to produce shear levels somewhat above the upper end of the values expected during flight tests, τ_w=3.9 to 5.3 psf. These shear levels are at the upper spectrum of the measuring capabilities of the gage. In fact, the floating head had to be decreased to a diameter of 0.25 inches to maintain the desired sensitivity level.

An analysis of the acceleration loads encountered during a wind tunnel test run needed to be performed before verification testing could begin. First accelerometers were attached to the wind tunnel on three axes, vertically (z), laterally (y), and longitudinally (x). The tunnel was run at those conditions desired for testing (Mach 2.4, T_o=300 K, P_o=55 psi), and PSD plots of the acceleration loads on the tunnel were measured.

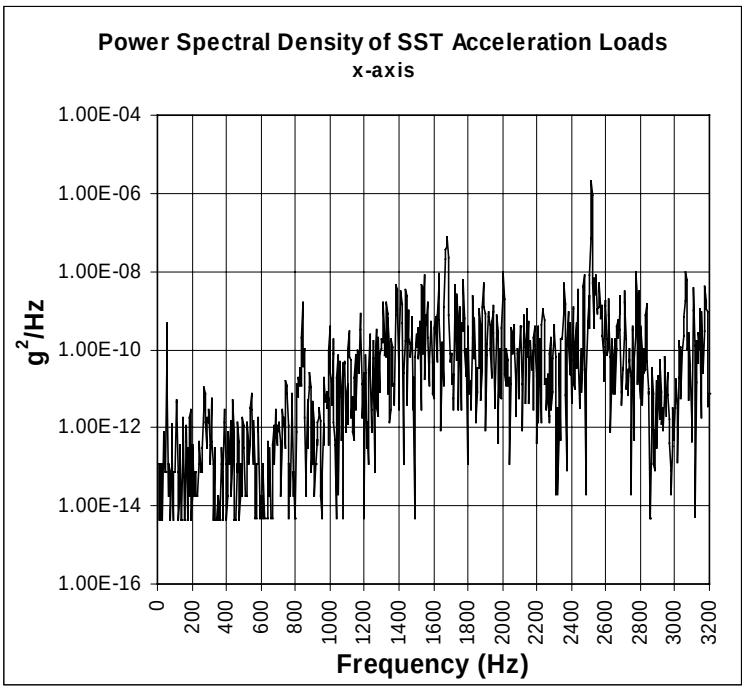

Figure 74: X-Axis Acceleration Loads During Supersonic Tunnel Run

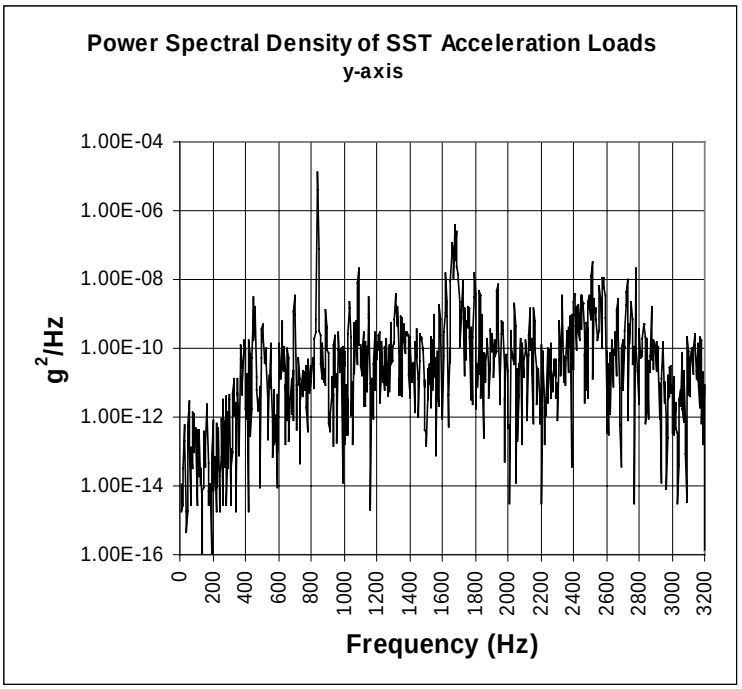

Figure 75: Y-Axis Acceleration Loads During Supersonic Tunnel Run

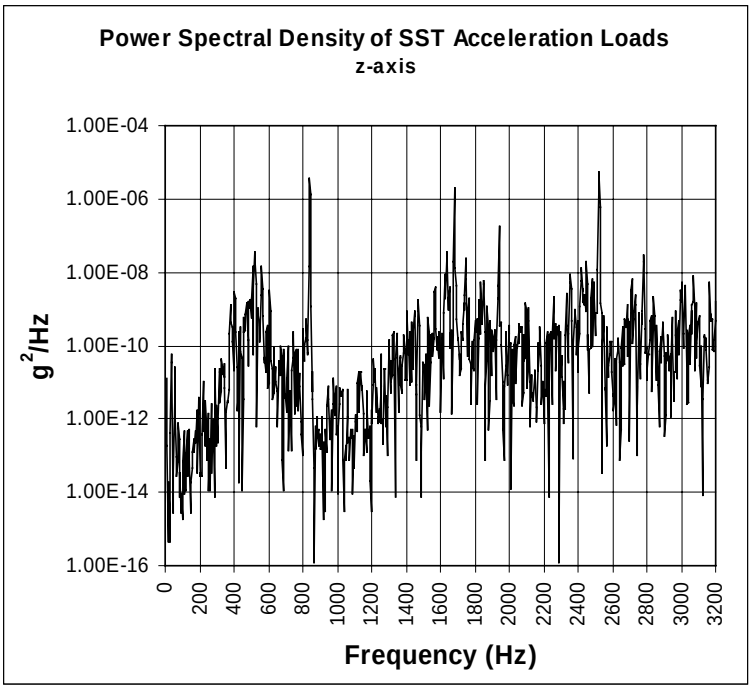

Figure 76: Z-Axis Acceleration Loads During Supersonic Tunnel Run

Figure 74, Figure 75, and Figure 76 show the acceleration loads on each axis. The results showed that during the steady portion of the tunnel run, the acceleration loads were much less severe than those encountered during the flight test shown in Figure 5. Thus, tests would provide the skin friction gage with a legitimate verification of its ability to measure shear, yet the vibration levels would not be as extreme as those anticipated on the F-15.

8.2. Experimental Skin Friction Results

The verification tests produced very good results. The third skin friction gage prototype was able to produce skin friction measurements that agreed with the theoretical prediction methods developed in Chapter 2.4. The measured skin friction values typically ranged from C_f=0.0016 to 0.0018. The gage was tested in the tunnel numerous times in order to verify the operability of each aspect of the gage. The gage was rotated 90 degrees for numerous runs to see if the gage would produce accurate results on both axes. The operability of the electromagnet was tested for each axis as well, even though the vibration levels were not severe. The results can be found in Figure 77, Figure 78, Figure 79, and Figure 80.

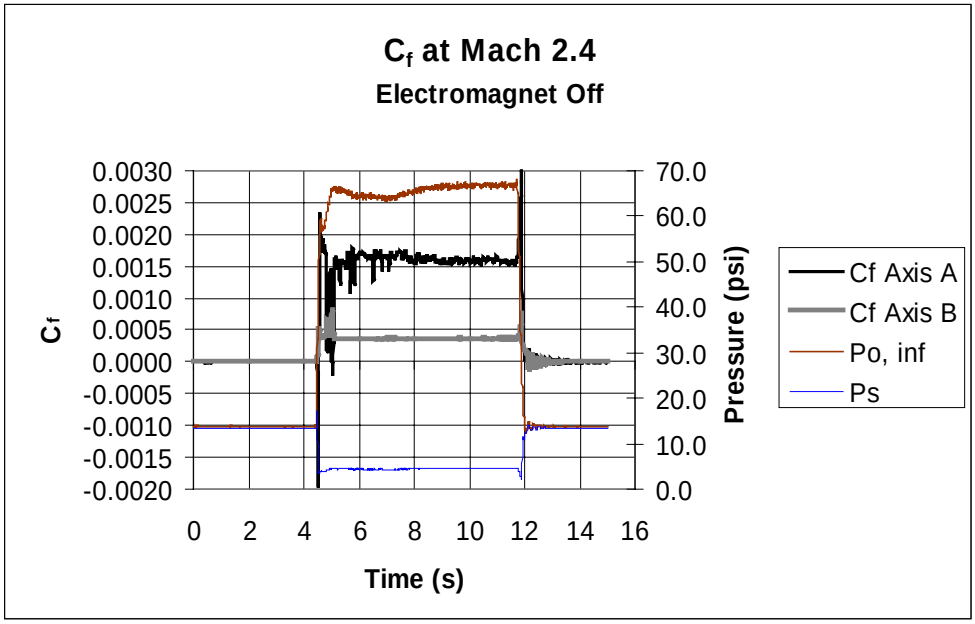

Figure 77: Test Run on Axis A with Electromagnet Off

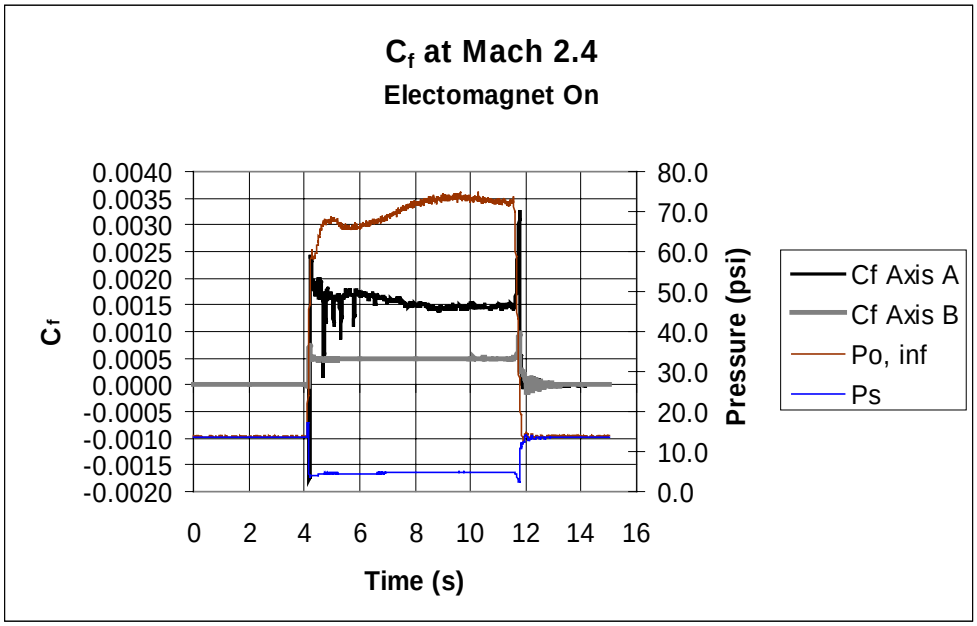

Figure 78: Test Run on Axis A with Electromagnet On

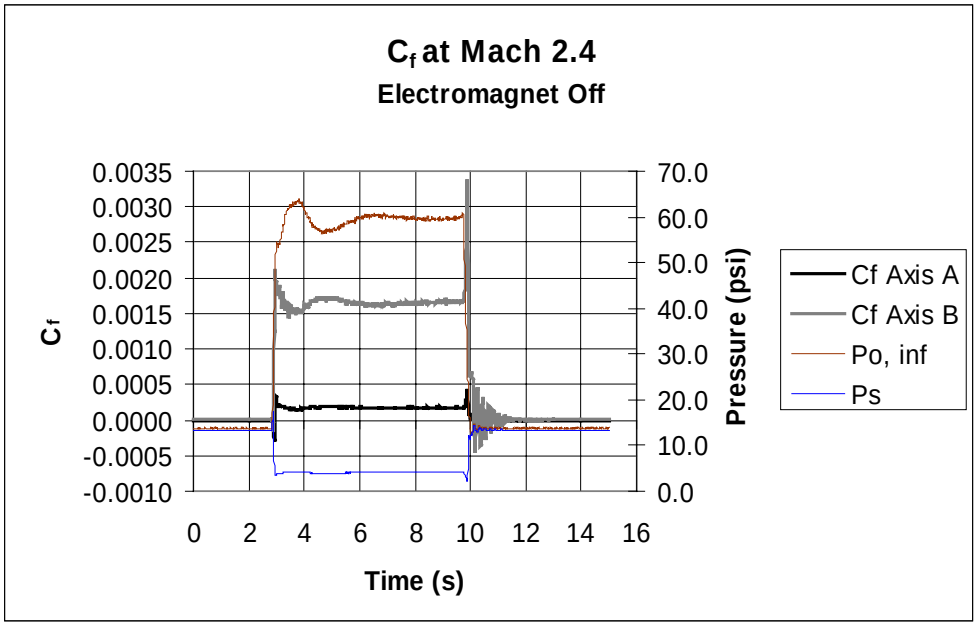

Figure 79: Test Run on Axis B with Electromagnet Off

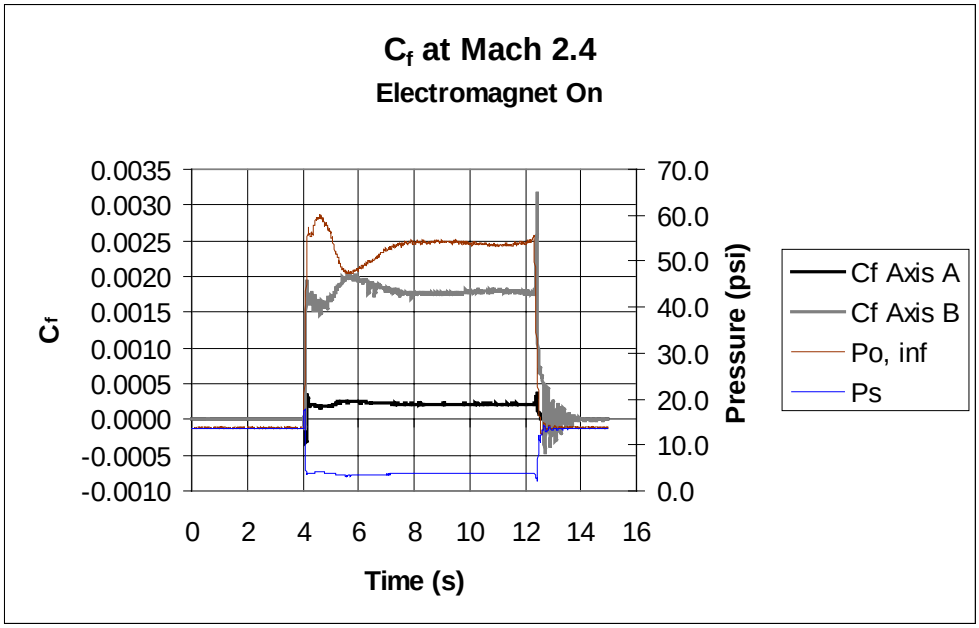

Figure 80: Test Run on Axis B with Electromagnet On

From top to bottom, the first curve represents the stagnation pressure within the tunnel during the run. The second two lines represent the skin friction measurements from the gage. The bottom line represented the static pressure at the gage. Due to the tendency of the supersonic tunnel to run at various steady stagnation pressures, the skin friction measurements from one run to the next varied. The repeatability of the run profiles was very good though. The tunnel utilized a rather archaic tunnel pressure control system that generally had a problem generating perfectly steady stagnation pressure conditions in the tunnel during the testing period. This became apparent in Figure 79 and Figure 80. In Figure 79, from 3 to 6 seconds, the total pressure oscillates slowly and dampens out. The same effect can be seen in Figure 80 from 4 to 8 seconds. A consequence of this phenomenon was that the skin friction measurements oscillated as well. Measured skin friction values were taken at locations on the graph where the stagnation pressure damped out to a steady value. From these measured pressures and the theory discussed in Chapter 2.1, theoretical values were calculated. Each of these tests showed good agreement with the predicted values. A comparison of these values can be seen in Table 8.

Table 8: Comparison of Theoretical and Experimental C_f

Test Condition	C_f - measured resultant	C_f - theoretical
Axis A, Electromagnet Off	$.00163 \pm 2x10^{-4}$	.00157
Axis A, Electromagnet On	$.00159 \pm 2x10^{-4}$	00155
Axis B, Electromagnet Off	$.00165 \pm 2x10^{-4}$	.00161
Axis B, Electromagnet On	$.00178 \pm 2x10^{-4}$	.00174

These results match fairly well, and are within the estimated ± 7.21 % error determined in the error analysis performed in Table 3 of Chapter 3.5. The predicted values were consistently slightly lower than the experimental values. This may be a result of the rather simple theoretical method, which utilized the incompressible to compressible relation from Van Driest. Also, this method utilized numbers read from a graph from Van Driest [37], which inherently could present some error. Nonetheless, the results from the wind tunnel verification tests were more than satisfactory.

Chapter 9. Conclusions and Recommendations

The goal of designing, constructing, and testing an instrument capable of accurately measuring wall shear (skin friction) was successful, and the goal of successfully dampening out the severe vibration induced noise inherent to flight testing without oil filling was a limited success. A skin friction gage that utilized a new eddy-current damping technique was designed. This passive damper was capable of reducing the amplitudes of the floating sensor head deflections. The maximum achieved damping from an electromagnetic eddy-current damper was a 33 % reduction in the amplitude of the sensing element vibrations at the first bending mode of vibration.

Three gages were designed. The first gage utilized small air gaps to provide the required damping. This approach was the easiest to implement, and if the gage performed adequately in the vibration simulation, little if any changes would need to be implemented into future designs which would also need to perform under similar rigorous test conditions. The noise caused by the 8 g_{rms} and 2 g_{rms} vibrations produced 30 to 5 times the expected skin friction output value, respectively. These noise levels produce measurements of little value. In addition, the amplitudes of the vibrations were so large that the head contacted the housing during testing. From this gage, it was concluded that a much stronger form of damping was required for all skin friction gages being designed for severe vibration environments.

The other two designs approached the damping issue more aggressively and used magnetism as a tool for damping. Of the eddy current damping designs, two systems came into fruition- one which utilized permanent magnets, and the other which used an electromagnet. The permanent magnet system produced favorable results, yet they were not completely satisfactory. Vibration induced noise levels were still larger than desired. The noise caused by the 8 g_{rms} and 2 g_{rms} vibrations produced 9 to 1 times the expected skin friction output value. Consequently, a method of producing greater damping was required.

The electromagnet concept boosted the level of damping available to the gage, with some drawbacks. The gage produced heat from the electromagnet, which could potentially cause the output to drift over long duration tests. The interference involved with the magnetic flux lines and the strain gage operation proved not to be a concern. The size of the

gage grew rather bulky, thus requiring a large surface for the test plate. Regardless of the drawbacks, the electromagnet concept proved to be the most successful of the three prototypes. The noise caused by the 8 g_{rms} and 2 g_{rms} vibrations produced only 24% to 6% of the expected skin friction output value. Due to the improved damping characteristics of the gage, the electromagnetic gage was the only prototype used to perform measurements in the supersonic wind tunnel. The wind tunnel tests provided good results of skin friction under rather mild vibration conditions.

In future gage designs several areas of improvement are needed. First and foremost, a better study of the optimum configuration should be performed to make sure that the eddy current damper is generating the maximum damping possible. Increased damping could be achieved by mounting the conductor of the eddy current damper more toward the floating head of the gage. Future electromagnetic eddy current dampers will need to have cooled temperature control systems. This will reduce the potential for temperature drift and potential damage to the gage. Gages will need to be reduced in size, so that they will be more manageable for other applications. Another problem associated with the third prototype is the power source required to run the electromagnet. They were cumbersome, bulky, and need to be replaced by a smaller piece of equipment. Ideally, the solution would be a permanent magnet capable of generating increased levels of magnetic flux density. In this manner, no power sources would be required and the size of the gage would be diminished. Also, future vibration verification tests should be combined with wind tunnel tests capable of simulating the actual environment encountered during flight-testing. A final recommendation for future skin friction gage designs is the implementation of an actively controlled damping system using piezo-electric materials. This method, although more complicated and involved than passive systems, would be able to more directly solve the problems associated with natural frequencies.

References

[1] Anderson, J.D., *Fundamentals of Aerodynamics.* 2nd Edition, McGraw-Hill, New York, 1991.

[2] Winter, K.G., "An Outline of the Techniques Available for the Measurement of skin Friction in Turbulent Boundary Layers," Progress in Aerospace Sciences, pp. 1-57, 1977.

[3] Froude, W., "Experiments on the Surface-friction Experienced by a Plane Moving through Water," 42nd British Association Report, pp. 118-124, 1872.

[4] Wooden, P.A. and Hull, G.H., "Correlation of Measured and Theoretical Heat Reansfer and Skin Friction at Hypersonic Speeds Including Reynolds Analogy," AIAA Paper No. 90-5244, Oct. 1990.

[5] Van Driest, E.R., "The Problem of Aerodynamic Heating", Aeronautical Engineering Review, vol.15, pp. 26-41, Oct. 1956.

[6] Nitsche, W., Haberland, C., and Thunker, R., "Comparative Investigation on Friction Drag Measuring Techniques in Experimental Aerodynamics," ICAS-84-2.4.1, 14th ICAS Congress, Sept. 1984.

[7] Preston, J.H., "The Determination of Turbulent Skin Friction by means of Pitot Tubes," Journal of Roual Aeronautical Society 58, pp. 109-121, 1954.

[8] Patel, V.C., "Calibration of the Preston Tube and Limitations on its use in Pressure Gradients," Journal of Fluid Mechanics 23, pp. 185-203, 1965.

[9] Nitsche, W., Haverland, C., and Thuenker, R., "A computational Preston Tube Method," Procedings of the 4th Symposium on Turbulent Shear Flows," pp. 15.1- 15.6, 1983.

[10] Nitsche, W. and Thuenker, R., "WAMPE-Wall Shear Stress Measuring Program (Computational Preston Tube Method)," TU-Berlin, ILR-Rep., 1984 .

[11] McCroskey, W.J. and Durbin, E.J., "Flow Angle and Shear Stress Measurements using heated Films and Wires," Journ. Basic Eng. 94, pp. 46-52, 1972.

[12] Nitsche, W. and Haberland, C., "Wanreibungsmessungen mit Oberflaechenhiessfilmsonder unter Beruecksichtigung von Termperatureinfluessen," Proc. of Sensor '83, vol. 1, pp. 42- 54, 1983.

[13] Owen, F. and Johnson, D.A., "Separated Skin-Friction Measurements-Source of Error: An Assessment and Elimination," AIAA 80-1409, AIAA 13th Fluid and Plasma Dynamics Conference, July 1980.

[14] Novean, M.G.G., *Direct Measurement of Skin Friction in Complex Supersonic Flows*. PhD thesis, Virginia Polytechnic Institute and State University, 1992.

[15] Gaudet, L. and Gell, T.G., "Use of Liquid Crystals for Qualitative and Quantitative 2-D studies of transition and skin friction," ICIASF '89 – 13th International Congress on Instrumentation in Aerospace simulation Facilities, vol. 43, pp. 66-81, 1989.

[16] Tanner, L.H. and Kulkarni, V.G., "A Study of the Motion of Oil Films on surfaces in Air flow, with Application to the Measurement of Skin Friction', J. Physics E, vol. 9, pp. 194-202, 1976.

[17] Monson, D.J. and Mateer, G.G., "Boundary-Layer Transition and Global Skin Friction Measurements with an Oil-Fringe Imaging Technique," SAE 932559, Aerotech '93, Costa Mesa, CA, Sept. 27-30, 1993.

[18] Zilliac, G.G., "Further Developments of the Fringe-Imaging Skin Friction Technique," NASA Technical Memorandum 110425, Ames Research Center, pp. 1-35, December 1996.

[19] Tanner, L.J. and Kulkarni, V.G., “A Skin Friction Meter, Using the Viscosity Balance Principle, Suitable for Use with Flat or Curved Metal Surfaces,” J. Physics E, vol. 10, pp. 278-284, 1977.

[20] Tanner, L.J. and Kulkarni, V.G., “The Viscosity Balance Method of Skin Friction Measurement: further Development Including Application to Three-Dimensional Flow,” J. Physics E, vol. 9, pp. 1114-1121, 1976.

[21] Monson, D.J. and Higuchi, H., “Skin Friction Measurements by a New Nonintrusive Double Laser Beam-Oil Viscosity Balance Technique,” AIAA J., vol. 19, no. 6, pp. 739-744, 1980.

[22] Westphal, R.V., Bachalo, W.D., and Houser, M.H., “Improved Skin Friction Interferometer,” NASA TM-88216, 1986.

[23] Magill, S.A., *Study of a Direct Measuring Skin Friction Gage with Rubber Compounds for Damping*. Master’s Thesis, Virginia Polytechnic Institute and State University, 1999.

[24] Dhawan, S., “Direct Measurements of Skin Friction,” NACA Report 1121, pp.281-300, 1953.

[25] Schetz, J.A., "Direct Measurements of Skin Friction in Complex Flows," Applied Mechanics Review, Vol. 50, No. 11, Pt. 2, Nov. 1997

[26] Chadwick, K.M., *An Actively cool floating element Skin Friction Balance for Direct Measurement in High Enthalpy Supersonic Flows.* PhD thesis, Virginia Polytechnic Institute and State University, 1992.

[27] Deturris, K. J., *A Technique for direct Measurement of Skin Friction in Supersonic Combustion Flow*. PhD thesis, Virginia Polytechnic Institute and State University, 1992.

[28] Bogdan, L., “Instrumentation Techniques for Short-Duration test Facilities,” Tech. Rep. Calspan Report No. WTH-030, Calspan Corp., Mar, 1967.

[29] MacArthur, R. C., “Transducer for Direct Measurement of Skin Friction in a Hypersonic Shock Tunnel,” Tech. Rep. Calspan Report No. 129, Calspan Corp., Aug. 1963

[30] MacArthur, R.C., “Contoured Skin Friction Transducers,” Tech. Rep. Calspan Report No. AN-2403-Y-1, Calspan corp., Aug. 1967

[31] Kelly, G. M., Simmons, J.M., and Paull, Al., “Skin Friction Gauge for Use in Hyper-velocity Impulse Facilities,” AIAA, vol. 30, pp. 844-845, Mar. 1992.

[32] Jolly, M.R., Bender, J.W., and Carlson, J.D., “Properties and Application of Commercial Magnetorheological Fluids,” SPIE 5th Annual Int. Symposium on Smart Structures and Materials, San Diego, March 15, 1998

[33] Inman, D.J., *Engineering Vibration*. Prentice Hall, New Jersey, pg. 240- 250, 1996.

[34] Park, C.H., Inman D.J., Kabeya, K., “Enhanced Piezoelectric Shunt Design,” Virginia Polytechnic Institute and State University, Deparment of Mechanical Engineering, CIMMS, 1998.

[35] McCaig, M. and Clegg, A.G., *Permanent Magnets in Theory and Practice*. John Wiley & Sons, New York, 1987

[36] Gunter, E.J., Humphris, R.R., and Severson, S.J., “Design Study of Magnetic Eddy-Current Vibration Suppression Dampers for Application to Cryogenic Turbomachinery,” University of Virginia, Department of Mechanical and Aerospace Engineering, December 1983

[37] NASA ADFRF, “Environmental Testing Electronic and Electromechanical Equipment,” Process Specification No. 21-2, pp. 25-29.

[38] Schetz, J., *Boundary Layer Analysis.* Prentice-Hall, Inc., ISBN 0-13-086775-X, 1993.

[39] Van Driest, E.R., “Turbulent Boundary Layer in Compressible Fluids,” J. Aeronaut. Sci., Vol. 18, No. 3, pg. 145, March 1951.

[40] Ogata, K., *System Dynamics*, 2nd Edition, Prentice-Hall Inc., New Jersey, 1992.

[41] James, M.L., Smith, G.M., Wolford, G.C., and Whaley, P.W., *Vibration of Mechanical and Structural Systems with microcomputer Applications*. 2nd edition. Harper Collins College Publishers, New York, 1994.

[42] Tongue, H.B., *Principles of Vibration*. Oxford University Press, New York, pg. 97-110, 1996.

[43] Harris, C.M., and Crede, C.E., *Shock and Vibration Handbook.* 2nd edition, McGraw-Hill Book Company, New York, pp. 2-15, 1990.

[44] Harris, F.J., "On the Use of Windows for Harmonic Analysis with the Discrete Fourier Transform," Proceedings of the IEEE, Vol. 66, No.1, Jan. 1978.

[45] Michell, L.D., Young K.J., and Mitchell, S.A., *User's Guide-- Beam 6.* Edition 6.1, Program version 6.0, Department of Mechanical Engineering, Virginia Polytechnic Institute and State University, August 1991.

[46] Stratton, J.A., *Electromagnetic Theory*. McGraw-Hill Book Company, New York, 1941.

[47] Nagaya, K. and Kojima, H., "On a Magnetic Damper Consisting of a Circular Magnetic Flux and a Conductor of Arbitrary Shape," Transactions of the ASME, Journal of Dynamic Systems, Measurement and Control, Vol. 106, March 1984, pg. 46-55

[48] Weinberger, M.R., " Drag Force of an Eddy Current Damper," IEEE Transactions, Aerospace and Electronic Systems, Vol. AES-13, No. 2, March 1977, pg. 197-200

[49] Moskowitz, L.R., *Permanent Magnet Design and Application Handbook.* Robert E. Krieger Publishing Company, Inc., Malabar, Florida, 1976

[50] Campbell, P., *Permanent Magnet Materials and Their Application*. Cambridge University Press, New York, 1994

[51] Cullity, B.D., *Introduction to Magnetic Materials.* Addison-Wesley Publishing Co., Massachusetts, 1972

[52] Plonus, M.A., *Applied Electromagnetics*. McGraw Hill Book Company, New York, 1978.

[53] Cherry, L.B., "Electro-Magnetic Induction Damping of Vibratory Motion," Acoustic Society of America, Noise Control, September/October, 1960, pg. 8-11

[54] Okada, Y., "Analysis and Experiments of the Electro-Magnetic Servo Vibration Damper," Bulletin of the JSME, Vol. 20, No. 144, June, 1977, pg. 696-702

[55] Yamakwa, I., Takeda, S. and Kojima, H., "Behavior of a New Type of Vibration Absorber consisting of Three Permanent Magnets," Bulletin of the JSME, Vol. 20, No. 146, August, 1997, pg. 947-954

[56] Maly, R.F., Smith, C.A. and Anderson, E.H., "Family of Smart Magnetic Tend-Mass Dampers," Air Force Research Laboratory, September 1997, pg. 4-21

[57] Carpenter Specialty Alloys, *Magnetic Alloys*, Carpenter Technology Corporation, December 1990.

[58] Mikulinsky, M. and Shtrikman, S., "Optimization of an Eddy Current Damper," IEEE, Electric Machines and Electromechanics, Volume 5, 1980, pg. 417-432

[59] Figliola, R.S. and Beasley, D.E., *Theory and Desgin for Mechanical Measurements.* 2nd Edition, John Wiley & Sons, Inc., New York, 1995, pp. 171-210.

[60] Allen, J. M., "Improved Sensing element for Skin-Friction Balance Measurements," AIAA Journal, vol. 18, pp.1342-1345, Nov. 1980.

Vita

Alexander Remington

The author was born on May 19, 1975 in Boston, Massachusetts. He was raised and received his elementary education in Sudbury, Massachusetts. He conducted his undergraduate engineering studies at the University of Notre Dame in Indiana where he received a Bachelor of Science in Aerospace Engineering in May of 1997. Upon completion of his undergraduate education, he entered the graduate program at the Virginia Polytechnic Institute and State University. He spent the next 2 years in pursuit of a Masters of Science in Aerospace Engineering which was completed in July of 1999.